Catalysis with Porous MOFs

Structure-Catalytic Property-Relationships in the Hydroformylation of Olefins over Rh Supported Metal-Organic Frameworks

Dissertation

zur

Erlangung des akademischen Grades

doctor rerum naturalium (Dr. rer. nat.)

der Mathematisch-Naturwissenschaftlichen Fakultät

der Universität Rostock

Rostock, 2014

vorgelegt von Toan Van Vu, geb. am 17.12.1976 in Nam Dinh - Vietnam

Die vorliegende Arbeit wurde von Juni 2010 bis November 2013 am Institut für Chemie und Leibniz-Institut für Katalyse an der Universität Rostock unter der Betreuung von Prof. Dr. Axel Schulz angefertigt.

Gutachter:

     1.   Prof. Dr. Axel Schulz

             Institut für Chemie, Universität Rostock

     2.   Prof. Dr. Udo Kragl

             Institut für Chemie, Universität Rostock

Datum der Einreichung: 02. April 2014

Datum der Verteidigung: 17. Juli 2014

Erklärung

Ich versichere hiermit an Eides statt, dass ich die vorliegende Arbeit selbstständig angefertigt und ohne fremde Hilfe verfasst habe, keine außer den von mir angegebenen Hilfsmitteln und Quellen dazu verwendet habe und die den benutzten Werken inhaltlich und wörtlich entnommen Stellen als solche kenntlich gemacht habe.

Toan Van Vu

Rostock, den 02.04.2014

Acknowledgements

Abstract

This work deals with preparation, characterization, and catalytic testing of Rh supported catalysts based on porous MOFs using hydroformylation of olefin with synthesis gas to aldehydes as a model reaction. It emphasizes on the influence of the MOF support on the catalytic performance, i.e., the Structure-Catalytic Property-Relationships. Selected MOFs with different structures and pore sizes ranging from small to extra-large mesoporous were solvothermally synthesized and functionalized with low concentrations of Rh(acac)(cod). The samples were characterized by XRD, FTIR, SEM, TEM, nitrogen adsorption-desorption, AAS, XPS, and SAXS measurements. The prepared MOFs are crystalline and highly porous. The Rh in all Rh@MOF samples is highly dispersed in a single site manner (single site catalysts). The catalytic results in the hydroformylation of olefins with different structures and chain lengths over different Rh@MOFs show that the catalysts are very active (conversion) and selective. The catalytic performance is affected by the structure, texture, and porosity of the MOF support. Besides, it is concluded that the orientation of the rotating phenylene linker with respect to the pore window has an important impact on the diffusivity of olefins (conversion). Single-file diffusion in quasi one-dimensional pores is discussed to be the reason of improved conversion with olefin mixture.

Zusammenfassung

Diese Arbeit beschäftigt sich mit der Präparation, Charakterisierung und katalytischen Testung von Rh –Trägerkatalysatoren auf der Basis von porösen MOFs. Die Hydroformylierung von Olefinen zu Aldehyden diente als Testreaktion. Ziel der Arbeiten war die Untersuchung von Struktur- Katalyse-Eigenschaftsbeziehungen. Ausgewählte MOF-Träger mit unterschiedlicher Struktur und Porengröße von schmall bis extragroß mosporös wurden solvothermisch synthetisiert und mit geringen Konzentrationen an Rh(acac)(cod) katalytisch funktionalisiert. Die Materialien wurden mittels XRD-, FTIR-, SEM-, TEM-, Stickstoff- Ad- und Desorption, AAS-, XPS-, und SAXS-Untersuchungen charakterisiert. Die erhaltenen MOFs sind kristallin und hochporös. In allen Rh@MOF -Trägerkatalysatoren ist Rh hoch dispers, in Form von „single sites", verteilt. Die katalytischen Ergebnisse in der Hydroformylierung von Olefinen mit unterschiedlicher Struktur und Länge mit den verschiedenen Rh@MOFs zeigt, dass die Katalysatoren sehr aktiv (Umwandlung) und selektiv sind. Das katalytische Verhalten wird durch die Struktur, Textur und Porosität der MOFs beeinflusst. Es wird auch geschlussfolgert, dass die Orientierung der rotierbaren Linker bezüglich der Porenöffnungen einen deutlichen Einfluss auf die Diffusivität (Umwandlung) der Olefine hat. Die erhöhte Aktivität (Umwandlung) von Olefinmischungen wird auf das Auftreten der „Single file" Diffsusion in quasi eindimensionalen Poren zurückgeführt.

Table of contents

List of figures

List of schemes

List of tables

List of abbreviations

2-pymo	2-Pyrimidinolate
4,4'-bpy	4,4'-Bipyridine
3D	Three dimension
AAS	Atomic absorption spectroscopy
acac	Acetylacetonate
ATR	Attenuated total reflection
BDC	1,4-Benzenedicarboxylate
BET	Brunauer-Emmett-Teller
BTC	1,3,5-Benzenetricarboxylate
CCD detector	Charge-coupled device detector
CTAB	Cetyl trimethylammonium bromide
CUS	Coordinative unsaturated metal sites
DEF	Diethylformamide
DMF	Dimethylformamide
EtOH	Ethanol
FTIR	Fourier transform infrared spectroscopy
H$_2$BDC	1,4-Benzenedicarboxylic acid
HKUST	Hong Kong University of Science and Technology
HKUST-1, MOF-199	$[Cu_3(BTC)_2]$
IRMOF-	Isoreticular metal-organic framework
IRMOF-3	$Zn_4O[O_2C-C_6H_3(NH_2)-CO_2]_3$
IUPAC	International Union of Pure and Applied Chemistry
M(cod)(cot)	M = metal, cod = cyclooctadiene, cot = cyclooctatriene
MCM-41	Mobile Crystalline Material – 41
MIL-	Matérial Institut Lavoisier –
MIL-53(Al)	$Al(OH)[O_2C-C_6H_4-CO_2].[HO_2C-C_6H_4-O_2H]_{0.70}$
MIL-77	$[Ni_{20}\{(C_6H_8O_4)_{20}(H_2O)_8\}]\cdot 33H_2O$
MIL-96	$Al_{12}O(OH)_{18}(H_2O)_3(Al_2(OH)_4)(BTC)_6\cdot 24H_2O$
MIL-100	$Cr_3X(H_2O)_2O[C_6H_3-(CO_2)_3]_2\cdot nH_2O$, n = 14.5, X = F/OH
MIL-101(Cr)	$Cr_3X(H_2O)_2O[(O_2C-C_6H_4-CO_2)]_3\cdot nH_2O$, n = 25, X = F/OH
mmol	millimole
MOF	Metal-organic framework
MOF-5	$[Zn_4O(BDC)_3]$ or $Zn_4O[O_2C-C_6H_4-CO_2]_3$
MSU-	Michigan State University –
NH$_2$-MIL-101(Al)	$Al_3O[(O_2C)-C_6H_3NH_2-(CO_2)]_3\cdot nH_2O$
p	Pressure
p/p$_0$	Relative pressure

Rh(acac)(cod)	(Acetylacetonato)(cycloocta-1,5-diene) rhodium(I)
SAXS	Small-angle X-ray scattering
SBA-	Santa Barbara Amorphous – (University of California, Santa Barbara)
SEM	Scanning electron microscope
sita	2-Salicylideneimine terephthalate
ST	Supertetrahedra
T	Temperature
TEM	Transmission electron microscope
TEOS	Tetraethyl orthosilicate
TGA	Thermogravimetric analysis
TMAOH	Tetramethylammonium hydroxide
TMB	1,3,5-Trimethylbenzene
TMP	2,4,4-Trimethylpent-1-ene
UHV	Ultra-high vacuum
wt%	Weight percent
XPS	X-ray photoelectron spectroscopy
XRD	X-Ray diffraction

Unit conversion

Quantity	Symbol	Name	Conversion
Length	Å	Angstrom	$1\ \text{Å} = 10^{-10}\ \text{m}$
	μm	micrometer	$1\ \mu\text{m} = 10^{-6}\ \text{m}$
	nm	nanometer	$1\ \text{nm} = 10^{-9}\ \text{m}$
Power	mW	milliwatt	$1\ \text{mW} = 10^{-3}\ \text{kg m}^2\ \text{s}^{-3}$
Temperature	°C	degree Celsius	$\text{K} = °\text{C} + 273.15$
Volume	mL	milliliter	$1\ \text{mL} = 1\text{cm}^3 = 10^{-6}\ \text{m}^3$
Wavenumber	cm^{-1}	reciprocal centimeter	$1\ \text{cm}^{-1} = 100\ \text{m}^{-1}$
Time	h	hour	$1\ \text{h} = 3{,}600\ \text{s}$
	min	minute	$1\ \text{min} = 60\ \text{s}$
Pressure	bar	bar	$1\ \text{bar} = 100{,}000\ \text{Pa}$
	hPa	hectopascal	$1\ \text{hPa} = 100\ \text{Pa}$
Energy	eV	electron-volt	$1\ \text{eV} = 1.6\ \text{x}\ 10^{-19}\ \text{J}$

1. Objectives

This study deals with preparation and characterization of rhodium supported MOF catalysts and detailed investigation of their catalytic performances in the hydroformylation of olefins. The main objectives are:

- Investigation of the relation between structure and porosity of MOFs and corresponding catalytic properties;
- Using the unique properties of the MOF structure, i.e., the organic-inorganic hybrid nature and porosity, to realize single site catalysts with improved catalytic performance.

Approach

- Synthesis of metal-organic frameworks with different structures and pore sizes, i.e., small, medium and large pore-sized MOFs as well as extra-large mesostructured MOFs (MesoMOFs);
- Immobilization of rhodium species with very low loading on the MOF materials to obtain different site isolated rhodium supported catalysts, Rh@MOFs, with similar rhodium contents;
- Detailed study of the catalytic performance of Rh@MOFs taking the hydroformylation of olefins with the different chain lengths and structure as model reactions;
- Evaluation of the influence of the structures and pore sizes of metal-organic frameworks on the catalytic performance;
- By using olefins with different structures and chain lengths in the hydroformylation reactions over the rhodium supported catalysts, Rh@MOFs, in which the selected MOF supports are with different structures and pore sizes, it is intended to investigate the influence of the MOF structures on the catalytic performance.

Based on the catalytic data achieved with the different Rh@MOFs as well as the catalyst characterization results, the influence of the MOF structures and pore sizes on the catalytic activity and selectivity will be evaluated in order to derive the Structure-Catalytic Property-Relationships.

2. Introduction

In the last two decades, the research around metal-organic frameworks (MOFs) has extended rapidly.[1] Porous MOFs are highly crystalline ordered organic-inorganic hybrid materials in which metal clusters and organic linkers are strictly connected forming three dimensional ordered frameworks. These hybrid materials possess a variety of properties such as very high specific surface area of up to 10400 $m^2 \ g^{-1}$,[2] high pore volume of up to 2.3 $cm^3 \ g^{-1}$,[3] tunable pore size ranging from micro to mesopores (2–50 nm), and cage sizes of up to 30–34 Å.[4] Very recently, pore size expansion of close to 98 Å has been achieved with one-dimensional channel systems by using long chain linkers.[5] Moreover, the huge amount of possibilities to functionalize the MOF by exchange and modification of organic linkers and metal compartments allow varying the material properties to a large extent.[6-11] Therefore, these materials have attracted great attention,[12] especially in catalysis,[1,13-25] adsorption or separation and others.[12,26-32]

Besides the highly porous properties, the crystalline ordered MOF frameworks with the strictly alternating arrangement of well-defined hydrophilic metal (oxide) clusters and hydrophobic organic linkers on a molecular level provide excellent conditions for the preparation of unique single site catalysts. These characteristics might provide MOFs with high activity and selectivity in catalysis. Hence, the catalytic application of MOF-based catalysts is of potential, especially under mild conditions, as often applied for the fine chemical synthesis including the highly important hydroformylation of olefins.

Discovered by Otto Roelen in 1938,[33] the hydroformylation is the reaction of olefinic double bonds with synthesis gas yielding linear and branched aldehydes as primary products. Linear aldehydes, the more valuable products, can be used for the production of alcohols. Approximate 9 million metric tons of aldehydes and alcohols are annually produced by using this reaction.[34] These products are important feed stocks for the synthesis of plasticizers, detergents, adhesives, solvents, pharmaceuticals, and agrochemicals as well.[35,36] Both cobalt and rhodium complexes are used in the industrial homogeneous catalyzed hydroformylation.[37,38] Even though the traditional hydroformylation is effective, there is an interest in the

heterogenization of this organic synthesis process due to the expected advantage of the heterogeneous process, e.g., catalyst recovery, over the homogeneous one. Thus, many efforts have been undertaken to immobilize catalytic active species on supports as silica, alumina, micro and mesoporous materials like zeolites and MCM-41, activated carbons, and organic polymers.[34,38-53] However, there are some limits of the supports in this heterogeneous hydroformylation due to loss of activity, low thermal stability or complicated procedure to synthesize the catalyst as reported in the literature.[34]

Porous metal-organic frameworks give new opportunities for the heterogenization of homogeneous catalysts. High porosity and large pore openings may enhance the mass transfer properties. Furthermore, the formation of single site active species could boost catalytic activity and selectivity. Both are expected to improve the catalytic performance. Therefore, the hydroformylation of olefins over rhodium supported catalysts based on MOFs is targeted in this research.

2.1. State of the art

The exceptional high porosity combined with the hybrid nature with defined separated and strictly alternating arrangement of inorganic units and organic linkers allows a high dispersion of active sites of a unique structure in a single site manner throughout the MOF framework. Owing to these attractive properties, MOFs are expected to be employed in heterogeneous catalysis.

The catalytic sites of MOFs can be of different origin:

(i)   The metal clusters of the MOF framework;

(ii)   Functionalized linker (e.g., acid or base function);

(iii)   Active species immobilized in the MOF framework (e.g., supported complexes, metals, metal oxide cluster or enzymes).

Several case studies giving a proof of principle related to the application of MOFs in catalysis have been published so far.[12,17,54,55] However, detailed catalytic studies are still rare.

In an early report, in 1994 Fujita et al. showed that the MOF $[Cd(4,4'-bpy)_2](NO_3)_2$ was catalytically active in the cyanosilylation of aldehydes.[56] The activity is assigned to Lewis-acid sites created at the coordinative unsaturated metal sites (CUS) of the cadmium centers. Similarly, the acid sites at CUS of Cu^{2+} in the compound $[Cu_3(BTC)_2]$, namely MOF-199, have been shown to catalyze the cyanosilylation of benzaldehyde and cyanotrimethylsilane.[18] A porous MOF namely MIL-101 discovered by Férey et al.[4] with the chemical formula of $[(Cr_3F(H_2O)_2O(BDC)]_3\cdot 25H_2O$ is also active in this reaction.[24] The acid sites created at CUS of Cr^{3+} oxide clusters (*ca.* 1 mmol g^{-1}) are expected to be the reason for the observed catalytic activity.[57] Horcajada et al. observed that both MIL-100(Cr, Fe) are active in the Friedel-Crafts benzylation of benzene with benzyl chloride.[58] A MOF, $[Pd(2-pymo)_2]$, is shown to be active in the partial oxidation of alcohol (3-phenyl-2-propen-1-ol to aldehyde) and in the Suzuki-Miyaura cross coupling reaction of phenylboronic acid and 4-bromoanisole.[19] Cu-based MOFs, $[Cu_3(BTC)_2]$, has been shown to catalyze the hydrosilylation of ketones.[59]

The amino-functionalized IRMOF-3 with the formula of $[(Zn_4O)(NH_2-BDC)_3]$ is shown to be active in the Knoevenagel condensation of benzaldehyde with ethyl cyanoacetate due to the active basic site of the organic linker.[60] Similarly, sulfated MIL-53 (Al) and MIL-101 (Cr) are active in the esterification reaction of *n*-butanol with acetic acid due to the Brønsted acid sites.[61]

Different noble metal supported MOF catalysts have been prepared and catalytically tested mainly for hydrogenation reactions (Table 1). The hydrogenation of different substrates such as cyclooctene, styrene, ethyl cinnamate, and 2-butyne-1,4-diol over palladium supported MOF-5, $[Zn_4O(BDC)_3]$, which was discovered by Yaghi and co-workers in 1999,[62] has been reported.[23,63,64] Similarly, the palladium supported MIL-101 has been found to be remarkably stable and active in the hydrogenation of styrene and cyclooctene. It shows significantly higher activity than, e.g., of palladium supported activated carbon.[24] Pd@MIL-101 has been also used as a multifunctional catalyst in the one-step synthesis of methyl isobutyl ketone by the multi-step hydrogenation reaction starting with acetone.[65] High palladium loaded MIL-101 catalysts containing different sized palladium nanoparticles have been tested in the selective hydrogenation of ketones to the corresponding alcohols.[66] The study of

4

Zhang et al. shows that IRMOF-3-SI-Au, [$Zn_4O(sita-AuCl_2)_x(NH_2-BDC)_{3-x}$], is very active in the hydrogenation of buta-1,3-diene.[67]

In summary, a couple of case studies proofed the catalytic activity of metal-organic frameworks and its usability as catalyst supports. However, systematic investigations of the catalytic performance of porous metal organic frameworks are rare.[1] Especially, the potential application of MOFs in the hydroformylation of olefins to aldehydes, an important reaction in the chemical industry to manufacture oxygenated compounds has not been investigated so far. Therefore, this contribution is aimed to study the catalytic performance of rhodium supported MOFs focusing on the hydroformylation.

Table 1. Catalytic reactions with metal supported catalysts based on MOFs.

MOF	Active site	Reaction	Substrate	Ref.
[Pd(2-pymo)$_2$]*	Pd^{2+}	partial oxidation	3-phenyl-2-propen-1-ol to aldehyde	[19]
		Suzuki-Miyaura cross coupling	phenylboronic acid and 4-bromoanisole	[19]
Pd@MOF-5	Pd (1 wt%)	hydrogenation	cyclooctene, styrene	[63]
Pd@MOF-5	Pd (0.5 wt%)	hydrogenation	ethyl cinnamate	[23]
Pd@MOF-5	Pd (1 wt%)	hydrogenation	2-butyne-1,4-diol	[64]
Ni@MOF-5	Ni (7.4 wt%)	hydrogenation	crotonaldehyde	[20]
Ru@MOF-5	Ru (31 wt%)	oxidation	benzyl alcohol to benzaldehyde	[68]
		hydrogenation	benzene	[68]
Pd@MIL-101	Pd (1 wt%)	hydrogenation	styrene, cyclooctene	[24]
Pd@MIL-101	Pd (0.11–0.87 wt%)	multi-step hydrogenation	acetone to methyl isobutyl ketone	[65]
Pd@MIL-101	Pd (40 wt%)	hydrogenation	different ketones	[66]
Pt@NH$_2$-MIL-101(Al)	Pt-W (Pt/W/Al = 0.33/2.02/1)	oxidation	CO	[69]
		hydrogenation	toluene	[69]
IRMOF-3-SI-Au, [$Zn_4O(sita-AuCl_2)_x$ $(NH_2-BDC)_{3-x}$]	Au^{3+}	hydrogenation	buta-1,3-diene	[67]
Mn@IRMOF-3	Mn^{2+}	epoxidation	alkenes (cyclohexene, cyclooctene and styrene) with trimethylacetaldehyde	[70]

* Pd in the MOF framework.

2.2. Porous MOFs

2.2.1. Composition and structure of MOFs

Porous MOFs are crystalline organic-inorganic hybrid materials in which metal clusters, usually metal oxides, and organic linkers are strictly connected forming three dimensional ordered frameworks. The interest in porous MOFs and their applications in adsorption and catalysis started in the 1990s where a couple of new hybrid materials with accessible large pore systems were discovered. For instance, in 1995, Zaworotko and co-worker reported the synthesis of $[Zn(4,4'-bpy)_2]SiF_6$ with large non-interpenetrated channels (Figure 1). The channels and the unit cells have the same dimensions of 11.396 x 11.396 Å. The effective size of the pores is of 8 x 8 Å, similar to the pore size of large zeolites. The volume of the channels is about 50% of the total volume.[71]
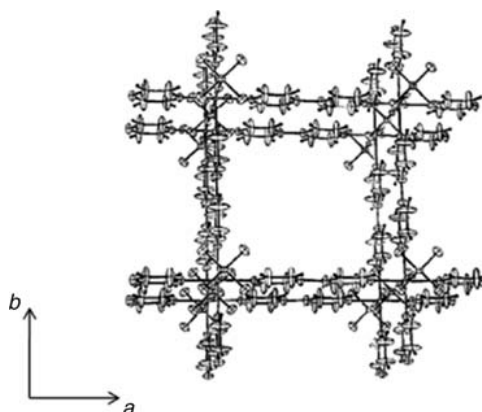
Figure 1. Representation of a square channel viewed along the *c* crystallographic axis. Figure taken from ref.[72]

In the same year, Yaghi and co-worker were successful in preparing $[Cu(4,4'-bpy)_{1.5}]NO_3 \cdot (H_2O)_{1.25}$ under hydrothermal condition. The single-crystal X-ray diffraction of this compound reveals that the Cu centers are connected with rod-like 4,4'-bpy ligands forming a three dimensional network, as shown in Figure 2.

A landmark of the MOF study could be the success in preparation of the most well-known MOF namely MOF-5 by Yaghi and co-workers in 1999. The schematic representation of the formation of MOF-5 is illustrated in Figure 3.
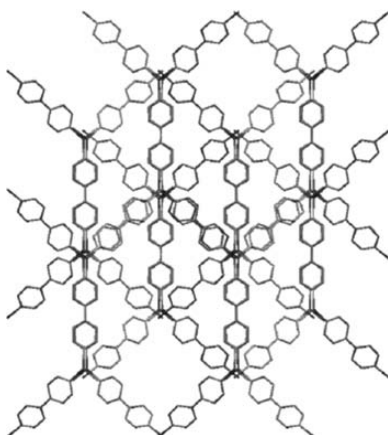
Figure 2. Crystal structure of $[Cu(4,4'-bpy)_{1.5}](NO_3)\cdot(H_2O)_{1.25}$. Nitrate anions and water molecules are omitted. Figure taken from ref.[72]
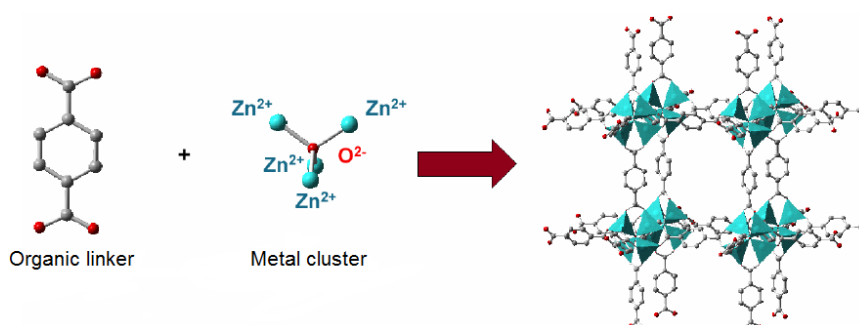
Figure 3. Schematic representation of synthesis and formation of MOF-5. Figure taken from ref.[73]

This solid material with the chemical formula of $[Zn_4O(BDC)_3]$ was synthesized under solvothermal condition from zinc nitrate and organic dicarboxylic acid.[62] The ZnO_4 tetrahedra are joined by benzene dicarboxylate linkers to form an extended 3D cubic framework.

Similar to MOF-5, a strategy of MOF synthesis based on reticulating metal ions and organic carboxylate linkers into extended networks created, a series of MOFs from Zn clusters with different dicarboxylate linkers has been prepared. The series of sixteen MOFs namely from IRMOF-1 to IRMOF-16 in which IRMOF stands for "isoreticular" metal-organic frameworks, has the same network topology and the first IRMOF-1 is MOF-5.[27] The representative linkers used and the corresponding IRMOFs are presented in Figure 4 and Figure 5. They are all highly crystalline materials in which several ones are mesoporous with pore diameters ranging from 21.4 Å to 28.8 Å and the open space represented up to 91.1% of the crystal volume.[27]
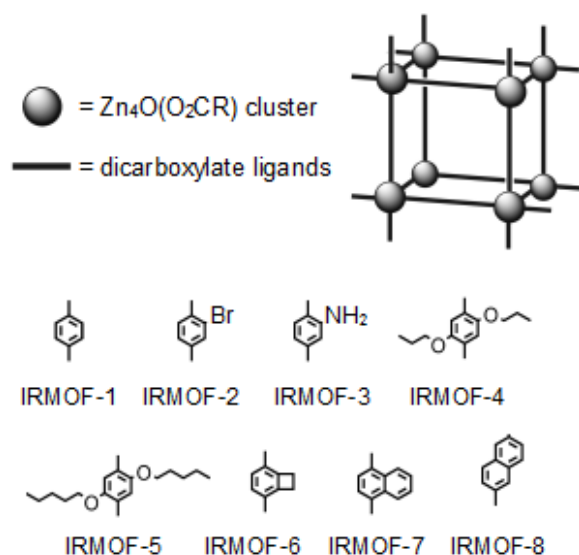
Figure 4. Dicarboxylate linkers used in the preparation of IRMOFs. Figure taken from ref.[27,74]
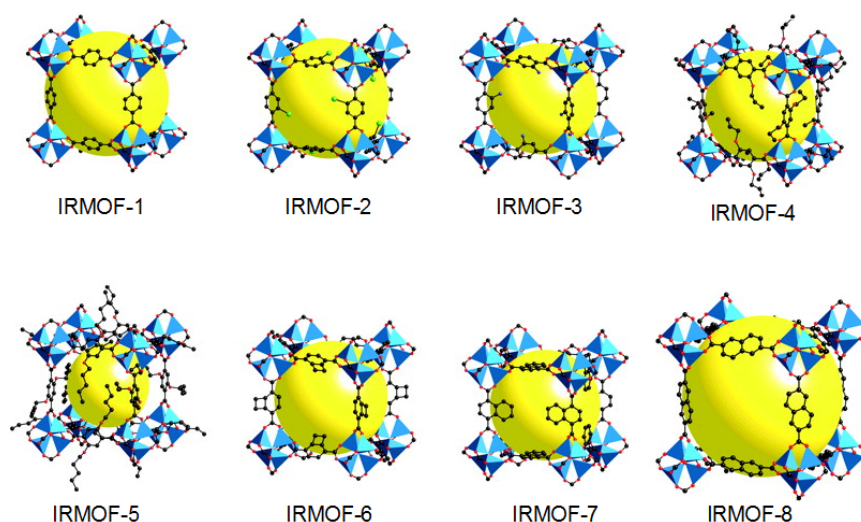
Figure 5. Zinc-based IRMOFs. Zinc: blue; carbon: black; yellow sphere: corresponding cavity. Figure taken from ref.[27,74]

A variety of metal clusters and organic linkers have been used for the synthesis of MOFs.[75] So, other MOFs, e.g., so-called MIL-type (MIL, Mátérial Institut Lavoisier),[4] $[Cu_3(BTC)_2]$ namely HKUST-1[76] or MOF-199[76,77] have been synthesized by using the different metal centers like Cr, Fe, and Cu and the linkers like benzene di/tricarboxylic acids exemplifying the diversity of the "world" of porous MOFs. The porosity of several examples of MOFs is shown in Table 2.

Moreover, by using the concept of "soft" templating with structure-directing agents developed for the synthesis of ordered mesoporous silicates like MCM-41,

mesoporous MOFs based on MOF-199[78-80] and MIL-53(Al)[81] containing additional meso- or nano-scale pores (pore diameter of 2–50 nm) have been prepared recently.

Table 2. The porosity of several examples of MOFs.

Name	Chemical formula	Pore size (Å)	Window size (Å)	Specific surface area (cm^2 g^{-1})	Pore volume (cm^3 g^{-1})	Ref.
MOF-5	[Zn$_4$O(O$_2$C–C$_6$H$_4$–CO$_2$)$_3$]	12	8	2900	0.61–0.54	[62]
IRMOF-3	Zn$_4$O[O$_2$C–C$_6$H$_3$(NH$_2$)–CO$_2$]$_3$	10.15	<8	2160	0.63	[27,82]
HKUST-1/ MOF-199	[Cu$_3$$\{$(C$_6H_3$–(CO$_2$)$_3$$\}_2$] or [Cu$_3(BTC)_2$]	9.0	-	692	0.33	[76,77]
MIL-53	Al(OH)[O$_2$C–C$_6$H$_4$–CO$_2$]·[HO$_2$C–C$_6$H$_4$–CO$_2$H]$_{0.70}$	8.5	8.5	1140	0.57	[83,84]
MIL-100	Cr$_3$F(H$_2$O)$_3$O[C$_6$H$_3$–(CO$_2$)$_3$]$_2$	25–30	4.8–8.6	3100	1.16	[85]
MIL-101	Cr$_3$X(H$_2$O)$_2$O[(O$_2$C–C$_6$H$_4$–CO$_2$)]$_3$, X = F/OH	29–34	12–14.7	5900	2.38	[4]

2.2.2. Synthesis of MOFs

The synthesis of MOFs is usually carried out at low temperature (< 250 ^{o}C) and mostly under solvothermal condition. In general, two solutions containing the metal and the organic components are mixed together and thermally treated (in a glass vessel or an autoclave) for crystallization at desired synthesis conditions. The main parameters of the synthesis are pH, concentration, and temperature in which the temperature is of the most important one.[86] The common polar solvents such as water, dimethyl/ethyl formamides, dimethyl sulfoxide or acetonitrile are frequently used in MOF synthesis. The characteristics of the ligand as bond angles, molecular length, etc. and of the metal ion play a very important role in the structure of MOF.[12]

The concept of isoreticular synthesis has been developed by Yaghi and co-workers (Figure 6). By changing one or both of organic linker/ligand and inorganic unit, MOFs with different pore sizes are created. In general, many metal atoms in their stable oxidization states, i.e., alkaline, alkaline-earth, transition metals, main group metals, and rare-earth elements, have been successfully used in the synthesis of MOFs.[55] For organic components, a variety of linkers can be utilized for MOF

synthesis. However, the most common organic linkers are derived from polycarboxylic acid or bipyridines of different size.[55]
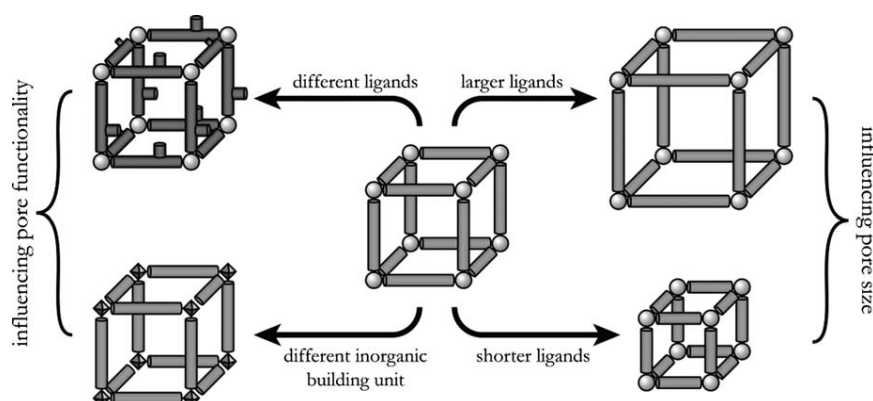
Figure 6. Schematic representation of the concept of isoreticular synthesis. Figure taken from ref.[1]

Besides, the microwave irradiation has been used for the synthesis of MOFs.[87-92] The advantage of this method is that a wide range of temperature and fast internal heating can be applied to shorten the crystallization time.[90,91,93] A study carried out by Morris and co-workers showed that the MOF samples synthesized under microwave conditions are purer and of higher crystallinity.[94]

2.2.3. Structure and porosity of investigated MOFs

2.2.3 1. Small pore-sized MIL-77 and MIL-96

A small pore-sized MOF namely **MIL-77** with the chemical formula of $[Ni_{20}\{(C_6H_8O_4)_{20}(H_2O)_8\}]\cdot33H_2O$ is synthesized in an autoclave under autogenous pressure using 3-methylglutarate linker.[95] Its nickel oxide metal clusters are connected with the glutarate organic linkers forming a complex 3D framework of helical octahedral chains and very large intersecting 20-membered ring tunnels as shown in Figure 7.

It shows an open 3D network of edge-sharing nickel octahedral. This complex framework is generated by two independent nickels: Ni1 located on the threefold axis and Ni2 on the twofold one. The two independent nickels contain octahedral coordination. Each Ni1 octahedron shares three edges with three Ni2 octahedra each Ni2 octahedron shares two of its *trans* edges with two neighboring Ni1 octahedra.

And the complex oxide group can be simply described from helixes running along the *a* axis, where Ni1 and Ni2 polyhedra alternate (Figure 7a). Each helix is connected with four out-of-phase parallel neighboring ones (above and below, and in front and behind), through a third Ni2 octahedron, which produces corrugated twenty-membered rings (Figure 7b). That also brings the formation of perpendicular helixes in this chiral structure. The twenty-membered rings interconnect with each other (Figure 7c) to create crossing tunnels as shown in (Figure 7d).[95]
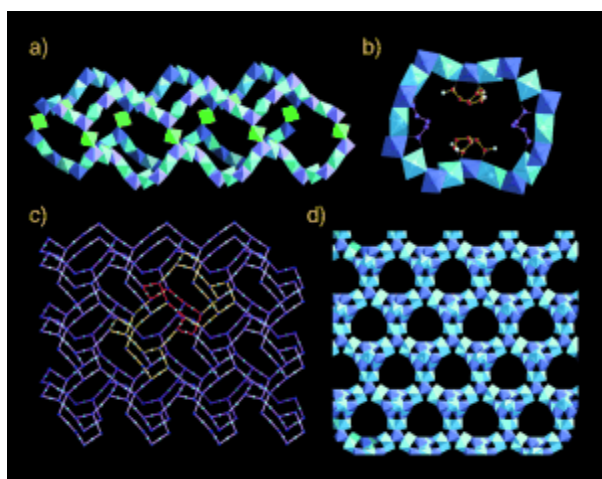
Figure 7. The structure of MIL-77. a) View of four helixes with alternating Ni1 (mauve) and Ni2 (pale blue) connected by Ni2 octahedra (green), b) polyhedral view of a corrugated twenty-membered ring with the two independent glutarate ions; the orange one is disordered with statistic occupancy of 2/3, c) view of the nickel network showing interconnected rings, and d) view of the nickel oxide tunnels down. Figure taken from ref.[95]

The TGA investigation shows that high weight loss only occurrs at *ca.* 350 °C due to the oxidization of organic linkers. The MIL-77 is stable in moisture or water. However, the specific surface area of this material of *ca.* 170 $m^2 g^{-1}$ is rather low compared to open porous MOFs structure. The pore of MIL-77 started with the glutaric acid is already small and becomes smaller due to the methyl group attached to the middle of the short $O_2C–C–C–C–CO_2$ linker. According to Guillou et al., the pores are found to be inaccessible.[96]

MIL-96, an aluminum benzene tricarboxylic acid based MOF with the formula $Al_{12}O(OH)_{18}(H_2O)_3(Al_2(OH)_4)(BTC)_6 \cdot 24H_2O$ is hydrothermally synthesized under autogeneous pressure in an autoclave from starting materials including aluminum nitrate and 1,3,5-benzenetricarboxylic acid (trimesic acid or H_3BTC) in water.[97] The MIL-96 structure owns a 3D framework containing isolated trinuclearμ_3-oxo-bridged

aluminum clusters and infinite chains of $AlO_4(OH)_2$ and $AlO_2(OH)_4$ octahedra forming a honeycomb lattice based on 18-membered rings. The framework possesses three types of cages in which the first two types are bigger than the other. Figure 8 shows a 3D framework of MIL-101 consisting of octahedral aluminum linked through the trimesate ligand, $[BTC]^{3-}$.
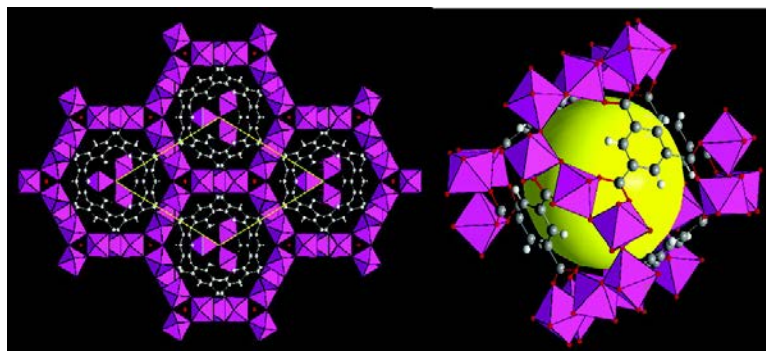
Figure 8. The structure of MIL-96. The hexagonal network of the aluminum octahedra (pink) containing 18-membered rings connected to the µ3-oxo-centered trinuclear units, via the trimesate ligand. Carbon: grey; cavity: yellow. Figure taken from ref.[97]

(a)   (b)
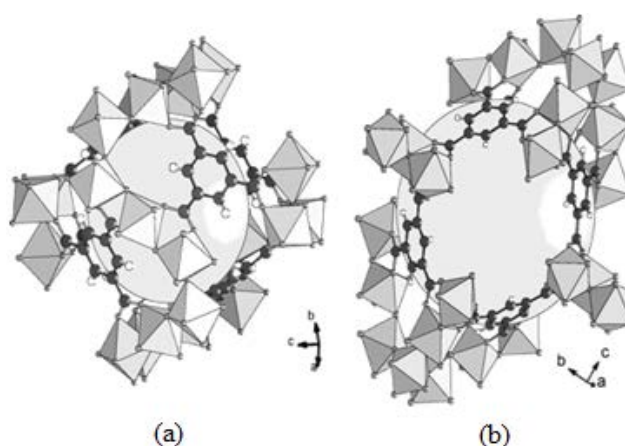
Figure 9. The two large cages of MIL-96. The light gray spheres indicate the empty cavity. Figure taken from ref.[97]

The two big cages are shown in Figure 9. The free diameter of the first one (Figure 9a) is estimated to be *ca.* 8.8 Å with a pore volume of *ca.* 420 Å^3. The second one (Figure 9b) is elongated and has a larger pore volume of *ca.* 635 Å^3. The pore-opening diameters of these large cages are of *ca.* 2.5−3.5 Å. The third cage is smaller compared to the first two big ones and has no empty space.[97] The BET surface area of MIL-96 is *ca.* 530 $m^2 g^{-1}$.[98] MIL-96 is thermally stable until the decomposition of the structure with the departure of the trimesate species at *ca.* 300 °C.[97]

2.2.3.2.   Medium pore-sized MOF-5 and IRMOF-3

A material with the formula unit [$Zn_4O(O_2C–C_6H_4–CO_2)_3$], so called **MOF-5** or **IRMOF-1**, was firstly synthesized by Yaghi et al. in 1999.[62] It is one of the most known MOFs synthesized using zinc nitrate and benzene dicarboxylic acid as organic linker under solvothermal condition. Its structure (Figure 10) consists of ZnO_4 tetrahedra which are joined via the organic linkers to give an extended 3D cubic framework.

Zinc: blue;
Oxygen: red;
Carbon: grey.
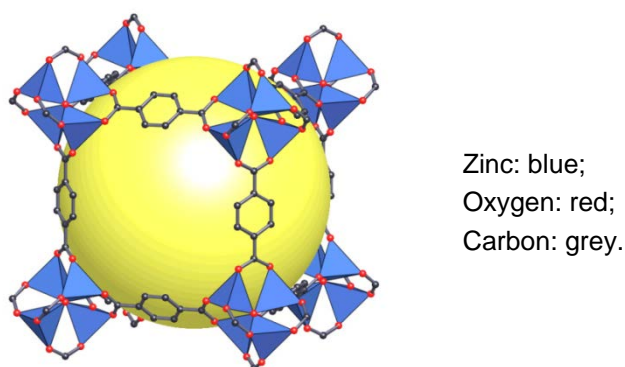
Figure 10. The structure of MOF-5. Figure taken from ref.[62]

The topology of the structure (primitive cubic net) is shown in Figure 11. The framework is very open with extraordinarily ordered edges connected by angles of 90°. It contains an ordered set of internal, intracrystalline pores with a diameter size of *ca.* 12 Å and with interconnecting pore apertures of *ca.* 8 Å.[62] This makes MOF-5 accessible for large molecules and interesting for applications in adsorption and catalysis.[62]

In comparison with conventional materials such as zeolites, MOF-5 has higher surface area of *ca.* 2900 $m^2 g^{-1}$ (BET) and pore volume of 0.61–0.54 $cm^3 g^{-1}$. The density of the material is very low, only 0.59 $g cm^{-3}$. MOF-5 is thermally stable up to 300 °C.[62] However, likely most zinc-based MOFs, MOF-5 is known to be sensitive to moisture due to the relative weak metal–oxygen coordination.[99-102] Therefore, it should be applied in non-aqueous condition.
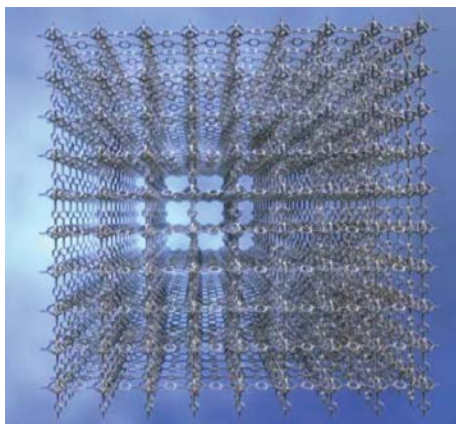
Figure 11. An overview of the MOF-5 framework. Figure taken from ref.[103]

IRMOF-3 with the unit formula $Zn_4O[O_2C–C_6H_3(NH_2)–CO_2]_3$ is an amino-functionalized (2-amino benzene dicarboylate linker) MOF and is isostructural with MOF-5 (Figure 12).[27]

Since one hydrogen atom of the organic linker is substituted by amore space demanding amino group, the free diameter of the pores with 10.15 Å,[82] is smaller than that of MOF-5 with 12 Å. The pore openings/pore apertures are also somewhat reduced (*ca.* 7.8 Å) compared to MOF-5 (*ca.* 8 Å). It has also high specific surface area of *ca.* 2160 m^2 g^{-1} (BET).[82] The IRMOF-3 is thermally stable up to nearly 400 ^{o}C.[82] It is less moisture-sensitive than MOF-5, which is obviously due to the amino group in the benzene ring of the linker. It is stable even when it is exposed to the ambient air for several days.[99]
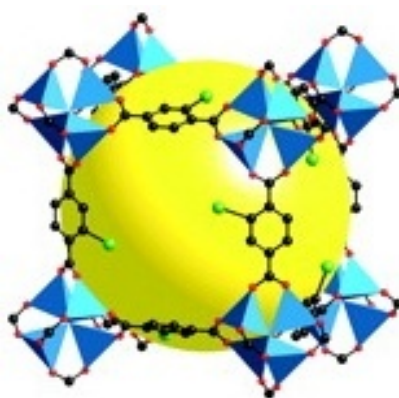
Zinc: turquoise;
Oxygen: red;
Carbon: black;
Amino –NH$_2$: bright green.

Figure 12. The structure of IRMOF-3. Figure taken from ref.[27]

2.2.3.3. Large pore-sized MIL-101

The large porous MOF namely MIL-101 is composed of inorganic trimeric octahedral chromium metal building blocks and alternating arranged organic 1,4-benzene dicarboxylate linkers (Figure 13).[4] They form so-called supertetrahedral secondary building units (ST), which build up the ordered and highly porous crystalline framework of the chemical composition $Cr_3X(H_2O)_2O[(O_2C–C_6H_4–CO_2)]_3 \cdot nH_2O$ (where n is *ca.* 25, X = F/OH).
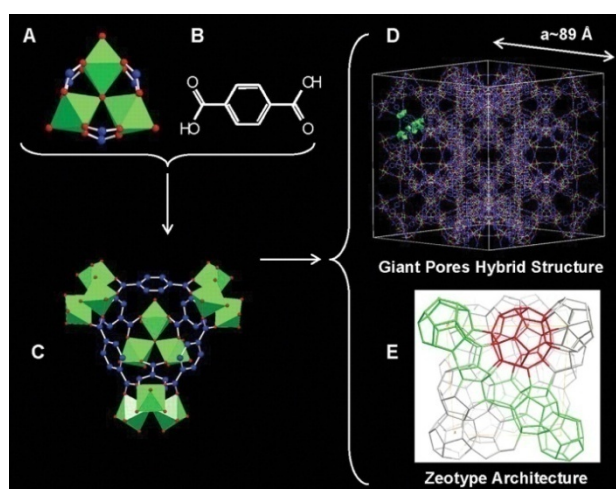
Figure 13. The structure of MIL-101. (A) Trimeric octahedral chromium building block chelated by carboxylic functions. (C) Supertetrahedral secondary building units (ST) with triangular pore openings created by (A) and (B) terephthalic acid. (D) Ball-and-stick representation of one unit cell, highlighting one ST drawn in a polyhedron mode. (E) Schematic 3D representation of the zeotype architecture (the vertices represent the centers of each ST) with the small (in green, with 20 ST) and large (in red with 28 ST) cages delimited by the vertex sharing of the ST. Chromium octahedra, oxygen, fluorine, and carbon atoms are in green, red, and blue, respectively. Figure taken from ref.[4]

The pore system of MIL-101 consists of two different large-sized cages with the internal free diameters of *ca.* 29 Å and *ca.* 34 Å, respectively, as shown in Figure 13(E) and Figure 14. They are present in a 2:1 ratio and correspond to the accessible pore volumes of *ca.* 12700 $Å^3$ and *ca.* 20600 $Å^3$, respectively. The smaller cage is accessible via pentagonal windows of *ca.* 12 Å size, whereas the larger one has both pentagonal and hexagonal windows with the diameters of *ca.* 12 Å and *ca.* 14.7 x 16 Å, correspondingly (Figure 14). These two cages are delimited by 20 and 28 ST units, respectively.
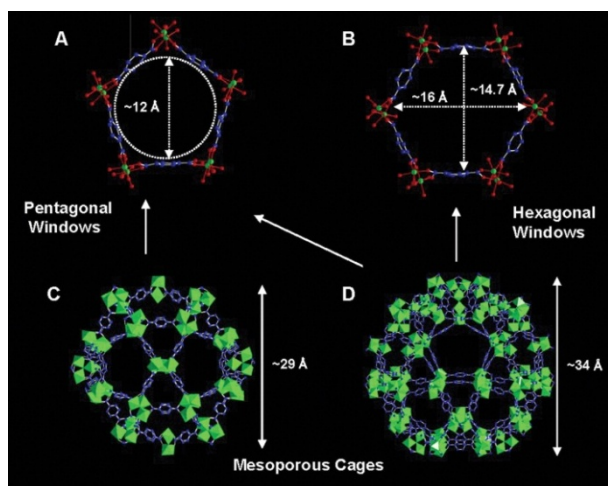
Figure 14. Pore openings and structures of MIL-101. The pentagonal and hexagonal windows (A and B) of the two mesoporous cages (C and D) containing triangular pore entrances of the ST units to the large cages. Figure taken from ref.[4]

The four vertices of ST unit are occupied by the trimers of chromium while the organic linkers are located at the six edges of the ST unit (Figure 13C). It is important to note that the ST unit is microporous with trigonal pore openings of *ca.* 8.6 Å[4] and can be considered as "side pockets" of the walls of the large cavities.[3] As a result, MIL-101 is not only a mesoporous material but also a microporous one. It is confirmed by the N_2 sorption isotherm of the dehydrated sample (Figure 15).[4] It belongs to the type I (according to IUPAC) with nitrogen uptakes at $p/p_0 = 0.1$ and at $p/p_0 = 0.2$ indicating the presence of the two kinds of pores. Especially, MIL-101 exhibits an extremely high specific surface area of *ca.* 5900 m^2 g^{-1} and pore volume of *ca.* 2.0 cm^3 g^{-1}. It shows high thermal stability in air up to 275 ^{o}C. Different from zinc-based MOFs, MIL-101 is stable over months in air and is not altered when it is treated with various organic solvents at room temperature or under solvothermal conditions.[4]
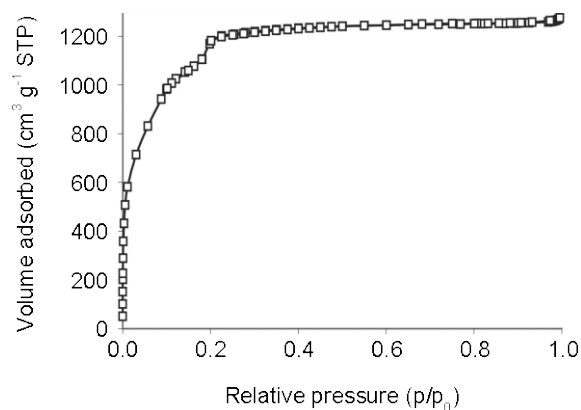
Figure 15. Nitrogen sorption isotherm of MIL-101 at 78 K. Figure taken from ref.[4]

16

These above properties, especially specific surface area, porosity, and stability make MIL-101 an attractive candidate for catalysis even with large molecules.

2.2.3.4. Extra-large mesostructured MOFs

Different from above described MOFs including the medium pore-sized MOF-5 and IRMOF-3 as well as the large porous MIL-101, which is considered as the small mesoporous MOF, the mesostructured MOF materials having 3D-nanostructures with well-defined mesoscale (2–50 nm) pores have been recently created. The introduction of meso and nanoporosity into MOFs is expected to overcome pore size and mass transfer constrains. The concept of "soft" templating used for the synthesis of mesoporous silicates shown in Figure 16 has applied for the preparation of mesostructured MOFs, so-called MesoMOFs.[79-81]
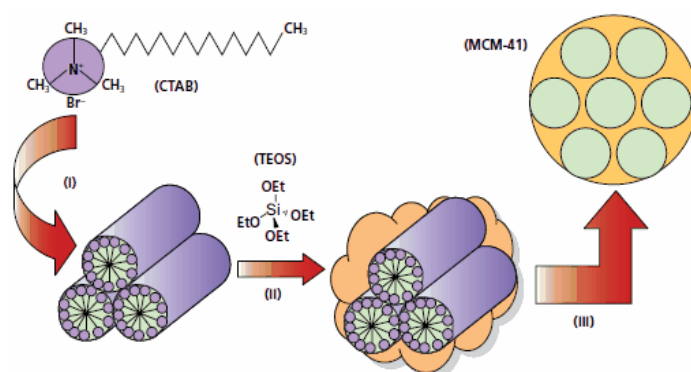
Figure 16. Schematic synthesis of mesoporous silica MCM-41. Figure taken from ref.[104]

In Figure 16, the surfactant CTAB is used as a structure-directing agent to form liquid crystalline micelles in water (I). Then the sol-gel precursor, e.g., tetraethylortho-silicate (TEOS), is added to this micellar solution to make, upon hydrolysis and condensation, a silica network around the micelles (II). At last, the removal of the organic template is carried out by the thermal treatment (calcination) or the solvent extraction yielding a ceramic mesoporous material, in this case hexagonally ordered MCM-41 silica framework (III).

Based on this concept, a mesostructured MOF derived from MIL-53(Al) has been successfully prepared recently.[81] Similarly, another mesostructured MOF based on MOF-199 (also called as HKUST-1) was synthesized by using CTAB with/without TMB as structure-directing agents.[78] It is shown that, depending on the amount of

17

the agents, the hierarchically micro and mesoporous MOFs are created. The porosity of a MOF example containing mesopores is given in Table 3.

Table 3. Synthesis conditions and the porosity of the hierarchically micro and mesoporous MOFs created from Cu^{2+} and $[BTC]^{3-}$. Data taken from ref.[78,105]

Sample	Molar ratio $Cu^{2+}/H_3BTC/CTAB/TMB$	S_{BET} ($m^2 g^{-1}$)	V_t ($cm^3 g^{-1}$)	V_{meso}/V_{micro}	Mesopore diameter (nm)
0	MOF-199[105]	1555	0.710		
1	1:0.556:0.15:-	1225	0.609	0.24	3.8
2	1:0.556:0.30:-	1124	0.597	0.34	3.9
3	1:0.556:0.60:-	905	0.560	0.44	5.6
4	1:0.956:0.30:0.15	579	0.505	1.43	31.0
5	1:0.956:0.30:0.30	533	0.517	1.64	23.0
6	1:0.956:0.30:0.60	1124	0.575	0.24	4.9
7	1:0.956:0.60:0.30	738	0.514	0.78	14.9

Applying the same concept, mesostructured MOF samples based on MIL-101 namely MesoMIL-1 and MesoMIL-2 (MesoMILs) have been prepared and will be discussed in the following parts. It is expected that, by changing the amount of the structure-directing agent, different meso-sized MOFs could be achieved. The mesostructured MOFs possiblely overcome the mass transfer hindrance in catalysis application, especially for very large or bulky molecules.

2.3.   Supported catalysts and catalyst supports

2.3.1.   Supported catalysts

Supported catalysts, as the definition by the Kirk-Othmer encyclopedia of chemical technology, are solid or heterogeneous catalysts in which relatively small amount of catalytically active species, frequently metals, are deposited on the surface of largely inert, porous, and shaped support bodies, which are sometimes referred to carriers.[106] The use of supported catalysts is connected with a couple of advantages:[107,108]

- Increased specific surface area of active species;
- Improved catalytic activity by high dispersion of active species;
- Improved size and shape selectivity by using defined pore structures, e.g., zeotype materials;

- Improved mass transfer by textural or internal porosity;

- Stabilization of the active species;

- A wide range of temperature and pressure in use;

- Material and cost savings, especially by using noble metals (e.g., Rh, Pd, Pt, Au);

- Easy recovery and separation from reaction mixtures;

- Easy to handle;

- Reduced toxic, easy and safe disposal;

- Immobilization of homogeneous catalysts in order to combine the advantages of homogeneous and heterogeneous catalysis.

Single site concept:

Materials with defined pore systems and high specific surface areas like zeolites or mesostructured silicates are preferential materials for the preparation of so-called single site catalysts which are expected to distinguish oneself by markedly improved catalytic properties. Based on the concept of site isolation, such catalysts can be engineered by controlled deposition of metal precursor on the catalyst support followed by controlled decomposition as shown in schematic representation Scheme 1 and Scheme 2. Gates and co-workers demonstrated that highly uniform rhodium or ruthenium species at the atomic scale could be prepared on the crystalline zeolite support.[109,110] It has been found that the organometallic precursor reacts with OH groups located in Al sites of the zeolite leading to dissociation of acetylacetonate (acac) ligands from the precursor and connecting the obtained metal species with a zeolitic support via two metal–oxygen bonds (Scheme 1 and Scheme 2).

$$M(acac)(CO)_2 \ + \ 2 \, HO(O)Al \longrightarrow M(CO)_2[O_2Al] \ + \ Hacac–HO(O)Al$$

Scheme 1. Schematic representation of reaction of a metal complex with an acidic site of zeolite. Scheme taken from ref.[110]

R (Rh–C) = 2.10 Å

R (Rh–O) = 2.21 Å

R (Rh–Al) = 3.02 Å
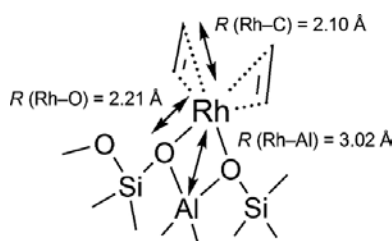
Scheme 2. Schematic representation of new bonds of metal–zeolite, $M(CO)_2[O_2Al]$. Scheme taken from ref.[109]

Similar to zeolite, MOFs are considered as zeolite-like, zeotype, materials. In contract to inorganic zeolites and related materials like AlO_4, MOFs are inorganic-organic hybrid materials in which the metal clusters are strictly alternating connected with the organic linkers forming the repeated hybrid metal-organic frameworks. They are highly crystalline defined materials with very large specific surface areas, high porosity, and designable pore sizes. These unique properties make them superior to other microporous systems and can facilitate the formation of highly dispersed active sites in a single site manner.

Confinement and shape and size selectivity:

Microporous and mesoporous materials with defined pore system has been shown size and shape selectivity. This behavior is assigned to the confinement effect occurred at the surface or in the pores and to the structures and pore sizes of catalysts in which the reactions take place. The concept of confinement in microporous zeolites was developed by Derouane et al. in the late 80s of the last century. It describes the interaction between the guest molecule and the catalyst host and the relation to catalysis.[111,112] It has been concluded that the confinement of the molecule in the pore, cage or surface hole (surface curvature or the wall of mesopores) results in a significant increase of activity and selectivity provided that the pore size of the catalyst and the molecule are similar. A schematic representation of the van der Waals energy (W) between a spherical guest molecule and a micropore is shown in Figure 17.[112]
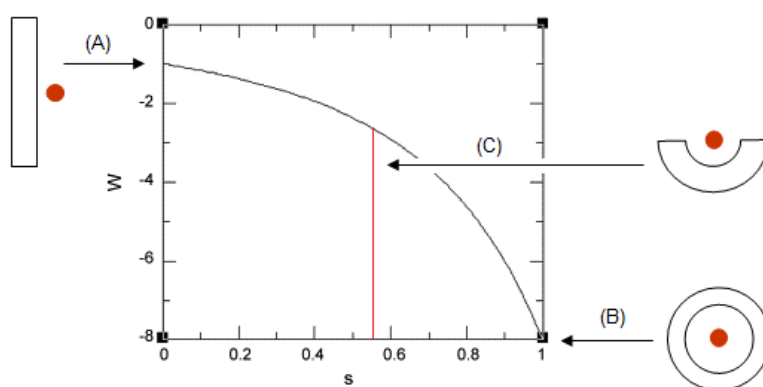
Figure 17. The van der Waals energy (W) between a spherical molecule (radius *d*) and a spherical micropore (radius *a*) with the $s = d/a$ parameter. (A) $s = 0$ corresponds to a sorbate on a flat surface, (B) $s = 1$ corresponds to a sorbate matching the pore size, and (C) $0 < s < 1$ corresponds to a sorbate on a curved surface. Values of *W* are relative to the flat surface case. Figure taken from ref. [112]

It is importantly noted that the adsorption energy in the zeolite pores can be up to 8 times larger than that of a flat surface (in cases: $s = 1$ compared to $s = 0$). Additionally, the formation of transition states during the course of catalytic reaction is affected by the pores of catalysts. For instance, the enhanced selectivity to *para*-xylene is observed in the alkylation of toluene with methanol over Pt@H-ZSM-5 catalyst (Figure 18) compared to the more bulky *o*- and *m*-isomers.[113,114] Similarly, the effect of the structure and pore channels of zeolites were observed in alkylation of biphenyl with propylene over different zeolites.[115]

(a)   (b)
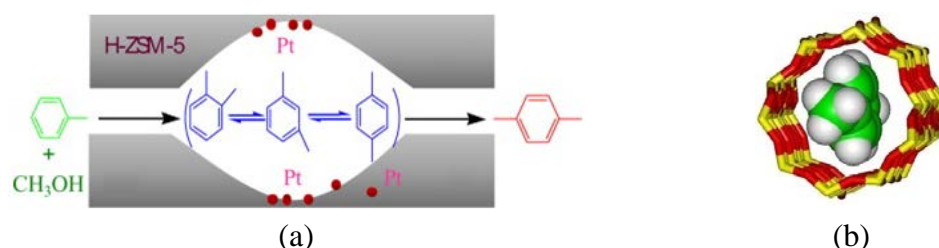
Figure 18. (a) Shape selectivity in alkylation of toluene with methanol over Pt@H-ZSM-5 catalyst and (b) *para*-xylene matching the channels of zeolite.[114,116]

Similar to zeolites, the confinement effect/surface curvature possibly happens in zeotype MOFs due to a variety of the structures and pore sizes. The effect might result in improved diffusion, activity, and shape selectivity when MOFs are in use as catalysts or catalyst supports

2.3.2. Catalyst supports

In heterogeneous catalysis, Al_2O_3, zeolite, SiO_2, TiO_2, and activated carbon are widely used as catalyst supports. It is because they possess high surface areas and pore volumes, high stability, and availability with reasonable costs.

Al_2O_3 is commonly used as a catalyst support, especially in the reforming process in petroleum refining. This inorganic material is highly thermal stable under the reforming reaction condition as well as under harsh catalyst regeneration in which coke deposited on the catalyst is burnt at a very high temperature. Similarly, zeolites are also widely used as catalysts and catalyst supports, especially a large amount used in FCC units of most refineries. As well crystallized materials with defined pore system, high surface area and pore volume, and highly thermal stability, they are

commonly used to engineer catalysts with accelerated catalytic activity and shape selectivity in harsh catalytic processes.

Additionally, ordered mesoporous inorganic materials such as MCM-, SBA-, MSU-, and others[117,118] have attracted attention of the scientist in the last two decades due to their potential applications in which big molecules are involved. Due to the improved pore sizes, the activity and mass transfer can be enhanced. The properties of several porous support materials are shown in Table 4.

Table 4. Overview of textural properties of several porous catalyst supports.[17,119]

Support	Surface area ($m^2\,g^{-1}$)	Porosity	Thermal stability
Al_2O_3	< 300	meso–macro	high
SiO_2	< 1000	micro–meso	high
Zeolites	< 600	micro	high
Mesoporous silica alumina materials	< 2000	meso	high
Activated carbon	500–2000	micro–macro	low–medium
MOFs	up to 10400	micro–meso	low–medium

Porous metal-organic frameworks are new emerging class of materials and of interest as catalyst supports by the improved porosity. However, due to the inorganic-organic hybrid nature the thermal stability and in part hydrolytic stability are lower compared to inorganic materials. Therefore, these materials are mainly of interest for the application at least severe catalytic reaction condition, e.g., as support active sites in fine chemical reaction and catalysis with enzymes.

2.4. Hydroformylation

2.4.1. Hydroformylation reaction

The hydroformylation is the reaction of an olefin with one equivalent each of CO and H_2 to form linear and branched aldehydes, as shown in Scheme 3.
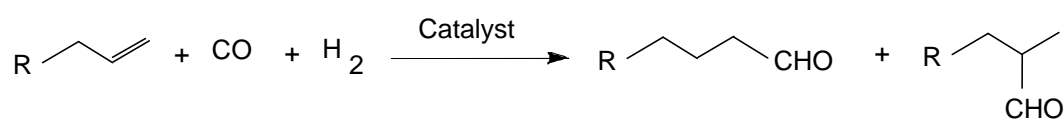
Scheme 3. Hydroformylation reaction.[120]

The reaction proceeds only in the presence of a catalyst. In general two reactions compete with the hydroformylation reaction.[121]

(i) Hydrogenation:
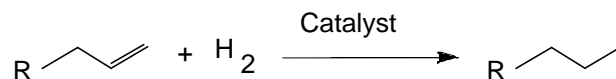
(ii) Isomerization of terminal alkene to internal alkene (double bond shifted reaction):
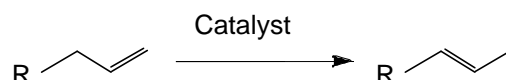
In the hydroformylation of a terminal alkene, the regioselectivity, i.e., the *n/i*-aldehyde ratio, is an important parameter of the catalytic performance. Moreover, depending on the catalyst, the ligand used, and reaction conditions, the selectivity to aldehydes is varied. The unbranched terminal olefins such as *n*-but-1-ene, *n*-hex-1-ene, *n*-oct-1-ene, etc. are usually more reactive than branched and/or internal ones. The order of reactivity of unsaturated substrates is presented in Scheme 4.
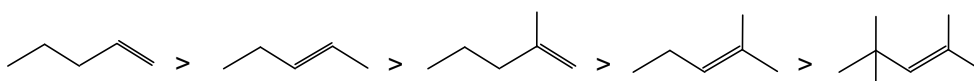
Scheme 4. The olefin reactivity in hydroformylation. Scheme taken from ref.[122]

Aldehydes are important intermediates for production of fine chemicals. Many intermediates/products can be achieved from aldehydes, e.g., alcohols via hydrogenation, carboxylic acids via oxidation, and amines via reductive amination. Aldolization is the starting point for branched alcohols, carboxylic acids, and amines with double carbon number.[123] An overview of uses of aldehydes is present in Figure 19.

The hydroformylation reaction only proceeds in the presence of a catalyst. Metals, especially rhodium and cobalt, can be used for this reaction; however, their activities are very different. The order of hydroformylation activity for unmodified monometallic catalysts clarifies as bellowed.[35]

Rh >> Co > Ir, Ru > Os > Pt > Pd > Fe > Ni

Cobalt catalysts completely dominated industrial hydroformylation until the early 1970's when rhodium catalysts were commercialized. In 2004, it was estimated that about 75% of all homogeneous hydroformylation processes were based on rhodium catalysts.[124]
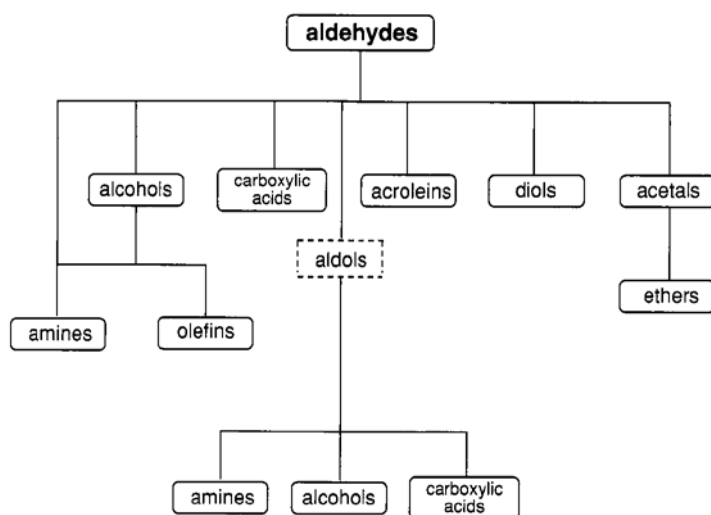
Figure 19. Compounds accessible through hydroformylation. Figure taken from ref.[35]
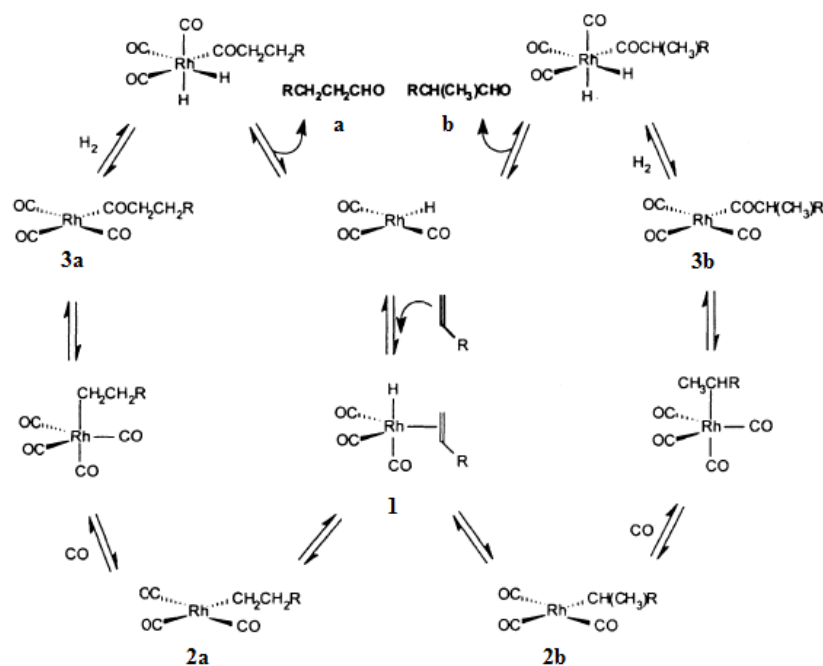
Figure 20. Mechanism of rhodium-catalyzed hydroformylation. Scheme taken from ref.[125]

The proposed mechanism of the hydroformylation of an alkene (a typical vinyl) is shown in Figure 20. On the onset of the hydroformylation, the Rh precursor reacts with synthesis gas to form the catalytic active rhodium hydride tricarbonyl species.

This compound coordinates the alkene generating the π-complex (1). The complex is rearranged via internal hydrogen transfer into the alkyl-rhodium intermediates (2a and 2b). The insertion of an additional CO molecule into this intermediate provides the acyl-rhodium species (3a and 3b). At the end of the catalytic cycle, these species interact with hydrogen via an oxidative addition, producing aldehyde (a and b) and generating the rhodium hydride tricarbonyl species.[125]

2.4.2.   Effects of temperature, pressure and solvent

Systematic studies on the influence of temperature on the hydroformylation of vinyl substrates in the presence of unmodified rhodium-based precursors have been carried out.[125] An increase of reaction temperature results in an enhancement of both the reaction rate of hydroformylation and that of isomerization of the double bond. In the reaction of oct-1-ene using Rh(CO)2(acac), a slight increase of the *n/i*-aldehyde ratio, from 1.5 at 50 ^{o}C to 2.1 at 90 ^{o}C, is observed.[126] However, the amount of isomerization products (internal octenes) is increased from 3% to 24% at 50 ^{o}C and 90 ^{o}C, accordingly. Another investigation of the influence of temperature on the hydroformylation of hex-1-ene in the presence of $Rh_4(CO)_{12}$ is shown in Figure 21. The yield of linear aldehyde increases along with increasing temperature, from 52% at 20 ^{o}C to 72% at 100 ^{o}C.
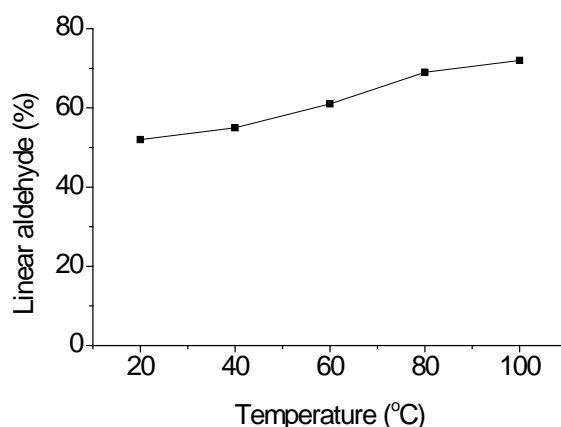
Figure 21. Influence of temperature on the hydroformylation of hex-1-ene in the presence of $Rh_4(CO)_{12}$ as catalyst precursor. Figure taken from ref.[125]

Relating to pressure, it has been shown that, in the hydroformylation of styrene, the CO and H_2 partial pressures affect the reaction regioselectivity, i.e., *n/i*-aldehyde ratio, only when the reaction is carried out at a high temperature. A decrease of CO or

H_2 partial pressure causes an increase of selectivity to linear aldehyde, especially at the high temperature of 100 $^{\circ}$C. For instance, in the hydroformylation of styrene at 100 $^{\circ}$C, the *n/i*-aldehyde ratio changes from 20/80 at 170 bar of CO/H_2 (1:1) to 44/56 at p_{H2} = 6 bar and p_{CO} = 85 bar or to 40/60 at p_{H2} = 85 bar and p_{CO} = 6 bar.[125] On the contrary, in the hydroformylation of *n*-hex-1-ene, the pressure does not affect the reaction regioselectivity neither at room temperature nor at high temperature. However, the chemoselectivity, i.e., the aldehyde selectivity, increases with an increasing temperature. The aldehyde products/isomerization products changes from 44/56 (or aldehyde selectivity of 44%) at 40 bar to 77/23 (or aldehyde selectivity of 77%) at 140 bar.[125]

Apart from temperature and pressure, solvent also influences the results of hydroformylation. In the liquid phase, the solvent is used to solubilize reactants, especially synthesis gas, and to facilitate the heat transfer and might affect both the activity of catalyst and the selectivity of the transformation. In common organic solvents, the solubilities of H_2 and CO are in the range of 2–10 mol m^{-3} bar^{-1}.[35] For instance, the solubilities of H_2 and CO in toluene are 3.1 mol m^{-3} bar^{-1} and 10.5 mol m^{-3} bar^{-1}, accordingly.[127]

3. Results and discussion

In this part, the results of the catalyst preparation and the catalytic testing in the hydroformylation of olefins are presented. The structural properties of the catalysts based on MOF are investigated by the different characterization methods. The catalytic performance of each Rh@MOF will be discussed in comparison with the others to figure out the possible effects of the structural properties of the supports on the catalytic behaviors.

3.1. Material and characterization

3.1.1. MOF-5

The crystallinity and the structure of as-synthesized MOF-5 and Rh@MOF-5 were checked by XRD. The XRD patterns are shown in Figure 22. They are similar to the calculated pattern and in agreement with previously reported pattern of MOF-5.[29,128,129]
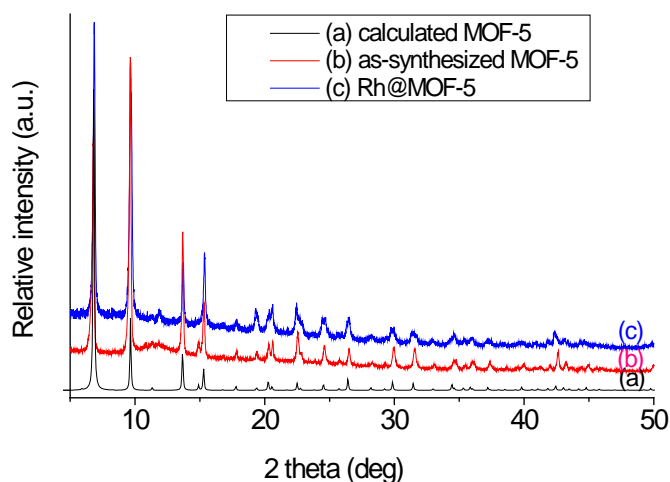
Figure 22. XRD patterns of MOF-5.

The TEM image of as-synthesized MOF-5 is shown in Figure 23. It shows that as-synthesized MOF-5 consists of well crystallized elongated nanocrystals. The crystals are uniform shaped with the dimensions of *ca.* 40–50 x 200 nm. The crystals tend to agglomerate (Figure 23). No indication of additional intraparticle nanoporosity is found in TEM.
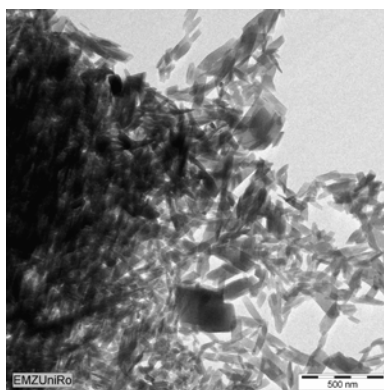
Figure 23. TEM image of as-synthesized MOF-5 showing nano-sized particles.

FTIR spectra of the MOF-5 sample and the Rh@MOF-5 supported catalyst in the spectral range of 500–2500 cm^{-1} are shown in Figure 24. They are very well resolved and show the typical vibration bands observed of benzene carboxylate, which is presented as a linker. The spectra are dominated by strong absorbances between about 1350–1600 cm^{-1} and 740–825 cm^{-1}. These bands are related to vibration modes of carboxyl groups and different $=$C–H modes of the phenyl groups. The FTIR lattice vibration spectra shows no indication for partial hydrolysis of the MOF usually indicated by a high frequency shift of the carboxyl vibration band at 1610 cm^{-1} to 1690–1760 cm^{-1}.
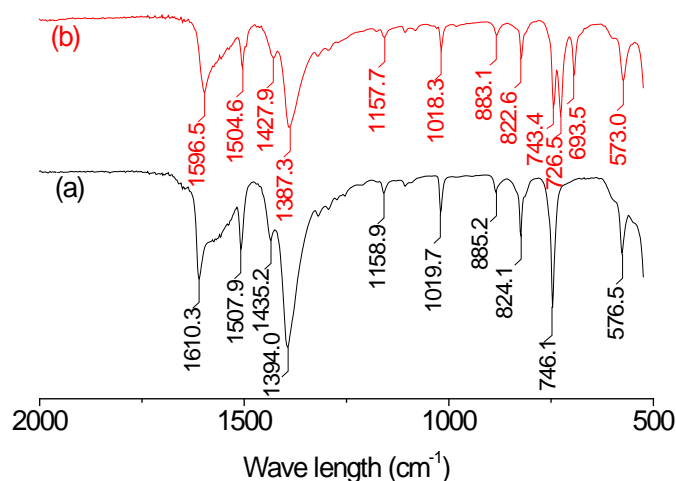
Figure 24. FTIR spectra of nano-sized (a) MOF-5 and (b) Rh@MOF-5.

Interestingly, Rh loading leads to a markedly low frequency shift of this and other vibration bands by 15–10 cm^{-1} and splitting of the 746 cm^{-1} linker vibration band of the benzene even the Rh loading is low. These changes indicate that the Rh is located in the framework of MOF-5. The rhodium seems to be highly dispersed. No larger

metal particles could be detected in the TEM images. Indeed, detailed studies on noble metal supported MOF-5 materials show that the M(cod)(cot) complex is decomposed and reduced to M(0) by hydrogenolysis under hydrogen atmosphere. Thereby small metal nanoclusters are formed.[68] It is expected that the same happens in the case of the Rh@MOF-5 catalyst with much lower Rh loading.

The specific surface area and pore volumes of materials were studied by nitrogen adsorption and desorption measurements. The isotherm shown in Figure 25 belongs to the type I according to the IUPAC nomenclature.[130] At low relative pressure up to $p/p_0 = 0.01$, the steep slope of the isotherm indicates the filling of the micropores of MOF-5. The further slightly increase of the nitrogen uptake up to a relative pressure $ca. \ p/p_0 = 0.5$ is due to adsorption in small mesopores having diameters of 2–5 nm. TEM shows no intraparticle mesoporosity. Therefore, these pores are due to textural porosity between the MOF nanoparticles. The BET surface area and specific pore volume of MOF-5 are 2337 $m^2 \ g^{-1}$ and 1.0 $cm^3 \ g^{-1}$, respectively.
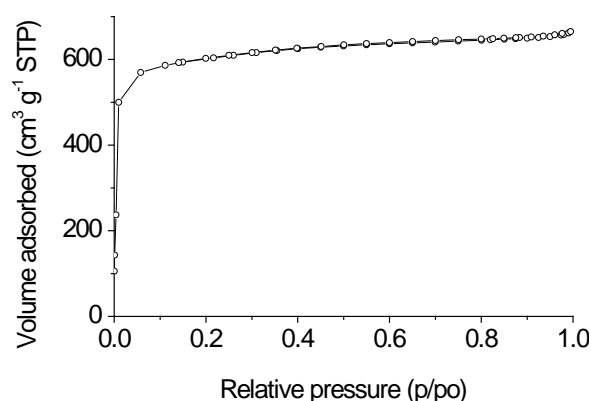
Figure 25. Nitrogen adsorption and desorption isotherms of MOF-5 measured at 77 K.

In the XPS spectrum of MOF-5, a strong signal of C_{1s} appears at 285.08 eV and the other, which is relatively weak, appears at higher energy of 289.39 eV. Their peaks are all asymmetric. A single asymmetric O_{1s} peak appears at 532.59 eV. Only the signal of Zn_{2p} appears as a doublet peak rising at 1023.09 eV and 1046.17 eV. It is highly asymmetric. A rhodium signal could not be identified in the XPS spectrum of Rh@MOF-5 sample. It is likely due to the relatively low rhodium loading on MOF-5. However, the loading, even very low, has a strong impact on the C_{1s}, O_{1s}, and Zn_{2p} signals of Rh@MOF-5. Significant electron binding energy shifts of *ca.* 0.48–1.45 eV to lower energy are observed after rhodium loading (Table 5). The shifts indicate a

strong interaction between the rhodium and the MOF framework. However, the shifts of binding energy to lower energy range are not similar for the different elements. Large shifts are observed with O_{1s} and Zn_{2p} signals (Table 5). This finding points to the location of rhodium near the O and Zn atoms. In other words, the rhodium is likely located close to the metal cluster of the MOF framework.

Table 5. Electron binding energies of the elements of MOF-5 before and after loading rhodium species.

Signal	Binding energy (eV)	
	MOF-5	Rh@MOF-5
C_{1s}	285.08	284.60
	289.39	288.77
O_{1s}	532.59	530.40
		531.89
Zn_{2p}	1023.09 (1/1)	1021.98 (1/1)
(doublet)	1046.17 (1/2)	1045.04 (1/2)

In conclusion, MOF-5 has been successfully synthesized. The material is well crystallized and consists of uniform elongated nanocrystals in the size of 40–50 x 200 nm. It is microporous and exhibits a high specific surface area of 2337 m^2 g^{-1} and a pore volume of 1.0 m^3 g^{-1}. The results of FTIR and XPS investigations point to a high dispersion of the supported rhodium in the MOF structure, a strong interaction of the Rh with the support, and that it is located close to the metal cluster of the MOF framework.

3.1.2. IRMOF-3

The X-ray diffraction patterns of as-synthesized IRMOF-3 and the used Rh@IRMOF-3 catalyst in comparison with the calculated pattern are shown in Figure 26. The reflections are well resolved and the observed patterns correspond to the structure of IRMOF-3.[60,101] The similarity of XRD patterns obtained for as-synthesized and the used rhodium loaded material indicates that the structure of the MOF framework is maintained after Rh loading and even after catalytic testing. The FTIR spectra of the as-synthesized form and the supported catalyst are shown in Figure 27. They are very well resolved and show the typical vibration bands observed with benzene carboxylate present as a linker. The absorbances observed between 1600–1330 cm^{-1}

and 830–750 cm^{-1} are related to the vibrations of the carboxyl group and different =C–H modes of the amino substituted phenyl group. The very strong vibration band located at *ca.* 1255 cm^{-1} in both samples are assigned to the C–N stretch vibrations of amino groups attached to the benzene ring. The spectra of the as-synthesized material and the rhodium loaded form are quite similar.
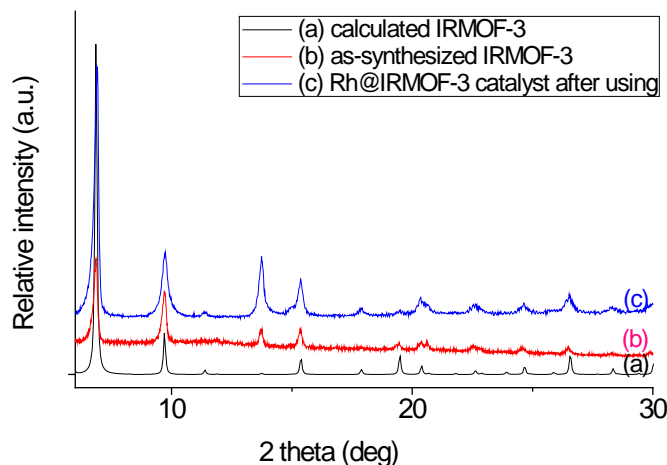
Figure 26. XRD patterns of IRMOF-3.
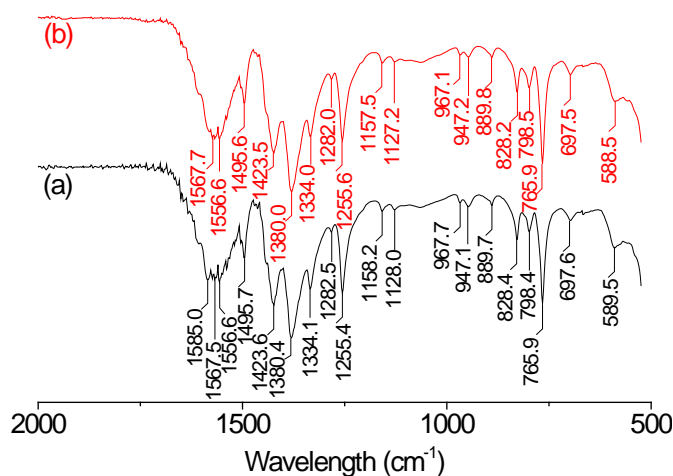
Figure 27. FTIR spectra of (a) IRMOF-3 and (b) Rh@IRMOF-3.

The SEM/TEM images of IRMOF-3 and Rh@IRMOF-3 in different magnifications are shown in Figure 28 and Figure 29. The starting material consists of large block- and cube-shaped particles of *ca.* 150–350 μm size. They show well-shaped and smooth faces. However, they are easily broken into compartments during handling. The big particles show cracks (Figure 28a and b). The high magnification image shows, however, that these large particles do not represent single crystals. They consist of agglomerates of much smaller, *ca.* 0.5 μm sized particles (Figure 28c).

31

Interestingly, the TEM image shows that these small particles are composed of nanoparticles of *ca.* 10–15 nm size (Figure 28d). Hence, the big, close to mm-sized, as-synthesized IRMOF-3 particles consist of agglomerated small nanoparticles, which are hierarchically assembled (10 nm → 0.5 μm → 300 μm), into large size compartments.

(a)

(c)

(b)

(d)
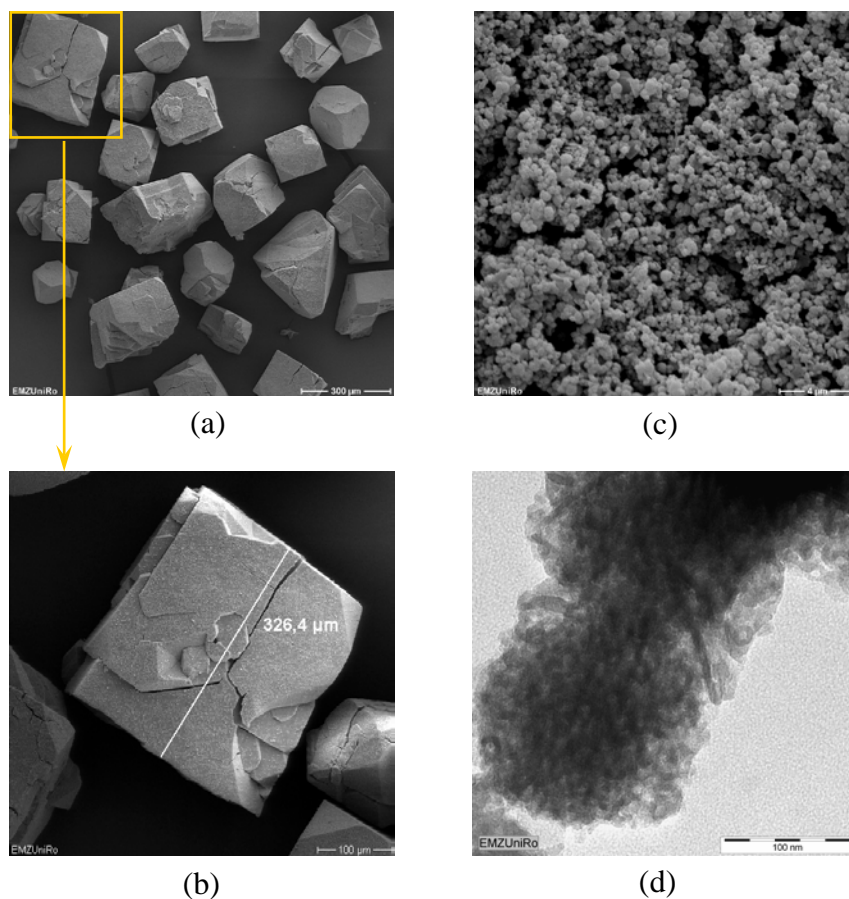
Figure 28. SEM/TEM images of IRMOF-3. (a) SEM image of block- and cube-shaped particles, (b) SEM image of a large particle with smooth faces and cracks, (c) high magnification SEM image of a big particle showing high textural porosity and hierarchically arranged μm-sized particles, (d) TEM image showing agglomerated nanoparticles forming the μm-sized particles.

After rhodium loading, which is connected with heating and stirring of the sample followed by evaporation of the solvent, the particles show some damages. The former large particles are broken into compartments of irregular shapes (Figure 29a). The faces of the particles are rough. Their edges and corners are more rounded. The particles show cracks and slits (Figure 29b).

(a)   (b)
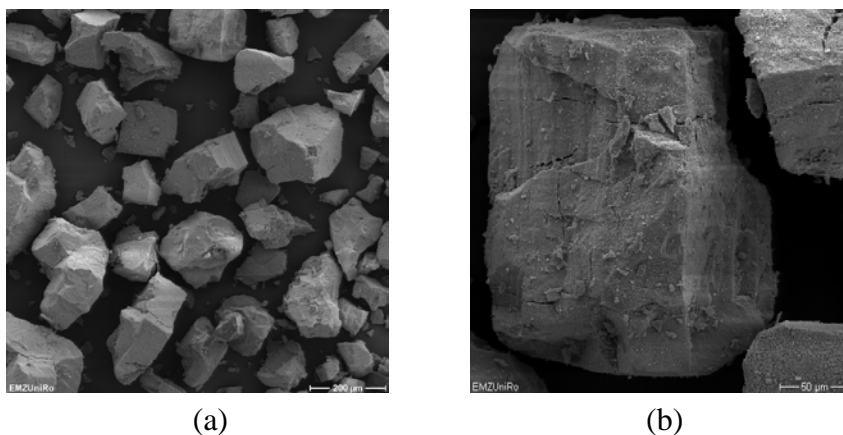
Figure 29. SEM images of Rh@IRMOF-3. (a) Overview showing irregular sized large particles and (b) a selected big cubic particle showing rough faces and cracks/slits.
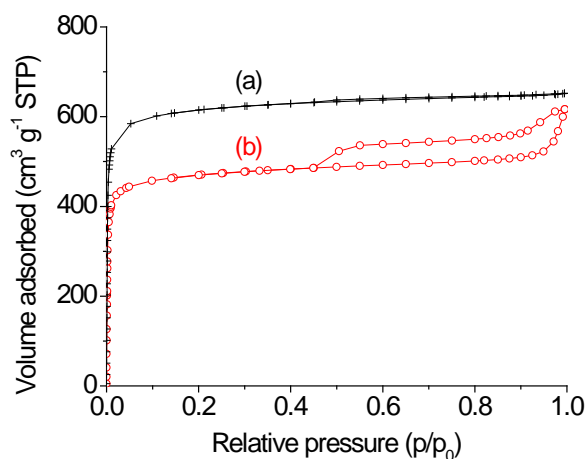
Figure 30. Nitrogen adsorption and desorption isotherms of (a) IRMOF-3 and (b) Rh@IRMOF-3 measured at 77 K.

The nitrogen adsorption-desorption isotherms of IRMOF-3 and its Rh supported catalyst are shown in Figure 30. At low relative pressure of up to $p/p_0 = 0.01$, the extremely steep increase of the isotherm indicates the filling of the micropores. The enhancement of the nitrogen uptake between a relative pressure of $p/p_0 = 0.01–0.2$ shows the filling of the open pores of the MOF. The isotherm of Rh@IRMOF-3 shows a similar appearance. The BET surface area of the starting material amounts to *ca.* 2450 m^2 g^{-1} and the specific pore volume to *ca.* 0.96 cm^3 g^{-1} showing high crystallinity and porosity of IRMOF-3. After rhodium loading, the BET surface area and the specific pore volume markedly decrease to *ca.* 1874 m^2 g^{-1} and *ca.* 0.73 cm^3 g^{-1}, respectively, indicating partial crystal damage. Also a second desorption step at $p/p_0 = 0.5$ is observed in the isotherm indicating the presence of (intraparticle) textural mesopores of *ca.* 4 nm size that could improve the accessibility of the pore

33

system of the Rh@IRMOF-3. The starting material contains already such mesopores but to a much lower extent. The shape of the hysteresis loop of the isotherm is consistent with the presence of slit-like pores. The loop is flat and the curves are parallel indicating parallel pore walls.[131,132] Also the formation of ink-bottle neck pores cannot be excluded which give rise to a similar hysteresis loop.[133] The loss of porosity and the occurrence of the textural porosity after rhodium loading are in line with SEM results.

Table 6. Electron binding energies of elements of IRMOF-3 before and after loading rhodium species.

Peak	Binding energy (eV)		
	MOF-5	IRMOF-3	Rh@IRMOF-3
N_{1s}	-	399.27	398.23
			401.00
C_{1s}	285.08	284.80	281.15
	289.39	288.52	284.80
			288.73
O_{1s}	532.59	532.93	529.60
			531.14
Zn_{2p}	1023.09 (1/1)	1023.98 (1)	1019.47 (1/1)
	1046.17 (1/2)	1047.08 (2)	1021.92 (2/1)
			1042.72 (1/2)
			1045.03 (2/2)

In the XPS spectrum of IRMOF-3, a Zn_{2p} signal (doublet) appears at 1023.98 eV and 1047.08 eV. The peaks are asymmetric. A single asymmetric O_{1s} peak appears at 532.93 eV. Additionally, the N_{1s} peak at 399.27 eV is highly asymmetric. Two C_{1s} signals are located at 284.8 eV and 288.52 eV. Additionally, a shoulder arises at *ca.* 293 eV. In comparison with MOF-5, the electron binding energies of Zn_{2p}, O_{1s}, and C_{1s} are somewhat similar (Table 6). It is understandable since IRMOF-3 is isostructural with MOF-5. However, in details, the C_{1s} signal of IRMOF-3 appears at a fairly lower energy (284.80 eV and 288.52 eV) compared to that of MOF-5 (285.08 eV and 289.39 eV), whereas both the O_{1s} and the Zn_{2p} ones arise at rather higher energies (Table 6). It is due to the amino group attached to the benzene ring of the linker in case of IRMOF-3. Rhodium loading has a severe impact on the appearance and location of the Zn_{2p}, O_{1s}, and C_{1s} XPS signals, respectively, although the loading

is rather low. According to the AAS analysis, the sample contains only 0.11 wt% of rhodium. This finding points to a strong interaction between the Rh and the MOF lattice indicating that the Rh is located in the pores of the MOF and highly dispersed. Largest shifts to lower energy are observed with the Zn_{2p} and the O_{1s} signals of the metal oxide sites (Table 6). The latter signal is significantly broadened.

The N_{1s} signal is split into two components (Figure 31). A rhodium signal could not be unambiguously identified in the XPS. However, the marked changes observed after rhodium loading indirectly confirms the presence of the rhodium in the pore structure probably close to the metal oxide sites.
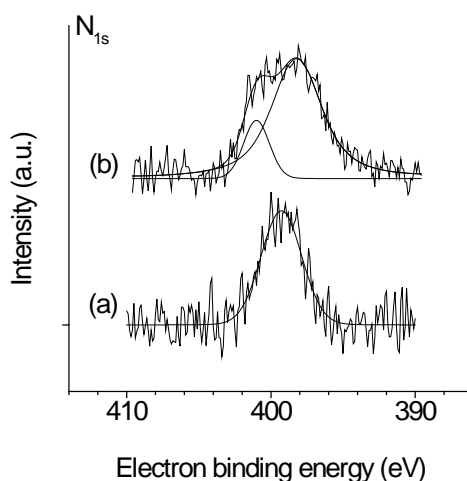
Figure 31. XPS N_{1s} spectra of (a) IRMOF-3 and (b) Rh@IRMOF-3 showing a split signal.

Finally, it is concluded that the catalytic material consists of agglomerated small IRMOF-3 nanocrystals. A high textural porosity of the catalytic material of 1874 m^2 g^{-1} for BET specific surface area and of 0.73 cm^3 g^{-1} for specific pore volume is achieved by hierarchically assembling of IRMOF-3 nanocrystals into 0.5 µm sized particles forming finally close to mm scale particles (up to *ca.* 330 µm). Thereby, a combined micro-meso-macro pore system is formed (Figure 28c, d). As a result, the catalytic sites would be highly accessible.

3.1.3. MIL-101

The crystallinity and structure of the synthesized MIL-101 sample was checked by powder X-ray diffraction (Figure 32). The obtained diffraction pattern is in agreement with the simulated one confirming the formation of the MIL-101 structure.[4,134] The

diffractogram shows resolved and narrow reflections indicating a well-crystallized material.
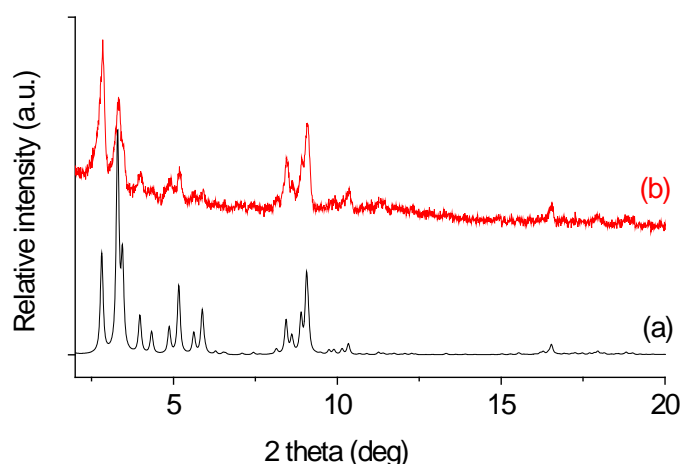
Figure 32. XRD patterns of MIL-101. (a) calculated pattern and (b) experimental pattern.
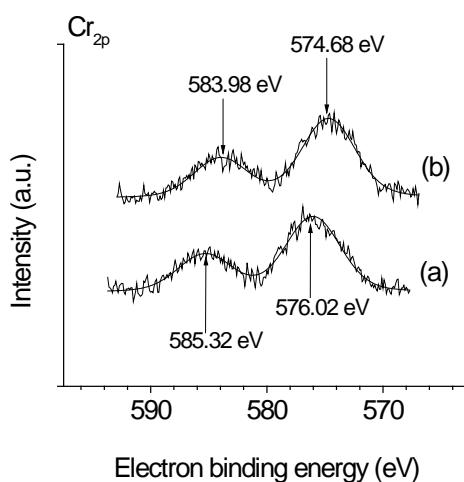
Figure 33. XPS spectra showing the Cr_{2p} doublet signal. (a) MIL-101 and (b) Rh@MIL-101.

The Cr_{2p} XP spectra of the starting MIL-101 and Rh@MIL-101 are shown in Figure 33. They show doublet signals with peak maxima arising at 585.32 eV and 576.02 eV in case of MIL-101 and 583.98 eV and 574.68 eV in case of Rh@MIL-101, respectively. This amounts to a significant shift of the signal maxima of 1.34 eV to lower energy. The shift indicates a strong interaction of the rhodium with chromium metal sites in the MOF structure even the rhodium loading was low. A less pronounced shift of 1.13 eV is observed with the O_{1s} signal. Only minor changes of 0.07–0.49 eV to lower energy are found with the C_{1s} signal, as shown in Table 7. The shifts confirm the location of the rhodium species in the framework nearby the

chromium and also oxygen (metal cluster). The rhodium loading was too low to be detected by XPS.

Table 7. Electron binding energies of elements of MIL-101 before and after loading rhodium species.

Peak	Binding energy (eV)		
	MOF-5	MIL-101	Rh@MIL-101
C$_{1s}$	*ca.* 282 (shoulder)	281.29	280.80
	285.08	284.82	284.77
	289.39	289.12	289.05
O$_{1s}$	532.59	530.80	529.67
Cr$_{2p}$	-	576.02	574.68
		585.32	583.98

FTIR spectra of MIL-101 and Rh@MIL-101 are shown in Figure 34. They are dominated by the vibration bands of the linker. They are well resolved and show the typical vibration bands usually observed with benzene carboxylate. The vibration bands occurring between 1630 cm^{-1} and 1390 cm^{-1} are related to vibrations of the carboxylate anion groups (1630–1500 cm^{-1}), C–O–H bending, or stretch in-plane bending modes (1440–1395 cm^{-1}) and deformation modes (1420–1340 cm^{-1}). CO–O and C–O stretching vibrations appear between *ca.* 1250 cm^{-1} and 1040 cm^{-1}. The bands below 900 cm^{-1} belong to different bending vibration bands of the C–H bonds (900–800 cm^{-1}) and =C–H deformation bands of the benzene ring (770–670 cm^{-1}). The vibration bands of the carboxyl groups might be overlapped by less intensive C=C stretch and ring vibrations of the benzene. Vibration bands of free carboxyl acid appearing at 1760–1690 cm^{-1} are not found. The latter finding confirms the purity and stability of the prepared MIL-101 sample. Interestingly, the rhodium loading causes only minor shifts (*ca.* 1 cm^{-1}) of the vibration bands to lower frequency. The largest shift of up to 3 cm^{-1} is observed with the carboxyl vibration band at *ca.* 1628 cm^{-1}. Additionally, a splitting of the vibration band located at 745 cm^{-1} is observed. This finding is in line with a location of the rhodium nearby the chromium sites as indicated by XPS. In contrast, significant shifts of the BDC linker vibrations to lower frequency of up to 15 cm^{-1} have been detected with MOF-5 at a similar low rhodium loading.[135]
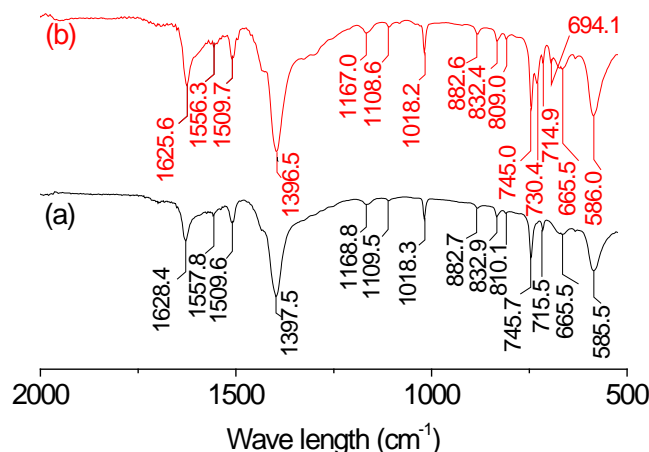
Figure 34. FTIR spectra of (a) MIL-101 and (b) Rh@MIL-101.

The SEM image of MIL-101 shows the formation of the well-shaped MOF particles during the course of the hydrothermal synthesis (Figure 35). The particles are agglomerated and in size of *ca.* 150–250 nm. The TEM measurement gives no indication of the formation of larger rhodium particles indicating that these active rhodium species are well dispersed in the MOF framework.
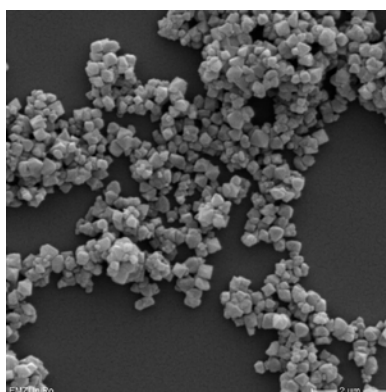
Figure 35. SEM image of Rh@MIL-101.

With an actual Rh loading of 0.15 wt% determined by AAS, *ca.* 1.2% of the trimeric chromium sites are occupied by Rh assuming an atomic (single site) metal distribution in the framework. This loading is high enough to provide a sufficient amount of single site rhodium species. The two large cages are surrounded by 20 or 28 ST units, which are constructed by four trimeric chromium sites. High dispersion of loaded rhodium is also indicated by chromium XPS data discussed above, which shows a substantial shift of the chromium signals even after low Rh loading.

SAXS measurements of the parent MIL-101 and Rh@MIL-101 (0.15 wt% Rh) catalyst have been performed to get additional information about the rhodium species. Because the SAXS data of MIL-101 and Rh@MIL-101 catalyst did not differ, higher loadings of 1% and 2% of Rh on MIL-101 have been included. The scattering curves of MIL-101 and Rh@MIL-101 (1 wt% Rh) in the q-range between 0.1 and 1, which is plotted as a log–log plot of the intensity I vs. the scattering vector q, are shown in Figure 36. They are nearly straight lines. The slope of log I vs. log q plot in the Porod regime[136,137] is between 3.8 and 4. The observed scattering is attributed to the particle surface structure of the MIL-101 particles, whereas a slope of near 4 indicates a smooth particle surface. The presence of nanoparticles would add an additional intensity in the q-range giving rise to a curved-shape of the plot.[138] In none of the samples additional scattering of small nano-sized Rh structures could be detected which is in line with above discussed findings of high dispersion of rhodium in the MOF.
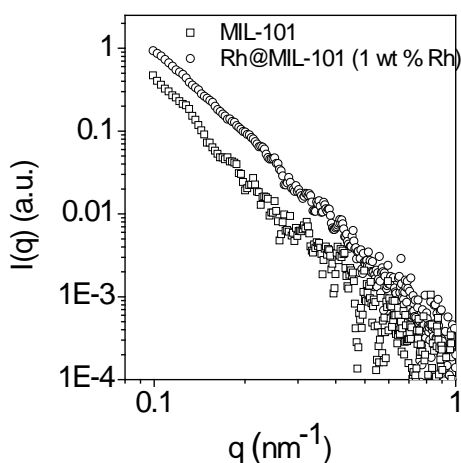
Figure 36. Scattering curves from SAXS measurements of MIL-101 and Rh@MIL-101.

The nitrogen adsorption-desorption isotherm of the sample is shown in Figure 37. The adsorption isotherm shows three distinct adsorption steps. At a very low relative pressure up to $p/p_0 = 0.01$, the uptake curve shows a very steep increase. It is assigned to the filling of micropores. Between the relative pressure of $p/p_0 = 0.01–0.2$, the slope of the adsorption isotherm decreases. This second step is related to the filling of small mesopores followed by a third step near $p/p_0 = 0.25$ of final pore filling. Further nitrogen uptake at the high relative pressure above $p/p_0 = 0.8$ is due to textural porosity. The overall course of the adsorption isotherm is characteristic for the MIL-

101 structure.[57] The well resolved adsorption steps of the isotherm and the high uptake confirms the formation of the well crystallized MIL-101. The BET surface area of the prepared MIL-101 is 4703 $m^2\,g^{-1}$, which is a high value compared to the other porous support materials. The specific pore volume amounts to 2.38 $cm^3\,g^{-1}$. The textural data also confirm the successful removal of excessive and difficult to remove terephthalic acid from the reaction mixture by the used repeated centrifugation procedure.
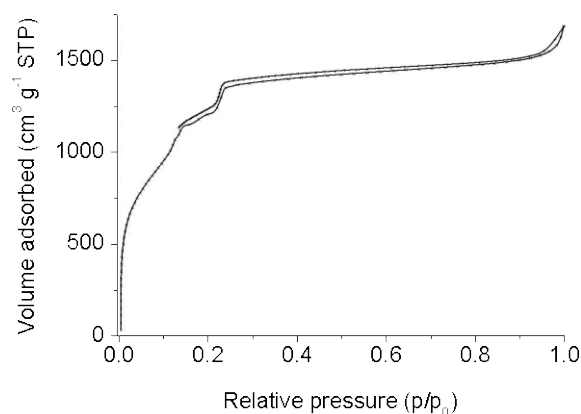
Figure 37. Nitrogen adsorption and desorption isotherm of MIL-101 measured at 77 K.

In summary, MIL-101 has been successfully synthesized in the presence of TMAOH. The material is well-shaped and has very high surface area of 4703 $m^2\,g^{-1}$ and pore volume of 2.38 $cm^3\,g^{-1}$. It is effective to remove the excess terephthalic acid by using the appropriate centrifugation regimes. Similar to Rh@MOF-5 and Rh@IRMOF-3, no signal of rhodium is detected by XPS measurement in the Rh@MIL-101 sample. Further investigation by SAXS indicates that small nano-sized rhodium structures could not be detected. It is therefore concluded that the rhodium sites in all Rh@MOF-5, Rh@IRMOF-3, and Rh@MIL-101 samples are highly dispersed in a single site manner at the atomic scale. As indicated by the XPS measurements for all considered Rh@MOFs, the rhodium active sites are likely located close to the metal cluster, and not at the organic linkers of the MOF structure.

3.1.4. MesoMILs

The XRD patterns of MesoMIL-1 and MesoMIL-2, which were obtained from collaboration with Vietnamese partner using CTAB as a structure-directing agent for the creation of mesopores, are shown in Figure 38. Although the obtained diffraction patterns are not completely coincide with the XRD pattern of MIL-101 (a sample for comparison), the obtained MesoMILs contain crystalline parts. The increase of diffraction intensity at very low angles is typically observed with mesostructured materials.
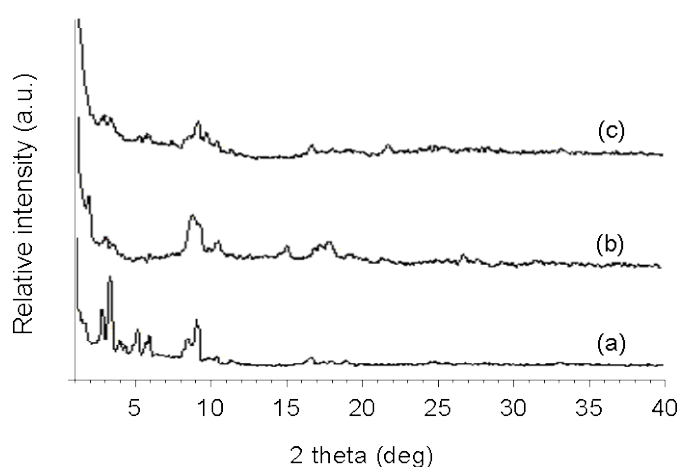
Figure 38. XRD patterns of (a) MIL-101, (b) MesoMIL-1, and (c) MesoMIL-2.

The SEM images of MesoMIL-1 and MesoMIL-2 in different magnifications are shown in Figure 39. In a low magnification image (Figure 39a), the irregular shaped and sized particles of MesoMIL-1 are observed. They are relatively big and of up to 200 μm. However, with MesoMIL-2 using more CTAB as the structure-directing agent in the synthesis process, the particles are much smaller (Figure 39b). The small micrometer particles are agglomerated to form bigger ones. In a higher magnification, it is clear that the big particles of MesoMIL-1 are composed of much smaller nanometer–micrometer agglomerated compartments (Figure 39c). In a high magnification, the big particle of MesoMIL-2 shows the rough surface (Figure 39d). For both the MesoMIL samples, the textural porosity could be created in between the small particles. This would enhance the mass transfer inside the MOF even though the MOF itself is already very porous due to its large pores.
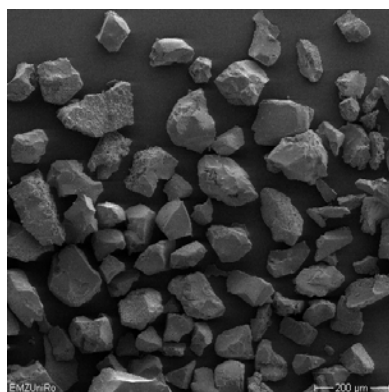
(a) MesoMIL-1
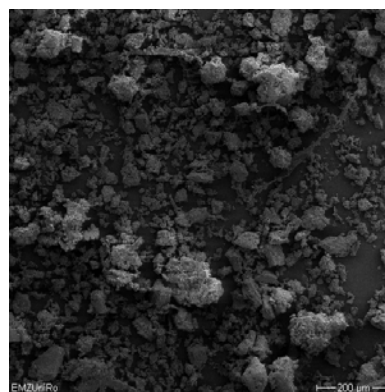
(b) MesoMIL-2
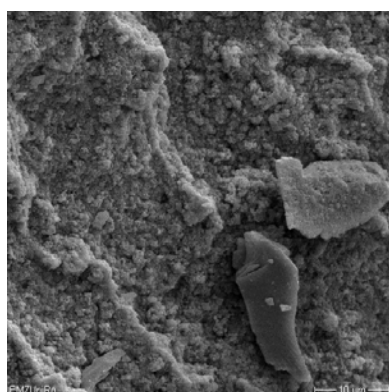
(c) MesoMIL-1
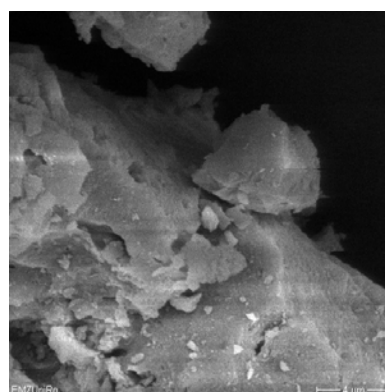
(d) MesoMIL-2
(the surface of a big particle)

Figure 39. SEM images of MesoMIL-1 and MesoMIL-2.

The TEM images of the two MesoMILs are shown in Figure 40. The nanoporosity is not found with the MesoMIL-1 sample (Figure 40a). However, it is clearly shown in the MesoMIL-2 sample (Figure 40b). This finding is reasonable since a bigger amount of CTAB is used in the synthesis of MesoMIL-2.
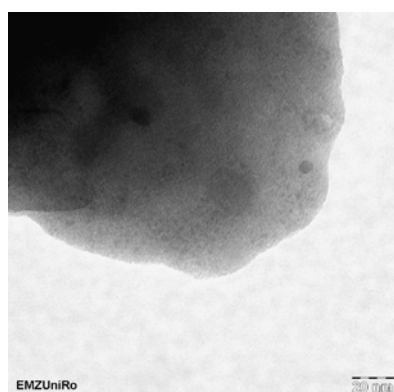
(a) MesoMIL-1
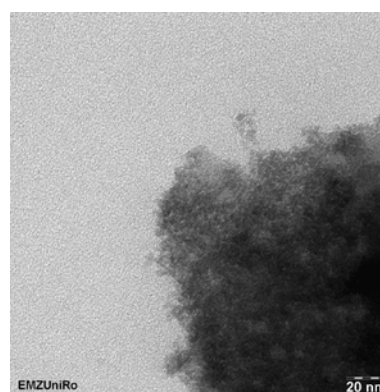
(b) MesoMIL-2

Figure 40. TEM images of MesoMIL-1 and MesoMIL-2.

The nitrogen adsorption-desorption isotherms of MIL-101 (a sample for comparison) and two MesoMILs are illustrated in Figure 41.
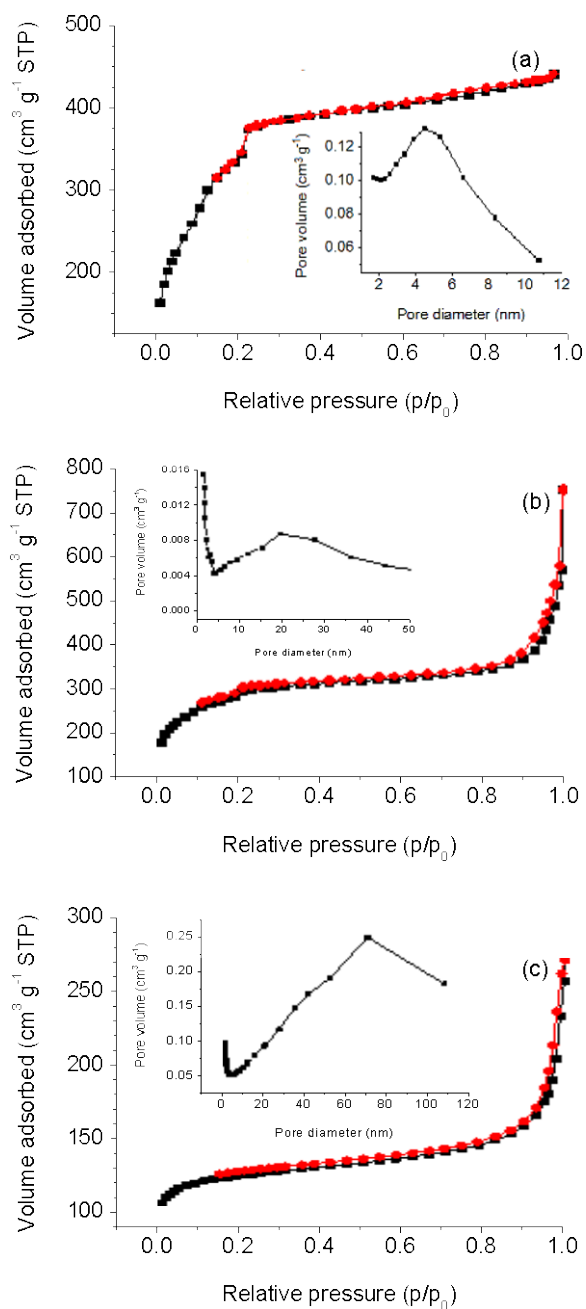
Figure 41. Nitrogen adsorption and desorption isotherms of MesoMIL-1 and MesoMIL-2.
(a) MIL-101 on the top, (b) MesoMIL-1 in the middle, and (c) MesoMIL-2 on the bottom.

In Figure 41a, the MIL-101 sample shows the typical isotherm found with the MIL-101 structure as discussed above. It contains already mesopores with a pore size maximum at *ca.* 4.5 nm. The influence of using the structure-directing agent on obtained synthesis product MesoMILs is clearly indicated in nitrogen sorption measurements. Even the typical course of adsorption is maintained, the nitrogen

uptake at the low relative pressure $p/p_0 = 0.25$ is reduced by *ca.* 30% in case of MesoMIL-1 in comparison with MIL-101. A notable second nitrogen uptake step above $p/p_0 = 0.8$ is observed in the isotherm of MesoMIL-1, which is related to the additional textural porosity with a maximum at *ca.* 20 nm induced by the CTAB template (Figure 41b). The isotherm shape of MesoMIL-2, a sample synthesized using more CTAB, is similar to that of MesoMIL-1 (Figure 41c). However, the nitrogen uptake up to $p/p_0 = 0.25$, which is related to the structural porosity of the MOF, is reduced by *ca.* 70% compared to that of MIL-101 and to *ca.* 60% compared to that of MesoMIL-1 (Figure 41). The MesoMIL-2 contains larger nanopores with a pore size maximum at *ca.* 70 nm in the pore size distribution plot (Figure 41c). This finding is in line with the observation of the nanoporosity in the TEM image of MesoMIL-2 (Figure 40b). The BET specific surface areas - the pore volumes are of (1500 m^2 g^{-1} - 1.6 cm^3 g^{-1}), (1000 m^2 g^{-1} - 1.0 cm^3 g^{-1}), and (470 m^2 g^{-1} - 0.5 cm^3 g^{-1}) for MIL-101, MesoMIL-1, and MesoMIL-2, respectively.

3.1.5.   MIL-77 and MIL-96

Two small pore-sized MOFs so-called MIL-77 and MIL-96 were provided by the counterpart in the University of Düsseldorf. Figure 42 presents the XRD pattern of MIL-77. The resolved and narrow reflections confirm the crystallinity of the material. The obtained diffraction pattern is in agreement with the previous result provided by Guillou et al.[96] confirming the formation of the MIL-77 structure.
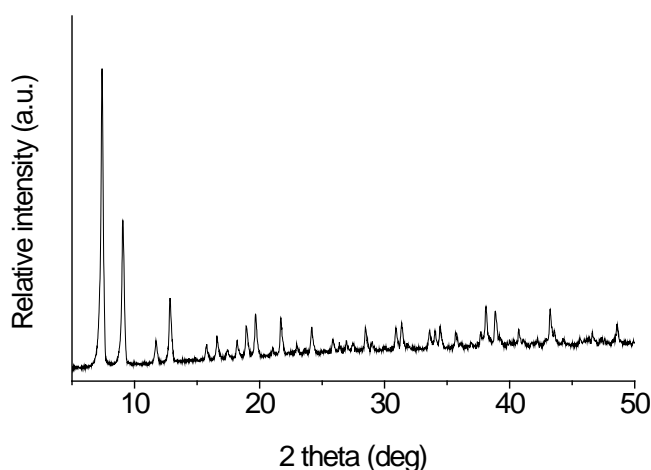
Figure 42. XRD pattern of MIL-77.

(a)	(b)
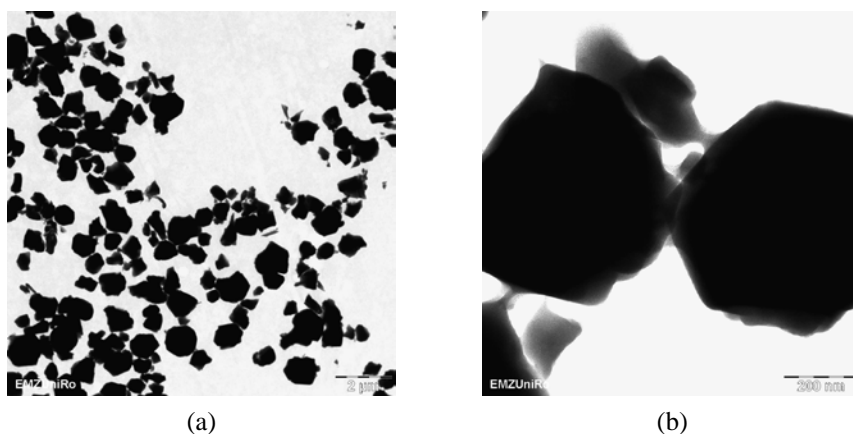
Figure 43. TEM images of MIL-77.

TEM images of MIL-77 in different magnifications are shown in Figure 43. The images show irregular sized and shaped particles with sizes ranging from nanometer to micrometer scale. The particles tend not to agglomerate and show no textural porosity. As the pore system is not accessible, catalysis can only occur at the outer crystal surfaces.

Figure 44 shows the XRD pattern of MIL-96, which contains only very narrow pore openings of *ca.* 3 Å size. Therefore, the relative large internal structural cavities are not available for molecules from outside. However, these cavities can modulate the external surface (roughness) on the molecular scale. The reflections that are resolved and narrow indicate a well-crystallized material. The pattern is similar to previous result and the simulated one shown in literature[97] confirming the structure of MIL-96 sample.
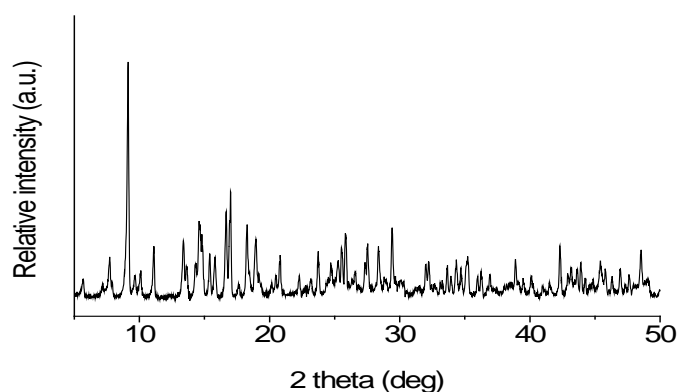
Figure 44. XRD pattern of MIL-96.

The TEM images of MIL-96 in different magnifications are shown in Figure 45. The nanoparticles have a size of *ca.* 10–15 nm and are nearly cube shaped.

(a)   (b)
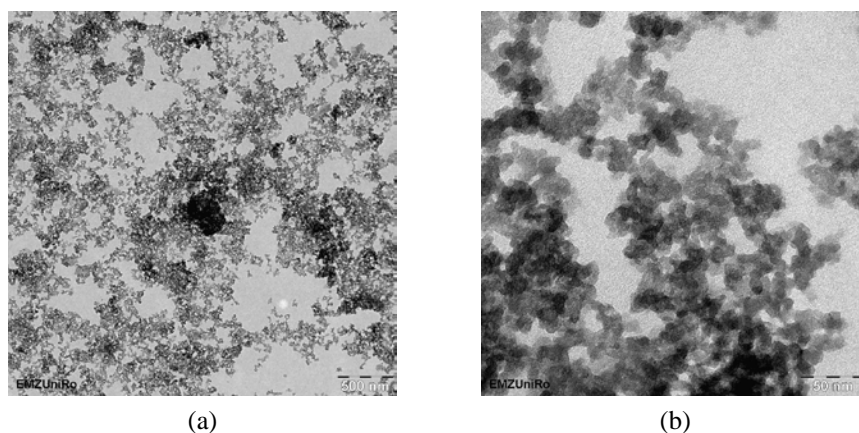
Figure 45. TEM images of MIL-96.

Summary - Material and Characterization

- MOFs of different structures and pore sizes have been successfully synthesized, i.e., the small pore-sized MOFs as MIL-77 and MIL-96, the medium pore-sized MOFs as IRMOF-3 and MOF-5, the large pore-sized MOF as MIL-101, and the extra-large mesostructured MOFs as MesoMIL-1 and MesoMIL-2.

- XRD, FTIR, and nitrogen sorption measurements confirm the structure type, the crystallinity as well as the porosity of the synthesized MOFs. SEM and TEM investigations show that crystalline nanoparticles have been obtained with MOF-5, MIL-101, and MIL-96. In cases of MIL-77, IRMOF-3, MesoMIL-1, and MesoMIL-2, bigger particles of micrometer size have been achieved.

- However, the apparent big microparticle of IRMOF-3 consists of smaller agglomerated micro-nano particles forming the hierarchically structured nano–meso–macro pore system.

- The highly dispersed rhodium in a single site manner in the MOF frameworks (single site catalysts) using low rhodium loadings (*ca.* 0.1 wt%) has been prepared. In case of Rh@MIL-101, for instance, only *ca.* 1.2% of trimeric chromium sites are occupied by rhodium.

- The rhodium is not detected for all Rh@MOF samples by XPS investigation due to the low loading and also high dispersion. However, significant shifts of electron binding energies (to lower energies) of elements forming the MOF structure are

found. The shifts indicate a strong interaction between the MOF structure and the supported rhodium and indirectly give a proof of the high rhodium dispersion in the MOF framework. The severe shifts which are always observed with O_{1s} and metals (Zn_{2p} or Cr_{2p}) point the location of rhodium at the metal oxide clusters of the MOF framework.

- In SASX investigations, nano rhodium particles are not detected in Rh@MOFs even with higher rhodium loading samples (e.g., an investigation of Rh@MIL-101 of up to 1 wt% of rhodium). This again strongly confirms that the hybrid MOF frameworks are good carriers to engineer single site catalysts. The textural porosities of used MOF supports is summarized in Table 8.

Table 8. Porosity and specific surface areas of the investigated MOFs. Pore and window diameters of MOFs from ref.[4,6,95,96,98,139]

MOFs	Free pore diameter (Å)	Free aperture for window (Å)	BET surface area ($m^2 g^{-1}$)	Pore volumes ($cm^3 g^{-1}$)
MIL-77	small	very small	170	-
MIL-96	8.8	2.5–3.5	530	-
IRMOF-3	10.15	< 8	2450	0.96
MOF-5	12	8	2337	1.00
MIL-101	29–34	12–14.7	4703	2.38
MesoMIL-1	200[**]	(12–14.7)[*]	1000	1.00
MesoMIL-2	700[**]	-	470	0.50

[*] MesoMIL-1 contains the MIL-101 structure
[**] from this study

3.2. Catalysis of Rh@MOFs

3.2.1. Rh@MOF-5

3.2.1.1. Reaction of single olefin component

The total conversions of different linear terminal *n*-alk-1-ene as *n*-hex-1-ene, *n*-oct-1-ene, *n*-dec-1-ene, and *n*-dodec-1-ene in the hydroformylation over Rh@MOF-5 are shown in Figure 46. The conversions proceed relatively fast with a nearly linear increase of the conversion with the reaction time. Apart from *n*-oct-1-ene, the conversions decrease with increasing chain lengths of the olefins as expected. The total conversions of *ca.* 99%, 90%, and 67% to aldehydes and internal olefins are achieved after 5 h of reaction with *n*-hex-1-ene, *n*-dec-1-ene, and *n*-dodec-1-ene, respectively (Figure 46). Interestingly, the conversion of *n*-oct-1-ene is much lower than that of the longer molecules as *n*-dec-1-ene and *n*-dodec-1-ene under same reaction conditions. The total conversion of *n*-oct-1-ene only reaches 16.7% after 3 h of reaction, which is markedly lower compared to 37.2% in case of the longer molecule *n*-dodec-1-ene and to 58.6% in case of *n*-dec-1-ene. The low conversion of *n*-oct-1-ene might due to its restricted access to the rhodium active sites. The more linear shaped long-tailed *n*-oct-1-ene molecule with a chain length of *ca.* 10 Å has difficulty to arrange its double bond at the active site, which is proposed to be located at the corner in the cages of MOF-5.
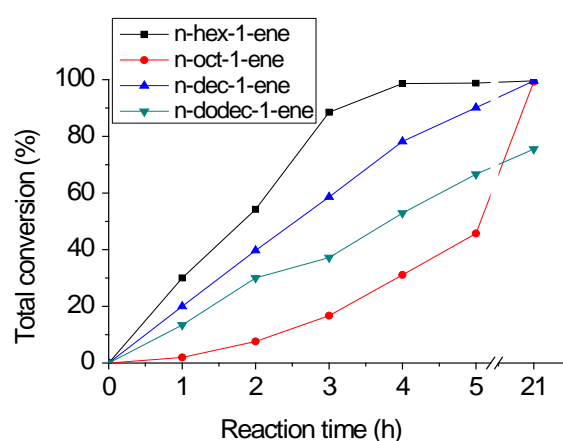
Figure 46. Total conversion of *n*-alk-1-ene in hydroformylation catalyzed by Rh@MOF-5. Reaction conditions: olefin/Rh = 100000/1, *T* = 100 $^{\circ}$C, *p* = 50 bar.

The aldehyde selectivities of *n*-alk-1-enes in the hydroformylation are presented in Figure 47. They are of *ca.* 30–35% and slightly change during 1–5 h of reactions. The selectivity of *n*-hex-1-ene is higher compared to the others beyond 3–4 h and reaches a very high value after 21 h of reaction. The increases of aldehyde selectivity during 5–21 h of reactions are due to the conversions of internal alkenes present in the reaction solutions to the corresponding *i*-aldehydes. Despite *n*-hex-1-ene, achieved increase in the aldehyde selectivity to *ca.* 50% by the conversion of internal alkenes even after prolonged time reaction is comparatively low. This is an additional indication for the presence steric hindrances in confined spaces of the pores/cages confirming size and shape selective properties of MOF-5.
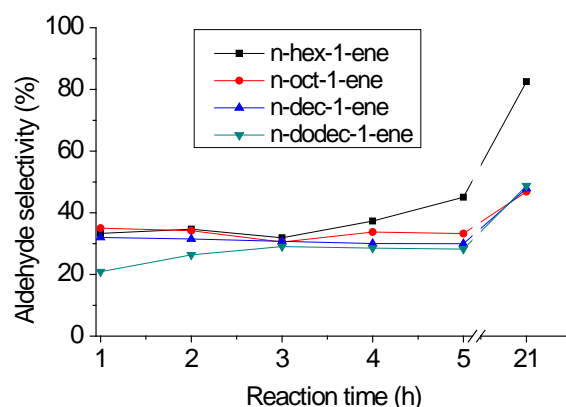
Figure 47. Selectivity to aldehydes in hydroformylation of *n*-alk-1-ene catalyzed by Rh@MOF-5. Reaction conditions: olefin/Rh = 100000/1, $T = 100\ ^{o}C$, $p = 50$ bar.

The yields of aldehydes in dependence on the reaction time obtained with *n*-alk-1-enes over Rh@MOF-5 are shown in Figure 48. The yields enhance correspondingly with the increases of the total conversions shown in Figure 46. After 5 h of reactions, *ca.* 45%, 15%, 27%, and 19% of *n*-hex-1-ene, *n*-oct-1-ene, *n*-dec-1-ene, and *n*-dodec-1-ene, respectively, are converted to aldehydes. The increase of the yield after prolonged reaction time is mainly due to the conversion of the less reactive internal alkenes. In the case of *n*-hex-1-ene, however, maximum conversion is already achieved after *ca.* 4 h of reaction (Figure 46), thus, the enhancement of aldehydes beyond this reaction time is due to the conversion of the internal hexenes alone. It is also the reason why the aldehyde selectivity starts to increase at *ca.* 4 h of reaction for *n*-hex-1-ene and at *ca.* 5 h of reactions for the other components (Figure 47).
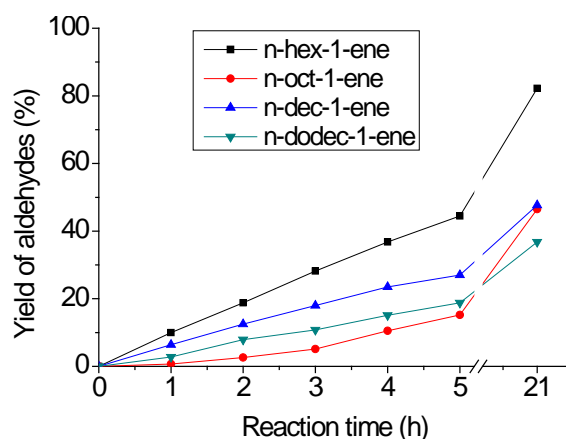
Figure 48. Yield of aldehydes in hydroformylation of *n*-alk-1-ene catalyzed by Rh@MOF-5. Reaction conditions: olefin/Rh = 100000/1, T = 100 $^{\circ}$C, p= 50 bar.

The *n/i*-aldehyde ratios are shown in Figure 49. Except for *n*-oct-1-ene at 1 h and *n*-hex-1-ene after 3 h of reactions, the ratios are very high and vary in a range of 2.8–3 during 1–5 h of reaction. In the case of *n*-oct-1-ene, the yield of aldehydes at 1 h of reaction is definitely small, of only 0.7%; hence, this low ratio can be an error. Due to the conversions of the internal alkenes to the corresponding *i*-aldehydes as stated above, the ratios are decreased to lower values of *ca.* 1–1.5 after prolonged reaction times (Figure 49). In case of *n*-hex-1-ene, the maximal total conversion is already achieved after a shorter reaction time, and then the formed internal alkenes are further converted to corresponding *i*-aldehydes. Therefore, its *n/i*-aldehyde ratio reduces earlier and faster compared to the others
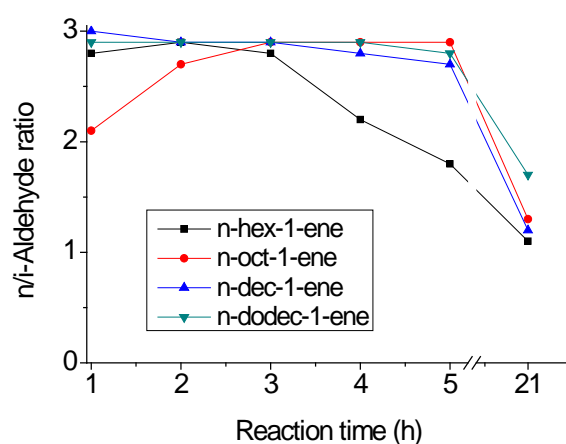
Figure 49. *n/i*-Aldehyde ratio in hydroformylation of *n*-alk-1-ene catalyzed by Rh@MOF-5. Reaction conditions: olefin/Rh = 100000/1, T = 100 $^{\circ}$C, p= 50 bar.

Different sized olefins, namely cyclohexene, cyclooctene, and different branched olefins such as 3,3-dimethylbut-1-ene (DMB), 4,4-dimethylpent-1-ene (DMP), and

50

2,4,4-trimethylpent-1-ene (TMP) were used as test molecules in order to study the molecular sieve effect (size exclusion) of the MOF-5 framework. Indeed, the conversions of the large cycloolefins and the bulky TMB are very low in the first hours of reaction revealed by yield of aldehydes vs. reaction time plots shown in Figure 50. This provides evidence of active Rh species located inside the MOF crystals. The prevention of cyclohexene conversion might be due to limited access of cyclohexene to the active site in the cage or the hindered diffusivity of the formed aldehyde because cyclohexene is known to be small enough to pass the window of the MOF-5 channels.[140]

The conversions of DMB and DMP to aldehydes are somewhat higher compared to those of *n*-dodec-1-ene, *n*-dec-1-ene, and *n*-oct-1-ene (Figure 48) although the linear internal alkenes are more reactive than the branched terminal alkene (Scheme 4). It seems that the bulky trimethyl head group decreases the access to pores. But the tail with the C═C group may stick into the outer pores. Or these (shorter) molecules can more effectively attach the double bond to the active sites in the cages. Therefore, a remarkable increase of the aldehyde yield is observed after 21h of reaction.
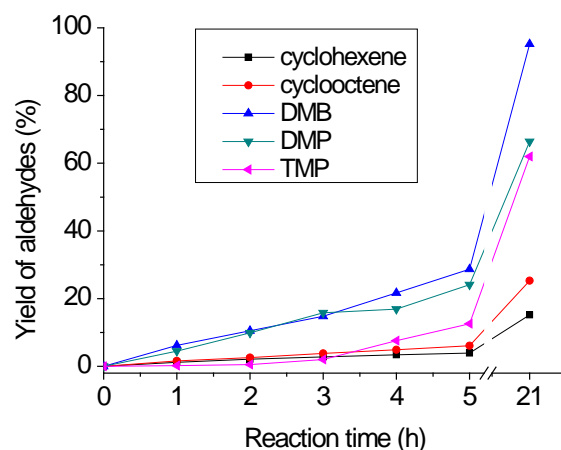
Figure 50. Yield of aldehydes in hydroformylation of cyclo and branched olefins catalyzed by Rh@MOF-5. Reaction conditions: olefin/Rh = 100000/1, T = 100 ^{o}C, p= 50 bar.

3.2.1.2. Reaction of mixture of olefins

In practice, also mixtures of olefin are used as feedstock for the hydroformylation. Therefore, it is of interest to study the behavior of olefin mixture. Here two mixtures containing three olefin components were utilized to investigate a possible interference. In the experiments, the molar olefin/catalyst ratio (100000/1 based on

rhodium), the solvent, and other the reaction conditions are similar to the single component experiments. Hence, the molar concentration of each olefin in the starting reaction solution is only one-third compared to the single component reaction; the other two olefins share the two-thirds left.

- *Mixture of n-hex-1-ene, n-oct-1-ene and cyclohexene*

The results of the hydroformylation tests are shown in Figure 51–54. In case of the *n*-hex-1-ene, *n*-oct-1-ene, and cyclohexene mixture, the behavior of *n*-hex-1-ene and *n*-oct-1-ene are quite similar to each other in terms of total conversion, aldehyde selectivity, and yield of aldehydes. Similar results have been observed with *n*-dec-1-ene and *n*-dode-1-cene, respectively, in another experiment. This behavior is different from that observed with single components where the conversion of *n*-hex-1-ene is higher and that of *n*-oct-1-ene is distinctly lower (Figure 46). Their total conversions continuously increase during 1–5 h of reaction and already reach over 95% after 5 h (Figure 51). While the aldehyde selectivities are constant during 1–5 h (Figure 52), the yields of aldehydes develop in line with the conversions and arrive at *ca.* 32% (Figure 53). The further increases of the aldehydes for a prolonged reaction time (21 h) are due to the conversions of the internal hexenes and octenes existed in the reaction solutions to the corresponding *i*-aldehydes. The enhancements of the aldehyde selectivities during 5–21 h, shown Figure 52, clearly explain the increases of the aldehyde yields.
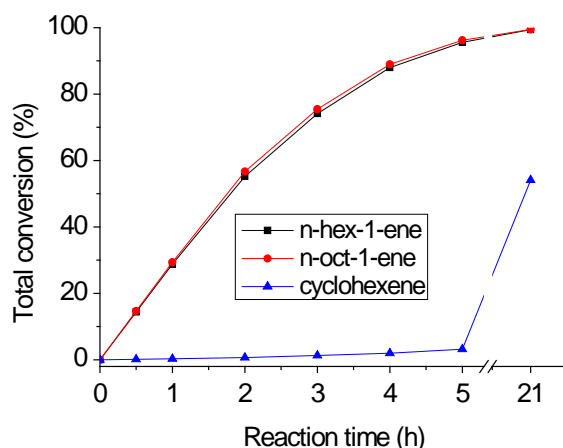
Figure 51. Total conversion in hydroformylation of the mixture of *n*-hex-1-ene, *n*-oct-1-ene, and cyclohexene catalyzed by Rh@MOF-5. Reaction conditions: olefin/Rh = 100000/1, T = 100 $^{\circ}$C, p= 50 bar.
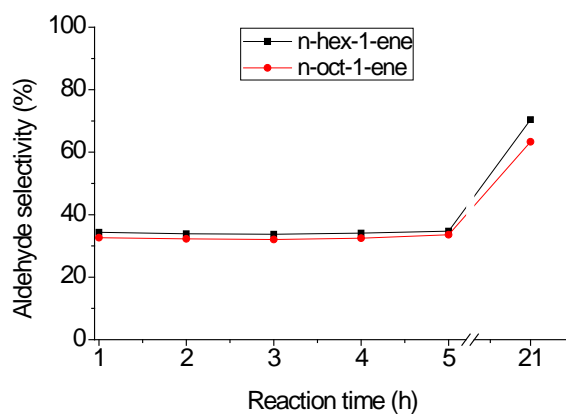
Figure 52. Selectivity to aldehydes in hydroformylation of the mixture of *n*-hex-1-ene, *n*-oct-1-ene, and cyclohexene catalyzed by Rh@MOF-5. Reaction conditions: olefin/Rh = 100000/1, *T* =100 °C, *p*= 50 bar.
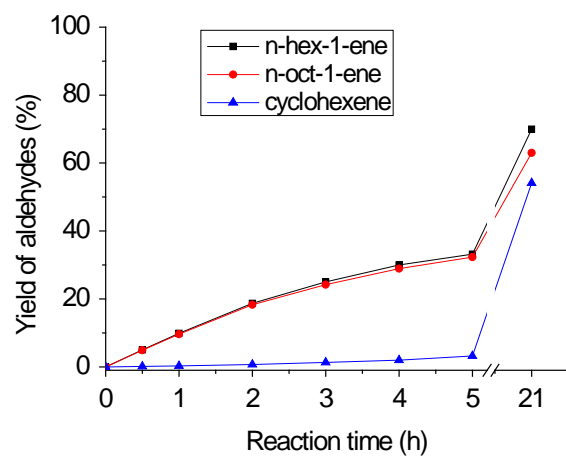
Figure 53. Yield of aldehydes in hydroformylation of the mixture of *n*-hex-1-ene, *n*-oct-1-ene, and cyclohexene catalyzed by Rh@MOF-5. Reaction conditions: olefin/Rh = 100000/1, *T* =100 °C, *p*= 50 bar.
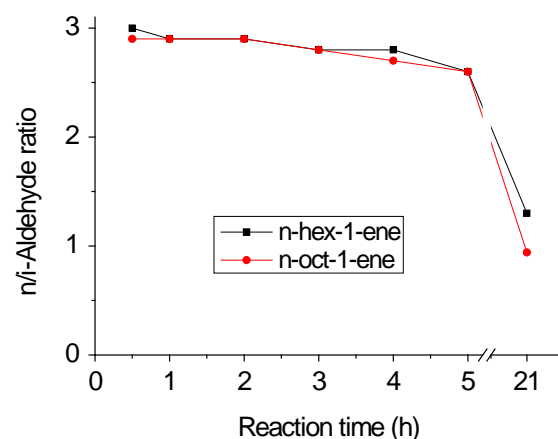
Figure 54. *n/i*-Aldehyde ratio in hydroformylation of the mixture of *n*-hex-1-ene, *n*-oct-1-ene, and cyclohexene catalyzed by Rh@MOF-5. Reaction conditions: olefin/Rh = 100000/1, *T* =100 °C, *p*= 50 bar.

Cyclohexene is nearly excluded from the reaction. The conversion of only 1.3% is achieved after 3 h. This is lower than the conversion observed in the single component reaction of 2.8% (Figure 50). The n/i-aldehyde ratios obtained with the mixture reaction are still high with values of *ca.* 2.8 after 5 h (Figure 54) as found with the single component reaction (Figure 49). With prolonged reaction time, the ratios are distinctly decreased to 1.3 and 0.94 for n-hex-1-ene and n-oct-1-ene, respectively, due to the conversions of the internal olefins (Figure 54). Interestingly, the conversion of cyclohexene to aldehyde is significantly accelerated after the prolonged reaction time and reaches *ca.* 55% compared to only *ca.* 15% in case of single component reaction (Figure 50).

- ***Mixture of n-oct-1-ene, cyclooctene and TMP***

The results of the hydroformylation of the mixture of n-oct-1-ene, cyclooctene, and TMP are presented in Figure 55 and Figure 56.
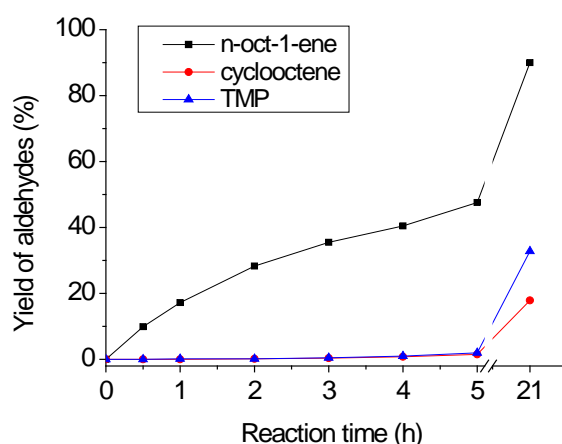
Figure 55. Yield of aldehydes in hydroformylation of the mixture of n-oct-1-ene, cyclooctene, and TMP catalyzed by Rh@MOF-5. Reaction conditions: olefin/Rh = 100000/1, $T = 100\ ^{\circ}$C, p= 50 bar.

As shown, the yield of aldehyde for n-oct-1-ene is markedly higher than that for cyclooctene and TMP. In comparison with the single component reactions, the yield for n-oct-1-ene in this case is higher (Figure 48 and Figure 55) due to the increased conversion of the formed internal octenes as indicated by the decrease of the n/i-aldehyde ratio after 2h (Figure 56). In contrast, the aldehyde yields for both cyclooctene and TMP are significantly lower (Figure 50 and Figure 55). For example, after 3 h of reaction, the yields of aldehydes in the single component tests are 5.1%,

3.8%, and 2.0% for *n*-oct-1-ene, cyclooctene, and TMP, respectively. But they achieve 35.5%, 0.4%, and 0.5% for *n*-oct-1-ene, cyclooctene, and TMP, correspondingly, after the same reaction time with the mixture. This finding is in line with the previous findings that the most reactive olefin is firstly converted.
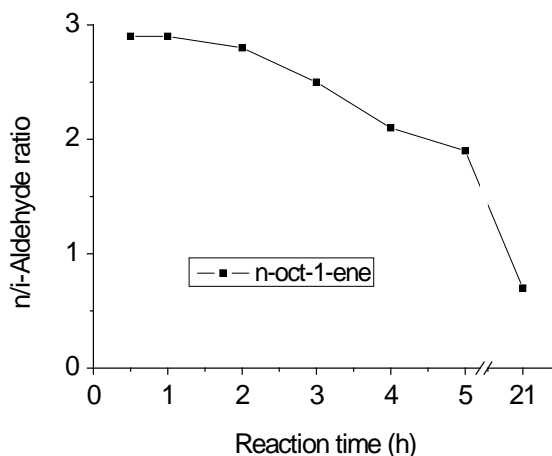
Figure 56. *n/i*-Aldehyde ratio in hydroformylation of the mixture of *n*-oct-1-ene, cyclooctene, and TMP catalyzed by Rh@MOF-5. Reaction conditions: olefin/Rh = 100000/1, T = 100 $^\circ$C, p= 50 bar.

In summary, the hydroformylation behavior of the used olefin mixtures is different from that of the single components (compare to chapter 3.2.1.1). The more reactive *n*-alk-1-enes are preferentially converted compared to less reactive olefins like cyclohexene or TMP. Noticeably, the hydroformylation behavior of the different sized *n*-alk-1-enes becomes equal regarding total conversion and aldehyde selectivity. Additionally, the high conversion of the internal alkenes to *i*-aldehydes is found after a prolonged reaction time. Less reactive components are converted last.

3.2.2. Rh@IRMOF-3

The total conversions of the different *n*-alk-1-enes in the hydroformylation over Rh@IRMOF-3 are shown in Figure 57. As revealed, the reaction proceeds very fast in the first 1–2 h of reaction, with exception of the *n*-oct-1-ene. The total conversion nearly linearly increases with the reaction time. After 1 h, the conversions achieved with *n*-hex-1-ene, *n*-dec-1-ene, and *n*-dodec-1-ene are *ca.* 30–45%. In contrast, *n*-oct-1-ene shows a distinct lower conversion of only 5%. After 3 h, more than 90% of conversion is obtained (Figure 57). The low activity of the *n*-oct-1-ene in the first 2 h of reaction is explained by limited access to the active Rh sites. Although the Rh is

located in the open pore structure, the more linear shaped long-tailed *n*-oct-1-ene molecule, with a chain length of *ca.* 10 Å, is difficult to arrange with its double bond at the active site in the confined space of the pore cages. A similar effect is found with rhodium supported MOF-5 as stated in chapter 3.2.1.1. Rh@IRMOF-3 shows higher activity compared to Rh@MOF-5 even though the pore diameter and pore opening/window of IRMOF-3 are smaller due to the –NH$_2$ group attached to the benzene ring of the linker. This finding can be explained by the presence of a hierarchically structured micro–meso–macro pore system in between the nanoparticles of IRMOF-3 (compare to chapter 3.1.2) improving mass transfer and access of olefins to the active sites. This will be further discussed below (chapter 3.3: Structure-Catalytic Property-Relationships).
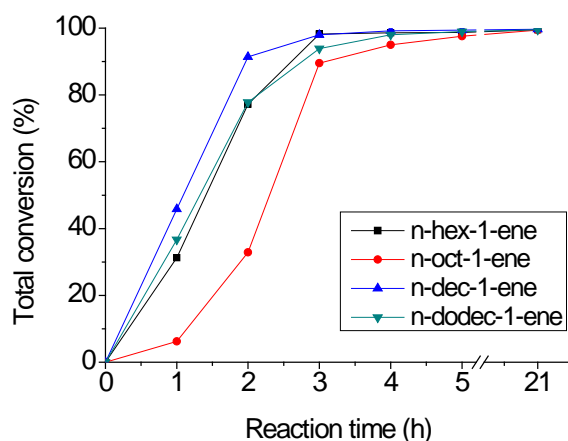
Figure 57. Total conversion of *n*-alk-1-ene in hydroformylation catalyzed by Rh@IRMOF-3. Reaction conditions: olefin/Rh = 100000/1, *T* = 100 $^{\circ}$C, *p*= 50 bar.
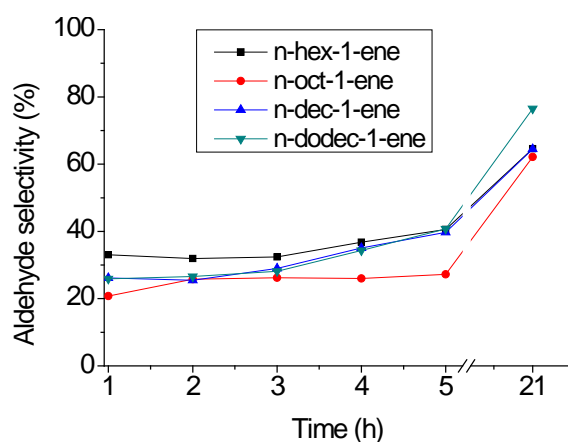

Figure 58. Selectivity to aldehydes in hydroformylation of *n*-alk-1-ene catalyzed by Rh@IRMOF-3. Reaction conditions: olefin/Rh = 100000/1, *T* = 100 $^{\circ}$C, *p*= 50 bar.

The selectivities to aldehydes are nearly unchanged during the first 3 h of reaction and vary between 26% and 32% depending on the substrate (Figure 58). They are lowest for the *n*-oct-1-ene. The selectivities further increase after prolonged reaction time due to the hydroformylation of internal alkenes. The corresponding aldehyde yields are shown in Figure 59. They increase quickly in the first 3 h of reaction and are in line with the course of conversion as well as aldehyde selectivity.
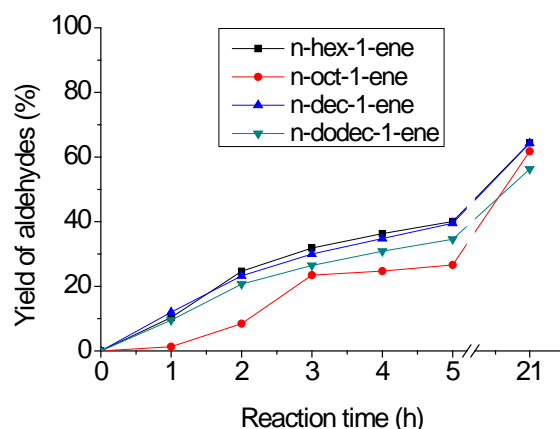
Figure 59. Yield of aldehydes in hydroformylation of *n*-alk-1-ene catalyzed by Rh@IRMOF-3. Reaction conditions: olefin/Rh = 100000/1, T = 100 ^{o}C, p= 50 bar.

The *n/i*-aldehyde ratio varies between *ca.* 2.7 and 3 in the first 2 h of reaction (Figure 60) and decreases thereafter. The total conversion of terminal alkenes has been nearly reached maximum value at this stage. Only internal alkenes remain in the reaction solution. Their hydroformylation leads to a decrease of the *n/i*-aldehyde ratio after prolonged reaction times. In the case of *n*-oct-1-ene, unreacted *n*-oct-1-ene is still present in the reaction mixture maintaining its higher *n/i*-aldehyde ratio as shown in Figure 60.
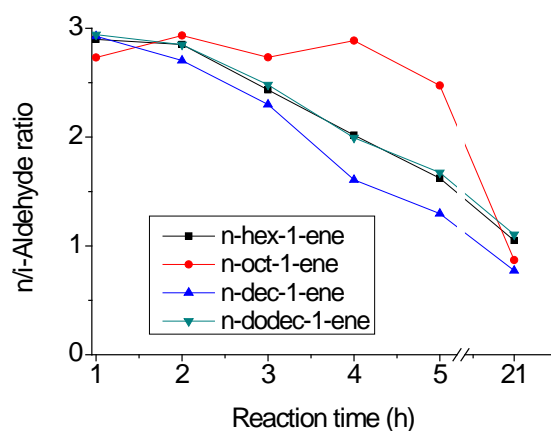
Figure 60. *n/i*-Aldehyde ratio in hydroformylation of *n*-alk-1-ene catalyzed by Rh@IRMOF-3. Reaction conditions: olefin/Rh = 100000/1, T = 100 ^{o}C, p= 50 bar.

In the cases of the more bulky cyclohexene and the double bond shielded TMP, the conversion to aldehydes is lower than that of terminal *n*-olefins and reaches *ca.* 20% after 2 h. In contrast, the steric demanding, less flexible hexa-1,5-diene is not converted. The approach of the C=C double bond to the active rhodium sites is prohibited (Figure 61). The IRMOF-3 catalyst has been reused after filtration without further work up. It is found that the catalytic activity decreases. However, the selectivity behavior, characterized by the *n/i*-aldehyde ratio, remains unchanged.

Figure 61. Yield of aldehydes in hydroformylation of bulky or stiff olefins catalyzed by Rh@IRMOF-3. Reaction conditions: olefin/Rh = 100000/1, T = 100 °C, p = 50 bar.

In summary, similar to Rh@MOF-5, Rh@IRMOF-3 is very active and selective in the hydroformylation of olefins. In comparison with the aforesaid material, this catalyst is more active due to the hierarchically arranged small primary MOF nanocrystals and secondary microparticles forming a combined micro–meso–macro pore system allowing easy access to active sites.

3.2.3. Rh@MIL-101

Different from MOF-5 and IRMOF-3, the metal-organic framework MIL-101 contains mesopores having diameters of 29 Å and 34 Å accessible via *ca.* 12–14.5 Å sized pore openings. Therefore, the large *n*-hexadec-1-ene molecule was included in the investigation of the hydroformylation.

The dependence of the total conversion on the reaction time of different *n*-alk-1-enes such as *n*-hex-1-ene, *n*-oct-1-ene, *n*-dec-1-ene, *n*-dodec-1-ene, and *n*-hexadec-1-ene over Rh@MIL-101 is shown in Figure 62. With the exception of *n*-hexadec-1-ene, the

reactions proceed fast. Total conversions of *ca.* 35–55% are already achieved after 1 h of reaction depending on the starting *n*-alk-1-enes. *Ca.* 90% of conversion is achieved after 3 h. The high activity of the catalyst despite the low Rh loading points to the presence of highly dispersed single active site species. The formation of uniform and small Rh species is facilitated by a defined support with structural uniformity of metal oxide surfaces combined with well separated inorganic and organic components as present in MOF and the use of Rh(acac) precursor. Thereby, the acetylacetonato (acac) ligand of the metal complex is replaced by oxygen of the metal sites.[109,110] The reaction of the present OH groups located at chromium site may assist the replacement of the acac ligand from the Rh precursor and the formation of metal–O bonds as shown with supported zeolites.[110]
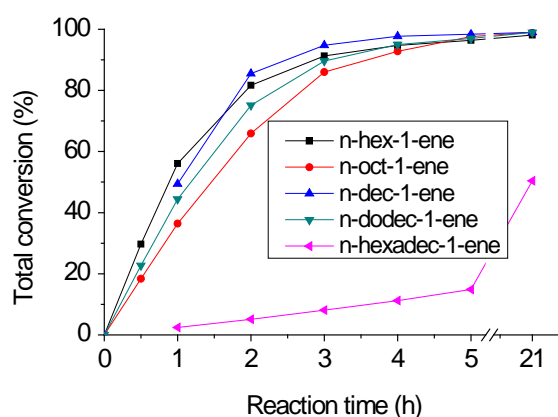
Figure 62. Total conversion of *n*-alk-1-ene in hydroformylation catalyzed by Rh@MIL-101. Reaction conditions: olefin/Rh = 70000/1, T = 100 $^{\circ}$C, and p= 50 bar.

With exception of *n*-oct-1-ene, the conversions systematically decrease with growing chain lengths of the *n*-alk-1-ene in the order: *n*-hex-1-ene > *n*-dec-1-ene > *n*-dodec-1-ene > *n*-oct-1-ene ≫ *n*-hexadec-1-ene, after 1 h of reaction. The conversion of *n*-oct-1-ene is lower than that of the larger molecules like *n*-dec-1-ene and *n*-dodec-1-ene. Very low conversion is observed with the bulky *n*-hexadec-1-ene compared to *n*-dodec-1-ene. The conversion of *n*-hexadec-1-ene slowly increases with prolonged time of reaction. This slow conversion points to a mass transfer hindrance of this large molecule due to the limited window sizes of 12 Å and 14.5 Å of the pores in the MIL-101 structure and/or limited access to the active sites.

Figure 63 shows the selectivity to aldehydes in dependence of the reaction time observed with *n*-alk-1-enes. The selectivity is only *ca.* 20% in case of *n*-hex-1-ene,

whereas it reaches nearly 30% in case of the longer chain molecules such as *n*-oct-1-ene, *n*-dec-1-ene, and *n*-dodec-1-ene. That means, *ca.* 80% or 70% of reaction products converted belong to double bond isomerized internal alkenes. Rh itself favors this isomerization. The blank experiments with *n*-hex-1-ene and *n*-oct-1-ene show that the parent MIL-101 (without rhodium) does not catalyze the double bond isomerization of terminal alkenes to internal alkenes or the hydroformylation of alkenes to aldehydes even after 21 h of reaction. Interestingly, the aldehyde selectivity is nearly unchanged during the course of reaction, even after 21 h (Figure 63). This finding reveals that double bond shifted internal alkenes, accounting for 70–80% of the reaction mixtures, are nearly not converted to the corresponding aldehydes over Rh@MIL-101. This result is different from the hydroformylation performance observed with the Rh@IRMOF-3 or Rh@MOF-5. In the latter, a large amount of *i*-aldehydes is formed from internal alkenes present in the reaction mixture.
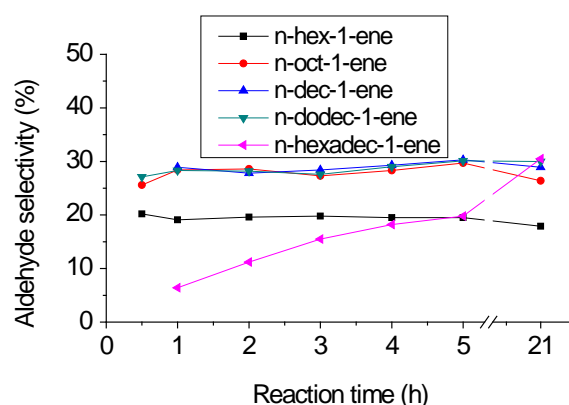
Figure 63. Selectivity to aldehydes in hydroformylation of *n*-alk-1-ene catalyzed by Rh@MIL-101. Reaction conditions: olefin/Rh = 70000/1, T = 100 ^{o}C, and p= 50 bar.
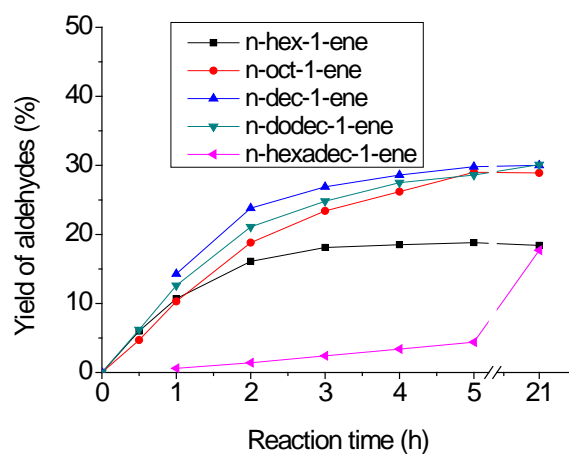
Figure 64. Yield of aldehydes in hydroformylation of *n*-alk-1-enecatalyzed by Rh@MIL-101. Reaction conditions: olefin/Rh = 70000/1, T = 100 ^{o}C, and p= 50 bar.

The selectivity behavior is reflected in the yield of aldehydes (Figure 64). During the first 3 h to 4 h, the yields increase in parallel with the conversion. However, the yields are not further increased after achieving nearly complete conversion (> 90%) of the n-alk-1-enes. Even after prolonging the reaction time to 21 h, the yields are only slightly changed with exception of n-hexadec-1-ene. As mentioned above, the mass transfer of this large molecule is decreased and the access to the active sites is hindered due to the shielding of the C=C double bond by the surrounding of large alkyl chain. Therefore, the total conversion and the initial aldehyde selectivity are comparatively low and slowly increased with reaction time. The finding that the internal alkenes are hardly converted to the corresponding i-aldehydes points to a hindered access of these molecules to the active rhodium sites of the MOF MIL-101. This is apparently surprising because the MIL-101 framework is highly porous and contains large cages (small mesopores). But the result can be explained by a preferred location of the active rhodium at the ST units. These units are microporous[57] limiting approach and access of the olefins to the Rh active sites. As known from related crystalline microporous zeolite structures, small windows and cages are preferred sites for metal ions.[141] They are energetically favored due to short interaction distances and the enhanced number of surrounding neighbored atoms. Therefore, it is plausible to assume that the catalytic active and highly dispersed rhodium species are located at these sites in the supertetrahedra. These window sites are less accessible that explains the hindered conversion of internal alkenes R_1–CH=CH–R_2 to aldehydes, where the double bond of the molecule and shielded by space demanding alkyl groups on both of the two sides. Therefore, the approach of C=C group to the active site is hindered. In contrast, in n-alk-1-ene, the double bond is located at the head of the molecule R–CH=CH$_2$ and can be exposed to the active sites (Figure 65).

Interestingly, the n-oct-1-ene has been found to be less active than the larger n-dec-1-ene and n-dodec-1-ene (Figure 62). This finding is also observed in the hydroformylation of n-alk-1-enes over Rh@MOF-5 and Rh@IRMOF-3 as shown above.[142] With MOF-5 and IRMOF-3 supports, less large porous (microporous) metal-organic frameworks compared to MIL-101, the activity differences are more pronounced (Figure 46 and Figure 59). A possible reason could be that the relative long and straight n-oct-1-ene (*ca.* 10 Å in length) is difficult to arrange at the active

sites due to the curvature of the pore walls of MIL-101 (Figure 65) and the limited free space of pores in MOF-5 and IRMOF-3 (*ca.* 12 Å).

Figure 65. Schematic representation of large cages and supertetrahedral (ST) side pockets of MIL-101. Proposed location of dispersed Rh active sites on less accessible position at the microporous ST unit forming the walls of the large cages of MIL-101 leading to limited access of converted internal alkenes compared to the starting terminal *n*-alk-1-enes.
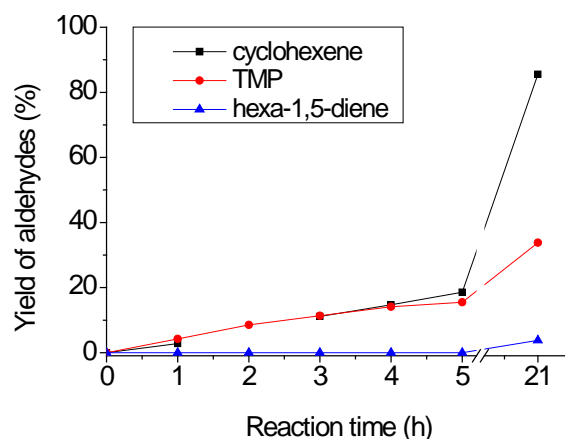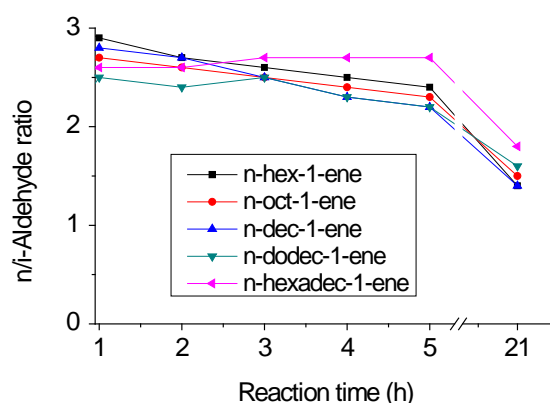

Figure 66. *n/i*-Aldehyde ratio in hydroformylation of *n*-alk-1-ene catalyzed by Rh@MIL-101. Reaction conditions: olefin/Rh = 70000/1, $T = 100\ ^{\circ}$C, and $p = 50$ bar.

The *n/i*-aldehyde ratios are presented in Figure 66. They are *ca.* 2.5–3 during 1–3 h of reaction. The MIL-101 framework shows improved *n*-aldehyde selectivity. The *n/i*-aldehyde ratios decrease to 1.5–1.8 after 21 h although the yields of aldehydes are only slightly changed. The decrease of the *n/i*-aldehyde ratio is due to the aldol condensation side reaction preferentially of *n*-aldehydes after long time of reaction yielding the corresponding unsaturated aldehydes. GS/MS analysis of reaction solutions after 5 h and 21 h of *n*-hex-1-ene hydroformylation shows favored aldol condensation of *n*-heptanal (Table 9). The loss of aldehydes by aldol condensation is in part compensated by the formation of aldehydes from remaining *n*- and internal alkenes in the reaction solution (Table 9). Therefore, the yield of aldehyde is slightly

decreased after the prolonged reaction time (Figure 64). The aldol condensation side reaction could be accelerated by the acid sites of the MIL-101, which amount to *ca.* 1 mmol g^{-1} and are created the coordinative unsaturated chromium metal sites in the MOF structure.[57] As a result, the *n*/*i*-aldehyde ratio decreases after the long reaction time.

Table 9. Detail of product mixture in hydroformylation of *n*-hex-1-ene after 5 h and 21 h of reaction.

Substrate/product in reaction product (%)	Reaction time	
	5 h	**21 h**
***n*-Hex-1-ene**	3.6	1.8
Internal hexenes	75.9	74.5
***n*-Aldehyde**	13.5	10.1
***i*-Aldehydes**	5.9	6.8
Aldol condensation products	0.6	4.6*
Sum of aldehydes	19.4	16.9

*Aldol condensation products containing 83% of $H_3C-(CH_2)_5-CH=C(CHO)-(CH_2)_4-CH_3$.
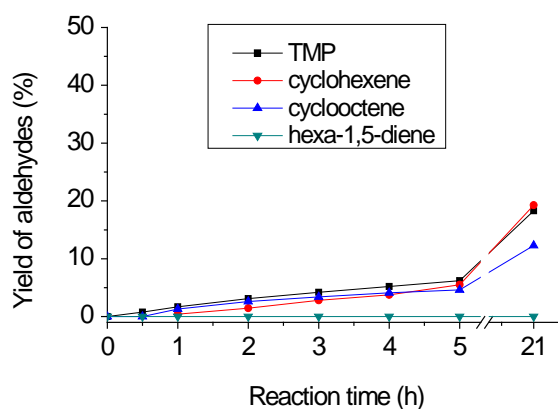
Figure 67. Yield of aldehydes in hydroformylation of bulky or less flexible olefin catalyzed by Rh@MIL-101. Reaction conditions: olefin/Rh = 70000/1, T = 100 °C, and p= 50 bar.

The steric constrains giving rise to limited access to rhodium sites in the MIL-101 framework have been further studied by using different bulky alkenes such as TMP, cyclohexene, cyclooctene, and the less flexible hexa-1,5-diene. The yields of aldehydes in these hydroformylation reactions are shown in Figure 67. The TMP, cyclohexene, and cyclooctene are slowly converted to aldehydes. However, hexa-1,5-

diene is not converted although one C=C double bond is located in "head" position like in *n*-hex-1-ene and the molecules are of similar size. The hexadiene is a very stiff bar-shaped molecule and the diene can act as a poison.[143]

In conclusion, despite low Rh loading, the Rh@MIL-101 catalyst is highly active which is assigned to the high dispersion and formation single site Rh species in the organic-inorganic hybrid framework. The catalyst behaves selective. The *n*/*i*-aldehyde ratios achieve values of up to 3. The bulky olefins are slowly converted, even though MIL-101 is a highly porous support containing mesoporous cages. Especially, the internal alkenes are hardly converted to the corresponding aldehydes. The observed selectivity is ascribed to the location of catalytic active rhodium species at internal framework sites of the microporous supertetrahedra, which renders approach of molecules to the active sites more difficult resulting in size and shape selectivity.

3.2.4. Rh@mesoMILs

3.2.4.1. Rh@MesoMIL-1

The total conversions of *n*-hex-1-ene, *n*-oct-1-ene, and *n*-dodec-1-ene in the hydroformylation over Rh@MesoMIL-1 are shown in Figure 68. The reactions are very speedy. The conversions already achieve *ca.* 40% to 60% after 1 h of reaction depending on the substrates. After 3–4 h, nearly all *n*-alk-1-enes are converted to aldehydes and internal alkenes. In comparison with Rh@MIL-101, Rh@MesoMIL-1 is somewhat more active indicating an improved mass transfer.
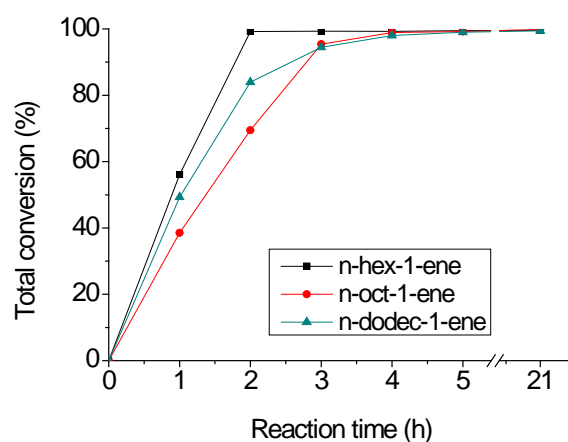

Figure 68. Total conversion of *n*-alk-1-ene in hydroformylation catalyzed by Rh@MesoMIL-1. Reaction conditions: olefin/Rh = 100000/1, *T* = 100 °C, and *p*= 50 bar.

Again, the conversion of *n*-oct-1-ene is still lower than that of the larger *n*-dodec-1-ene. Addionally, the conversion of cyclohexene is still low as observed with Rh@MIL-101 (Table 10). It is, therefore, concluded that the access to the active sites at the ST unit is still limited in the MesoMIL-1 framework.

Table 10. Hydroformylation of cyclohexene catalyzed by Rh@MesoMIL-1. Reaction conditions: olefin/Rh = 100000/1, T = 100 ^{o}C, p = 50 bar.

Reaction time (h)	Total conversion/Yield of aldehyde of cyclohexene (%)	
	Rh@MesoMIL-1	**Rh@MIL-101**
1	-	0.4
3	-	2.8
5	6.8	5.5
21	14.0	19.3

However, the selectivity and yield to aldehyde over Rh@MesoMIL-1 are totally different from those of Rh@MIL-101 (Figure 69 and Figure 70). The yields of aldehydes continuously increase during the course of reaction and reach high values after 3–4 h of reaction (Figure 70) due to the conversion of internal alkenes. Probably, the cutting of large cages by the formation of mesopores reduces the curvature effect facilitating access of the internal alkenes to the active sites. It is totally different from Rh@MIL-101 where the Rh sites are supposed to be situated in the microporous ST units and the access of the internal alkenes is hindered by the curvature of the pore walls of the large cages. These findings are in agreement with the nitrogen adsorption results, which indicate that a part of the MIL-101 structure is maintained in the MesoMIL-1 framework (the uptake curve between p/p_0 = 0–0.25).
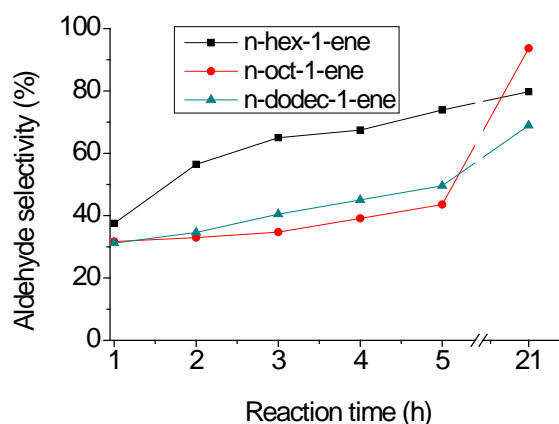
Figure 69. Selectivity to aldehydes in hydroformylation of *n*-alk-1-ene catalyzed by Rh@MesoMIL-1. Reaction conditions: olefin/Rh = 100000/1, T = 100 ^{o}C, and p = 50 bar.
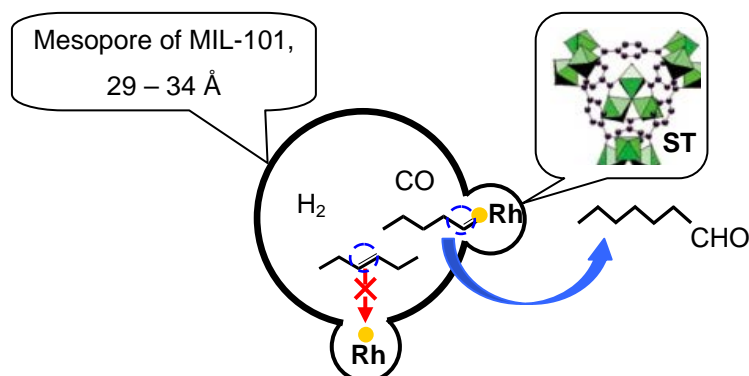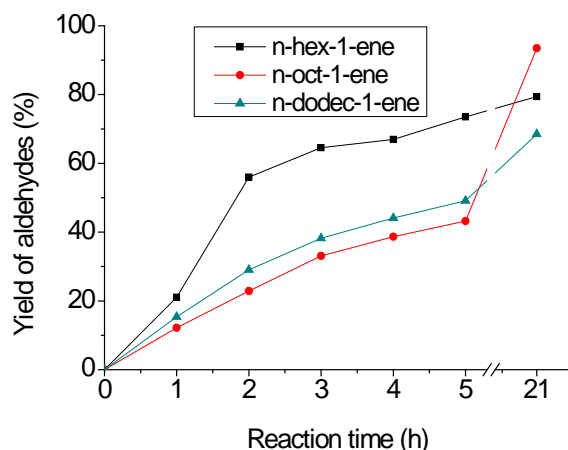
Figure 70. Yield of aldehydes in hydroformylation of *n*-alk-1-ene catalyzed by Rh@MesoMIL-1. Reaction conditions: olefin/Rh = 100000/1, T = 100 °C, and p= 50 bar.

The *n/i*-aldehyde ratios in the hydroformylation of *n*-alk-1-ene over Rh@MesoMIL-1 are presented in Figure 71. They decrease during the courses of reactions. In case of *n*-hex-1-ene, the ratio is lower and drops earlier and faster compared to the others. This is due to its high reactivity and the early conversion of formed internal hexenes to aldehydes. The high *n/i*-aldehyde ratio observed with *n*-oct-1-ene is again due to its low conversion.
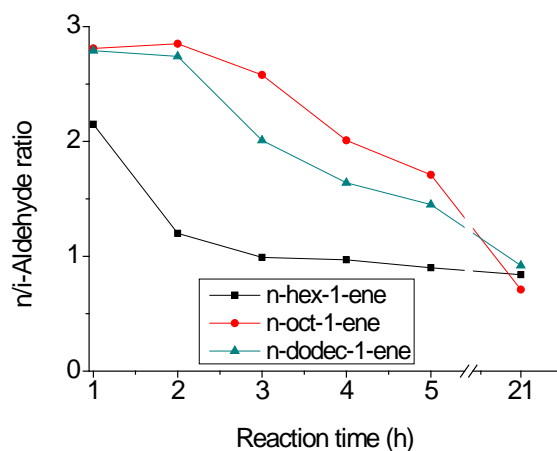
Figure 71. *n/i*-Aldehyde ratio in hydroformylation of *n*-alk-1-ene catalyzed by Rh@MesoMIL-1. Reaction conditions: olefin/Rh = 100000/1, T = 100 °C, and p= 50 bar.

In summary, Rh@MesoMIL-1 is very active in the hydroformylation of *n*-alk-1-enes. The incorporation of mesoporosity/mesostructure improves the mass transfer leading to the increased conversion compared to Rh@MIL-101. The partial cutting of large pore cages reduces the curvature effect, which renders the access to the active sites more difficult. As a result, the conversion of internal alkenes is boosted and the *n/i*-aldehyde ratio is decreased. The structure of MIL-101 is maintained and the Rh sites

are proposed to be still located at ST units as in Rh@MIL-101. Therefore, the conversion of cyclohexene is still very low.

3.2.4.2. Rh@MesoMIL-2

The total conversion vs. the reaction time in the hydroformylation of *n*-alk-1-enes over Rh@MesoMIL-2 is shown in Figure 72. The Rh@MesoMIL-2 is a highly active catalyst. It is more active than Rh@MIL-101 and also Rh@MesoMIL-1. The total conversion of *n*-hex-1-ene reaches 100% after only 1 h of reaction. In contrast to Rh@MIL-101, high conversion is achieved even with the very long chain *n*-hexadec-1-ene (Figure 72) pointing to a very open pore structure of nanometer size compared to pore openings of MIL-101 in sizes of 12 Å and 14.5 Å. The very high conversion of *n*-hexadec-1-ene over Rh@MesoMIL-2 indicates that the pore system of this material is very open due to the mesostructure. The catalytic results are in accordance with the material characterization. As stated, the loss of micropores and the formation of large mesopores are indicated by the course of the nitrogen adsorption-desorption isotherm of MesoMIL-2 (Figure 41c). The nanoporosity is confirmed by the TEM images (Figure 40b). Interestingly, the "octene effect", i.e., the lower conversion achieved with *n*-oct-1-ene compared to the longer chain alkenes, always found with Rh@MOF-5, Rh@IRMOF-3, Rh@MIL-101, and even Rh@MesoMIL-1, is not observed with Rh@MesoMIL-2. The total conversions are in the expected order: *n*-hex-1-ene >*n*-oct-1-ene > *n*-dec-1-ene > *n*-dodec-1-ene >*n*-hexadec-1-ene (Figure 72). The results confirm the high accessibility of active Rh sites.

Figure 72. Total conversion of *n*-alk-1-ene in hydroformylation catalyzed by Rh@MesoMIL-2. Reaction conditions: olefin/Rh = 100000/1, T = 100 ^{o}C, and p= 50 bar.

Table 11. Hydroformylation of cyclohexene catalyzed by Rh@MesoMIL-2. Reaction conditions: olefin/Rh = 100000/1, T = 100 °C, p= 50 bar.

Reaction time (h)	Total conversion/Yield of aldehyde of cyclohexene (%)	
	Rh@MesoMIL-2	Rh@IRMOF-3
1	3.7	2.8
3	11.9	11.2
5	19.7	18.6
21	92.8	85.5

Interestingly, the high conversion (yield of aldehyde) is also found with cyclohexene (Table 11). The result is very different from that of Rh@MIL-101 (Figure 67) and that of Rh@MesoMIL-1 (Table 10). This finding additionally confirms that the framework of Rh@MesoMIL-2 is very open and the rhodium active sites are easily accessible even compared to the mesostructured Rh@MesoMIL-1 catalyst. This might be a result of the deeper "cutting" of the MOF structure. The TEM image clearly shows the nanoporosity inside the irregularly shaped agglomerated particles. This structure allows the bulky/big molecules like cyclohexene and hexadecene to access to active sites easily. The catalytic behavior of Rh@MesoMIL-2 in the hydroformylation of cyclohexene is somewhat similar to that of Rh@IRMOF-3 as shown in Table 11. As explained in chapter 3.1.2, the IRMOF-3 contains a hierarchically structured micro–meso–macro pore system in between the nanoparticles improving access to active sites.
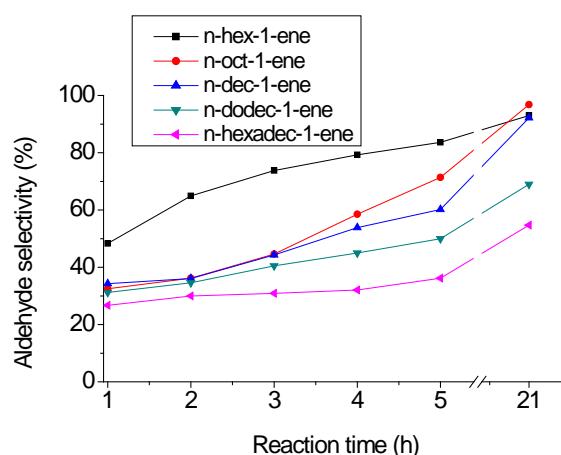
Figure 73. Selectivity to aldehyde in hydroformylation of *n*-alk-1-ene catalyzed by Rh@MesoMIL-2. Reaction conditions: olefin/Rh = 100000/1, T = 100 °C, and p= 50 bar.

The aldehyde selectivities continuously increase during the course of reaction (Figure 73) indicating that the formed internal alkenes are further hydroformylated to the

corresponding aldehydes. The aldehyde selectivity of *n*-hexadec-1-ene is only slightly changed during 1–5 h of reaction due to the low conversion.
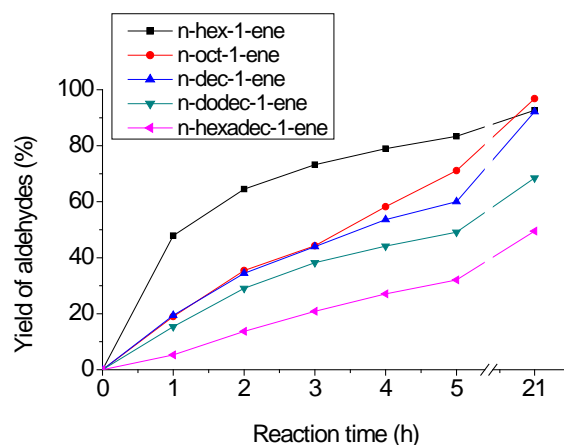
Figure 74. Yield of aldehydes in hydroformylation of *n*-alk-1-ene catalyzed by Rh@MesoMIL-2. Reaction conditions: olefin/Rh = 100000/1, *T* = 100 °C, and *p*= 50 bar.

The yields of aldehydes are shown in Figure 74. They steadily increase corresponding to the total conversions and the aldehyde selectivities. The yield achieved with *n*-hexadec-1-ene up to *ca.* 50% is significantly higher than over other Rh@MOF catalysts even the Rh loading is low.
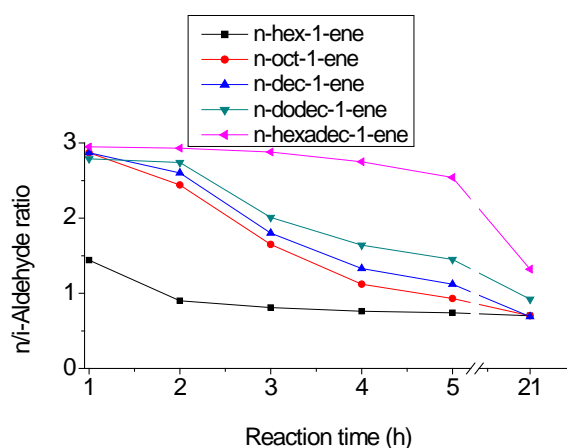
Figure 75. *n/i*-Aldehyde ratio in hydroformylation of *n*-alk-1-ene catalyzed by Rh@MesoMIL-2. Reaction conditions: olefin/Rh = 100000/1, *T* = 100 °C, and *p*= 50 bar.

The *n/i*-aldehyde ratios with Rh@MesoMIL-2 are shown in Figure 75. The ratio reflects the total conversion. The *n/i*-aldehyde ratio is very low for *n*-hex-1-ene and increases with the chain lengths of the *n*-alk-1-enes. The exceptional high conversion of terminal hex-1-ene leads to an instant increase of internal hexenes in the reaction solution, which are subsequently converted to corresponding *i*-aldehydes. On the

contrary, the lower total conversion of *n*-hexadec-1-ene maintains a high level of *n*-alkene in the reaction solution leading to its high *n/i*-aldehyde ratio.

In summary, Rh@MesoMIL-2 is very active and selective in the hydroformylation of olefins to aldehydes. However, the *n/i*-aldehyde ratio is decreased compared to other Rh@MOF catalysts. The high meso and nanoporosity obtained by "cutting" the MOF structure leads to a remarkable increase of the mass transfer and accessibility of Rh active sites, which facilitates the total conversion even with the large *n*-hexadec-1-ene and the hardly to convert cyclohexene. The high conversion is achieved for all substrates regardless of the very low rhodium content points to the well dispersion of rhodium sites in the MesoMOF framework, too. The different behavior of Rh@MesoMIL-2 from Rh@MesoMIL-1 indicates that the windows/pore openings of the ST units, which are considered as "side pockets", are now opened by the use of the organic template for the mesopore construction.

3.2.5.　Rh@MIL-77 and Rh@MIL-96

The catalytic performance in the hydroformylation of *n*-hex-1-ene over **Rh@MIL-77** is presented in Figure 76.
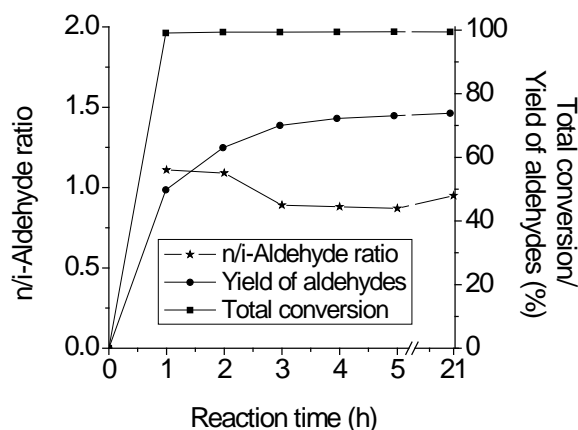
Figure 76. Total conversion and yield of aldehydes in hydroformylation of *n*-hex-1-ene catalyzed by Rh@MIL-77. Reaction conditions: olefin/Rh = 100000/1, $T = 100\ ^{\circ}C$, $p= 50$ bar.

As shown, *n*-hex-1-ene is immediately converted and the total conversion reaches a maximum value after a very short reaction time (less than 1 h). Rh@MIL-77 contains very small, inaccessible pores, hardly to access for *n*-hex-1-ene. Therefore, the reaction should take place at the outer surface of the catalyst particle. Even though the

70

catalyst contains low rhodium (0.1 wt%), the extremely high conversion points to the high dispersion of the rhodium active sites on the material. The aldehyde selectivity is high and slightly increases from 50% at the beginning to *ca.* 72% after the prolonged reaction time due to the conversion of formed internal alkenes to the corresponding *i*-aldehydes. As a result, the selectivity to linear aldehyde is comparatively low and the *n/i*-aldehyde ratio decreases from *ca.* 1.1 to 0.9 during the course of reaction. The results, i.e., high activity and high selectivity to aldehydes but very low selectivity to linear aldehydes, indicate that the reaction takes place at rhodium sites located at the external surface of the catalyst.

Table 12. Hydroformylation of cyclohexene catalyzed by Rh@MIL-77. Reaction conditions: olefin/Rh = 100000/1, T = 100 ^{o}C, p= 50 bar.

Reaction time (h)	Total conversion/ Yield of aldehyde (%)
1	6.7
3	20.2
5	30
21	72.7

The data presented in Table 12 show the conversion/yield of aldehydes in the hydroformylation of cyclohexene. The cyclohexene molecule is too big to enter the pore system of MIL-77. Hence, the observed very high activity (conversion) also indirectly proves that, the reaction takes place on the surface of the catalyst and the rhodium sites are well dispersed (single sites).

The framework of **MIL-96** contains three types of cages in which the biggest ones have free diameter of *ca.* 8.8 Å but the pore-opening diameters of the largest cages are quite small and of *ca.* 2.5−3.5 Å (chapter 2.2.3.1). These pore windows are too small to be passed by most guest molecules.

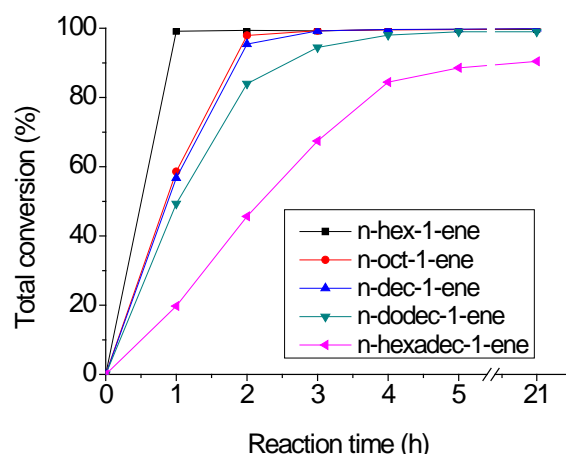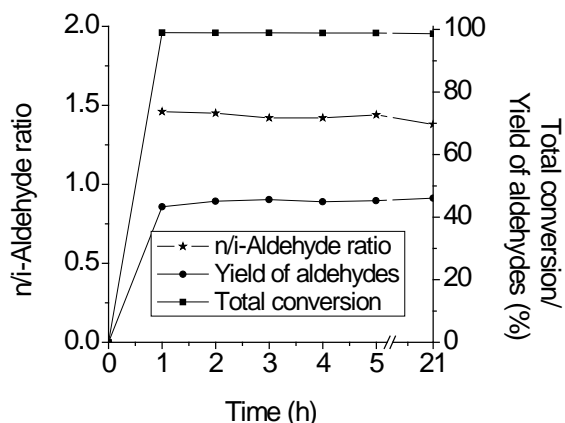**Figure 77.** Total conversion and yield of aldehydes in hydroformylation of *n*-hex-1-ene catalyzed by Rh@MIL-96. Reaction conditions: olefin/Rh = 100000/1, $T = 100\ ^{\circ}C$, $p = 50$ bar.

The catalytic performance of **Rh@MIL-96** in hydroformylation of *n*-hex-1-ene is presented in Figure 77. As Rh@MIL-77, this catalyst is very active. The total conversion and maximum aldehyde formation are already achieved after 1 h of reaction. The yield of aldehydes reaches *ca.* 45% and is not changed during the course of reaction. The *n/i*-aldehyde ratio remains at *ca.* 1.5. The reaction is completed after 1 h. Obviously, the formed internal hexenes in the reaction solution are not converted to the corresponding *i*-aldehydes. The constant yield of aldehydes of only *ca.* 45% verifies that Rh leaching does not happen during the course of reaction or the leached Rh, if occurs, is not active. The very speedy reaction together with the unchanged *n/i*-aldehyde ratio of *ca.* 1.5, which is low compared to other porous Rh@MOFs but higher than Rh@MIL-77 of *ca.* 0.9, demonstrates that the reaction takes place on the surface of the catalyst. The enhanced *n/i*-aldehyde ratio of Rh@MIL-96 compared to Rh@MIL-77 points to a "surface curvature and confinement effect", which prevents the conversion of internal hexenes. Such effect can be due to surface holes. E.g., the bowl-shaped or concave surfaces can be created by cutting cages of the MOF structure at the particle surface. This way modulates surface shape in which the active sites are located in the "holes", prohibits the access of the internal hexenes to the active sites and the formation of *i*-aldehydes. Such an explanation is plausible since the internal hexene molecules are linear shaped and stiff due to the location of the internal C=C group in the middle of the molecule surrounded by space demanding alkyl groups, i.e., $-CH_3$ and $CH_2-CH_2-CH_3$ or two $-CH_2-CH_3$ groups on both of the two sides. On the contrary, the terminal hex-1-ene molecule can be easy to arrange the double bond at the head of the molecule to get in touch with the rhodium active sites;

72

thus, it is quickly converted. When all starting *n*-hex-1-ene has been reacted, the reaction is stopped. As a result, the *n/i*-aldehyde ratio of 1.5 keeps constant even after a prolonged reaction time (21 h).

The conversion/yield of aldehyde in the hydroformylation of cyclohexene is shown in Table 13. Rh@MIL-96 is very active in this reaction showing improved access of cyclohexene to the active surface sites. The observed conversion is comparable or slightly lower than that observed with Rh@MIL-77, where the catalysis also takes place at the surface of the catalyst particle.

Table 13. Hydroformylation of cyclohexene catalyzed by Rh@MIL-96. Reaction conditions: olefin/Rh = 100000/1, T = 100 ^{o}C, p = 50 bar.

Reaction time (h)	Total conversion/Yield of aldehyde (%)
1	6.0
3	14.7
5	23.9
21	58.6

In short, the catalysts based on the small pore-sized MOFs, Rh@MIL-77 and Rh@MIL-96, are very active in the hydroformylation of olefins regardless of low rhodium contents. Due to the reactions occurring on the surface, the reactions proceed very fast but the selectivities to linear aldehydes are low.

Summary - Catalysis of Rh@MOFs

Based on the catalytic data achieved in the hydroformylation of olefins with different structures and chain lengths over Rh@MOFs, it is concluded that

- All Rh@MOFs are highly active in the hydroformylation of olefins although high olefin/catalyst ratios of up to *ca.* 100000 based on Rh are used. It is due to the "single site" nature of active Rh in the MOF frameworks.
- The catalytic performance, the activity and the selectivity, are highly affected by the structure and textural properties of the MOF supports. Highest total conversion is found with catalysts in which Rh sites are free accessible at the catalyst surface as present in small pore-sized/inaccessible Rh@MIL-77 and Rh@MIl-96 or at the wall of extra-large nanoporous Rh@MesoMIL-2.

- Porous Rh@MOFs catalysts behave size selective. The total conversion of *n*-alk-1-enes increases with the increasing pore size. Over a catalyst based on an extra-large pore MOF, the large or bulky molecules like *n*-hexadec-1-ene and cyclohexene are quickly converted. Except for *n*-oct-1-ene, the total conversion of *n*-alk-1-enes decreases with the increasing molecule size.

- Due to the confinement effect in the micropore, the selectivity to linear aldehyde, *n/i*-aldehyde ratio, is enhanced up to *ca.* 3. After conversion of starting *n*-alk-1-enes, formed internal alkenes are further converted to corresponding *i*-aldehydes leading to a decrease of *n/i*-aldehyde ratio.

- Rh@IRMOF-3 is more active than Rh@MOF-5 even though the pore size of IRMOF-3 is apparently smaller compared to that of MOF-5. This can be explained by a hierarchically structured micro–meso–macro porous system existed in IRMOF-3 particles reducing the pathway of diffusion of reactants. This can also be the reason for the high conversion of cyclohexene over Rh@IRMOF-3.

- In contrast to other Rh@MOFs, internal alkenes are not further converted over Rh@MIL-101 because the Rh active sites are located in less accessible positions in microporous ST units, which hinder access of the internal alkenes to the active sites. A similar effect is found with small pore Rh@MIL-96 indicating a "surface curvature" effect. A small decrease of *n/i*-aldehyde ratio in case of Rh@MIL-101 is caused by aldol condensation consuming previously formed *n*-aldehyde facilitated by the coordinative unsaturated chromium sites.

- The introduction of mesostructure into the MIL-101 framework improves the catalytic activity (conversion) and the yield of aldehyde by further conversion of formed internal alkenes as shown in reactions over Rh@MesoMILs. However, the selectivity to linear aldehyde, the *n/i*-aldehyde ratio, is reduced.

- *n*-Oct-1-ene shows an unusual behavior in the hydroformylation. Its total conversion is lower than that of larger *n*-alk-1-enes (*n*-dec-1-ene and *n*-dodec-1-ene). This effect is more pronounced with medium pore-sized Rh@MOFs. But with extra-large pore Rh@MesoMIL-2 the *n*-oct-1-ene is faster converted than the larger *n*-alk-1-enes as expected. This is assigned to the confinement effect in the pores.

3.3. Structure-Catalytic Property-Relationships

- **The catalytic performances of different Rh@MOFs: the hydroformylation of *n*-hex-1-ene as a model reaction**

The total conversion of *n*-hex-1-ene in the hydroformylation over the different Rh@MOF catalysts: small pore-sized (Rh@MIL-77 and Rh@MIL-96), medium pore-sized (Rh@IRMOF-3 and Rh@MOF-5), large pore-sized (Rh@MIL-101), and extra-large pore-sized (Rh@MesoMIL-1 and Rh@MesoMIL-2) catalysts after 1 h of reactions are shown in Figure 78. The catalysts, where the reaction takes place at the catalyst surface due to inaccessible pores (Rh@MIL-77 and Rh@MIL-96) or in big nanopores (Rh@MesoMIL-2), show highest activities. In these cases, mass transfer and access to the Rh active sites are obviously not hindered. In contrast, the conversion achieved with Rh@IRMOF-3 and Rh@MOF-5 (medium pore size), Rh@MIL-101 (large pore size), and Rh@MesoMIL-1 is markedly lower indicating that the reaction takes place in the pores of MOFs, which might have restricted mass transfer and access to the active sites. The conversion is higher with the Rh@MIL-101 catalyst compared to the smaller pore-sized IRMOF-3 and MOF-5 based catalysts additionally showing the impact of the pore system (size) on the conversion.
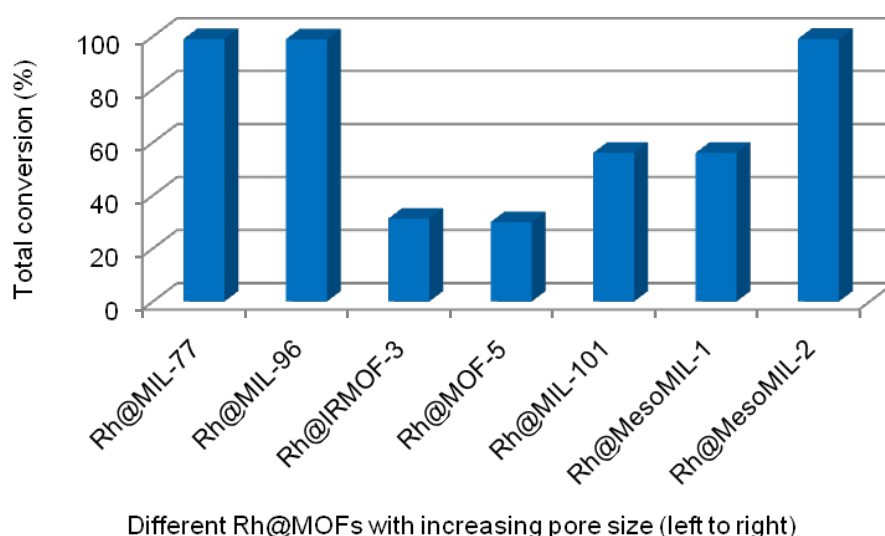
Figure 78. Total conversion of *n*-hex-1-ene in hydroformylation catalyzed by different Rh@MOFs. Reaction conditions: $T = 100\ ^{o}C$, $p = 50$ bar, $t = 1$ h.

The different access to the active sites depending on the location of Rh at the surface or in the pores of the MOF framework is also reflected in the aldehyde selectivities (Figure 79).
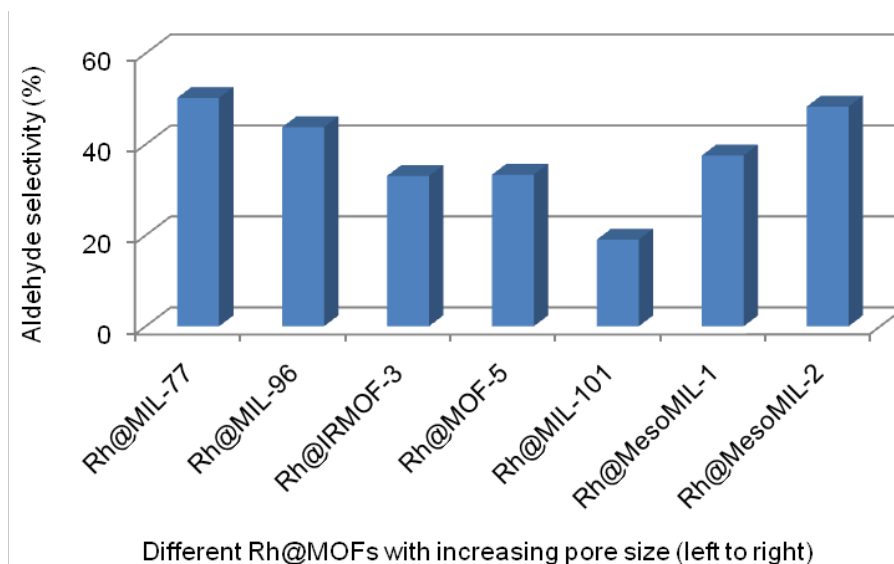
Figure 79. Selectivity to aldehydes in hydroformylation of *n*-hex-1-ene catalyzed by different Rh@MOFs. Reaction conditions: T = 100 ^{o}C, p= 50 bar, t = 1 h.

They are highest for the nanoporous catalysts and the small pore-sized MIL-77 and MIL-96 based catalysts, which provide easy access to the active sites. But aldehyde selectivities for the medium pore-sized MOF-5 and IRMOF-3 and large pore-sized MIL-101 based catalysts are lower. These results again confirm the strong impact of the catalyst pore system on the catalytic performance. Lower conversions and aldehyde selectivities result in the lowest aldehyde yields for the medium pore-sized catalysts (Figure 80).

Even though the total conversion over large pore-sized Rh@MIL-101 is higher than over medium pore-sized Rh@IRMOF-3 and Rh@MOF-5, the aldehyde selectivity is distinctly lower. This surprising finding can be explained by the location of Rh in the microporous supertetrahedra (ST) forming the wall of large cages. Mass transfer is facilitated by large pores enhancing the total conversion (formation of aldehydes and internal alkenes). However, the steric more demanding hydroformylation of internal alkenes is more restricted with the smaller ST cages (medium-sized pores) compared to the more open channel system of the MOF-5 and IRMOF-3 framework. As a result, even with the high total conversion the yield of aldehydes is low with Rh@MIL-101.
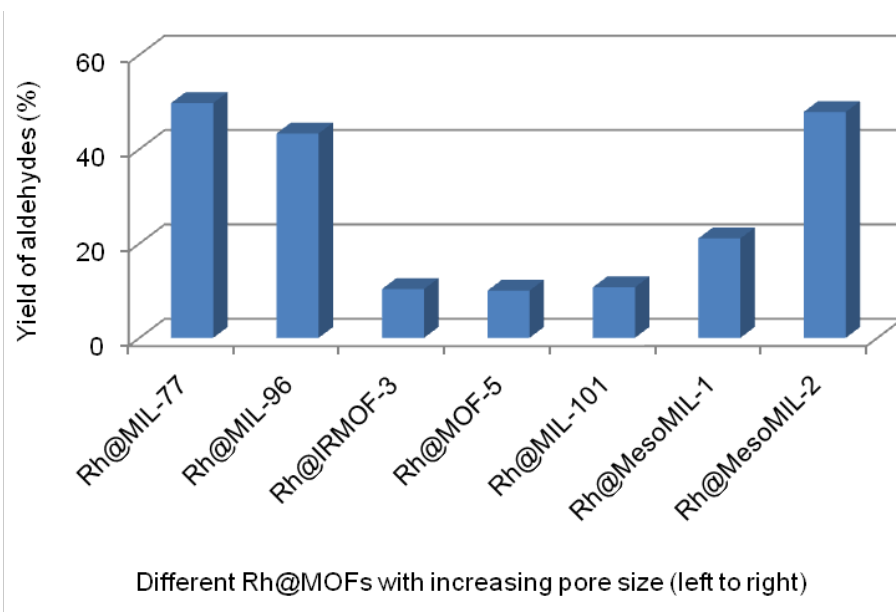
Figure 80. Yield of aldehydes in hydroformylation of *n*-hex-1-ene catalyzed by different Rh@MOFs. Reaction conditions: $T = 100\ ^{\circ}C$, $p = 50$ bar, $t = 1$ h.

In case of Rh@MesoMIL-1, the catalytic performance is determined by the remaining MIL-101 structure. However, the introduction of mesoporosity leads to a partial "cutting" of the large pores and the loss of the internal surface curvature effect. The access to the Rh sites is improved resulting in an enhanced conversion to aldehydes compared to Rh@MIL-101. However, the shape selectivity (*n/i*-aldehyde ratio) is decreased (Figure 81).
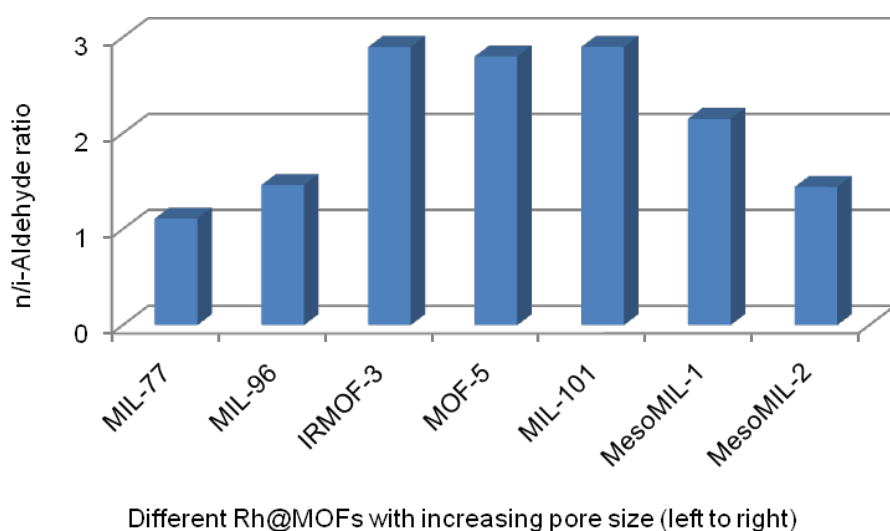
Figure 81. *n/i*-Aldehyde ratio in hydroformylation of *n*-hex-1-ene catalyzed by different Rh@MOFs. Reaction conditions: $T = 100\ ^{\circ}C$, $p = 50$ bar, $t = 1$ h.

Accordingly, highest shape selectivities with *n/i*-aldehyde ratios of *ca.* 3 are observed with medium pores present in the frameworks of MOF-5, IRMOF-3, and MIL-101 (ST units). The reaction takes place in the confined space of pores. Catalysts, where the reaction takes place preferentially at the surface or in extra-large nanopores, show markedly lower shape selectivities. Despite the differences between the Rh@MOF catalysts, the catalytic activities are generally high for all the samples. After 3 h of reaction, *ca.* 90% and more of the starting materials (*n*-alk-1-enes) are converted to aldehydes and internal alkenes (Figure 82).
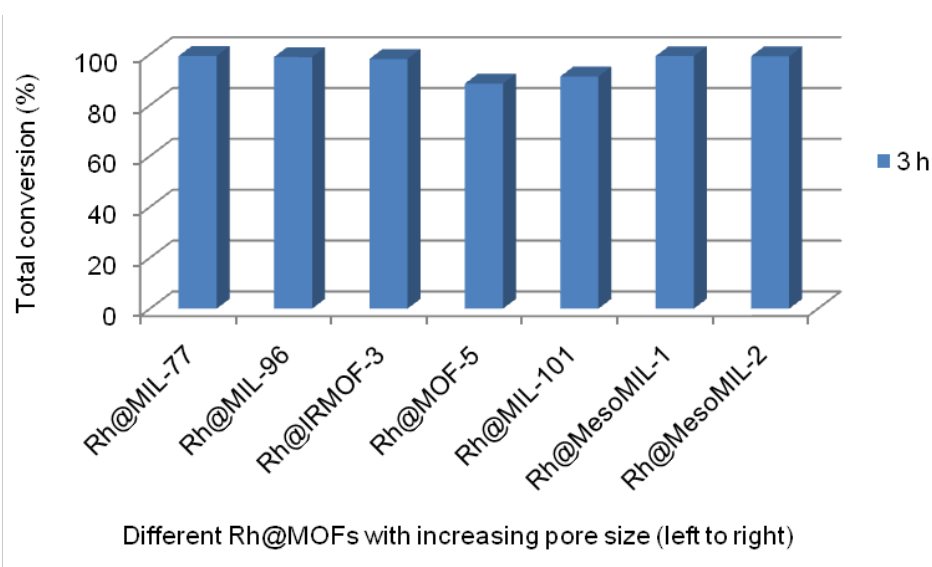
Figure 82. Total conversion of *n*-hex-1-ene in hydroformylation catalyzed by different Rh@MOFs. Reaction conditions: $T = 100 \,^{\circ}$C, $p = 50$ bar, $t = 3$ h.

Beyond 3 h the aldehyde yields markedly increase with Rh@IRMOF-3 and Rh@MOF-5 indicating the conversion of formed internal alkenes to *i*-aldehydes (Figure 83) leading to a decrease of the *n/i*-aldehyde ratio (Figure 49 and Figure 60). Interestingly, the internal alkenes are nearly not converted over Rh@MIL-101 and Rh@MIL-96. These catalysts behave strictly selective. As with Rh@MIL-96 the reaction takes place at the catalyst surface. The finding points to a surface curvature effect present on this catalyst.
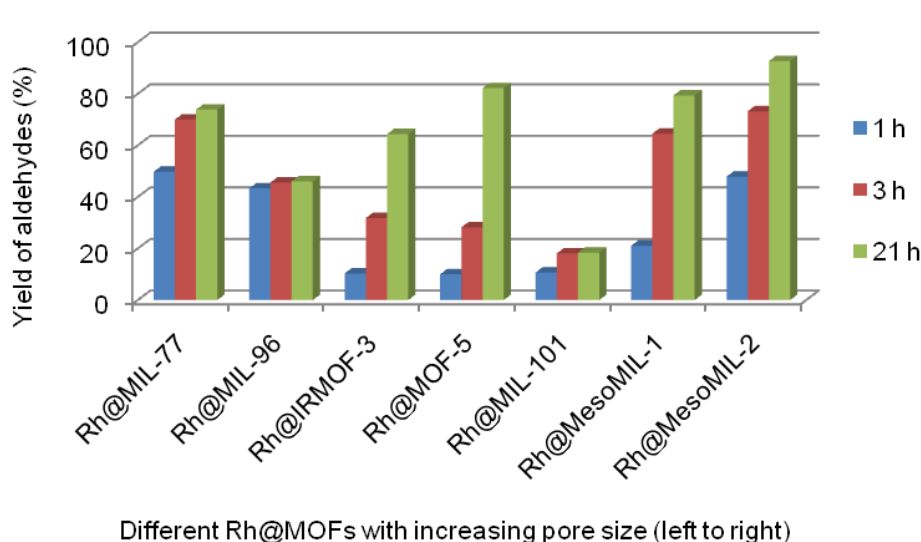
Figure 83. Yield of aldehydes in hydroformylation of *n*-hex-1-ene catalyzed by different Rh@MOFs. Reaction conditions: *T* = 100 °C, *p*= 50 bar, *t* = 1, 3, 21 h.

- **The reaction of cyclohexene**

The conversion of cyclohexene over the Rh@MOF catalyst is a good indicator for the accessibility of the Rh sites (Table 14).

Table 14. *H*ydroformylation of cyclohexene catalyzed by different Rh@MOFs arranged with the increasing pore size order after several selected reaction times. Reaction conditions: *T* = 100 °C, *p*= 50 bar.

Reaction	Total conversion/Yield of aldehyde of cyclohexene over different Rh@MOFs (%)						
time (h)	MIL-77	MIL-96	IRMOF-3	MOF-5	MIL-101	MesoMIL-1	MesoMIL-2
1	6.7	6.0	2.8	1.2	0.4	-	3.7
3	20.2	14.7	11.2	2.8	2.8	-	11.9
5	30.0	23.9	18.6	3.9	5.5	6.8	19.7
21	72.7	58.6	85.5	15.2	19.3	14.0	92.8

With catalysts, where the reaction takes place at the catalyst surface (Rh@MIL-77 and Rh@MIL-96) or in the big nanopores (Rh@MesoMIL-2) the conversions of cyclohexene to aldehyde are comparatively high with *ca.* 60–90% after 21 h. The improved conversions point to the high accessibility of the Rh sites. The somewhat lower conversion of cyclohexene over Rh@MIL-96 compared to Rh@MIL-77 is in agreement with the previous finding that internal hexenes are nearly not converted to *i*-aldehydes over Rh@MIL-96.

79

With medium pore-sized IRMOF-3 and MOF-5 as well as large pore-sized MIL-101 supported catalysts, the initial conversions are low indicating restricted access of the active sites in pores of the framework. This finding confirms that the Rh is located in less accessible side pockets (ST units) of MIL-101 as proposed above.

Interestingly, high conversions are also observed with Rh@IRMOF-3 after long reaction times. The IRMOF-3 consists of small nanoparticles of *ca.* 10–15 nm size, which are easily accessible via a hierarchically structured meso–macro pore system in between the nanoparticles. Additionally, the diffusion pathway of the molecule in the catalyst is substantially reduced due to the small size of the nanoparticles, which corresponds to the length of *ca.* 4–6 unit cells, $a_0 = 2.57$ nm[144,145] or 8–12 cages. Both lead to the improvement of mass transfer of the molecules in this catalyst compared to the more open MOF-5 structure and, hence, to an enhancement of conversion. This finding is in agreement with the increased conversion of internal alkenes after a prolonged reaction time observed with this catalyst.

- **Anomalous catalytic behavior of *n*-oct-1-ene**

As stated in chapter 3.2, **decreased conversion** of the *n*-oct-1-ene is observed over porous Rh@IRMOF-3, Rh@MOF-5, Rh@MIL-101, and Rh@MesoMIL-1 compared to that of longer *n*-alkenes as *n*-dec-1-ene and *n*-dodec-1-ene. The difference of total conversions between *n*-oct-1-ene and *n*-dodec-1-ene over the different MOF catalysts is presented in Figure 84.

As previously discussed, the more linear shaped long-tailed *n*-oct-1-ene molecule with its chain length of *ca.* 10 Å (similar to the pore sizes of medium pore-sized MOFs) is difficult to arrange at the Rh active sites in the confined space of the pores or approach to Rh at ST units is limited by the internal surface curvature of large pores in MIL-101 (Figure 65). This effect is diminished and finally disappears with increasing access in the extra-large nanopores of MesoMIL-2 (Figure 72).
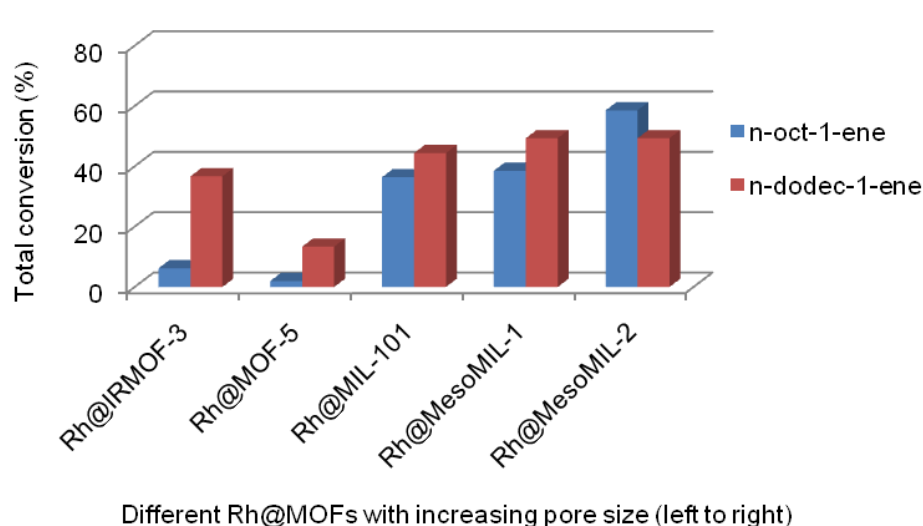
Figure 84. Comparison of total conversion between *n*-oct-1-ene and *n*-dodec-1-ene in hydroformylation catalyzed by different Rh@MOFs after 1 h of reaction. Reaction conditions: $T = 100\ ^{\circ}C$, $p = 50$ bar.

Severe changes in the **course of conversion** are observed with the medium pore-sized MOF-5 and IRMOF-3 catalysts, where the pore diameters fit the size of molecule (confinement effect). Very low conversion of *n*-oct-1-ene is observed in an initial induction period followed by a sudden increase of the conversion, indicating that the pore is open. It is proposed that the *n*-oct-1-ene is jammed in nearby crystal surface cavities blocking up the pores because its size just fits the cage.

After reaching a critical loading, the *n*-oct-1-ene becomes able to move in the pores leading to a sudden increased conversion (Figure 85).
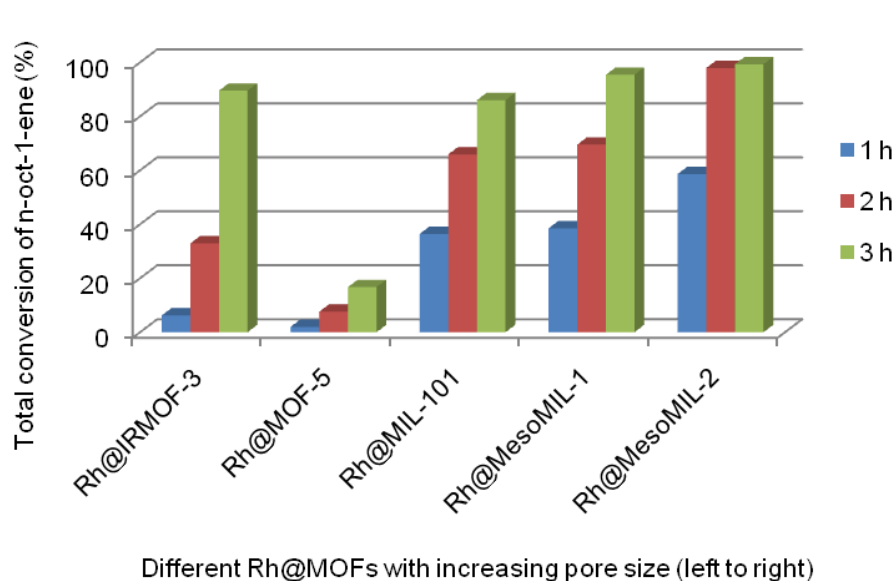
Figure 85. Total conversion of *n*-oct-1-ene in hydroformylation catalyzed by different Rh@MOFs after 1 h and 3 h of reaction. Reaction conditions: $T = 100\ ^{\circ}C$, $p = 50$ bar.

81

The passing of the *n*-oct-1-ene molecule through the window induces a switching of the orientation of the phenylene linker in the framework in a manner that the planes of the linkers are oriented in parallel to the passing molecule, perpendicular to the window opening. The other two pore directions are blocked. This leads to the formation of a "quasi" one-dimensional, in parallel arranged, channel system, which is connected with enhanced directed diffusion of the molecules. These changes explain the sudden increase of the conversion of *n*-oct-1-ene after an initial induction period of *ca.* 1–2 h.

This conclusion is based on the following considerations and findings. The **orientation of the linker** markedly modulates the effective size of the window. There exist preferred linker orientations, leading to the formation of structural isomers by distortion of the MOF lattice, which could be identified by XRD structural analysis.[144]

The rotations of the phenylene groups[146,147] are not independent from each other and from the lattice of the MOF. They cause lattice distortions and atom displacements. Therefore, concerted changes (domino effect) of the linker orientation in the direction of the molecule pathway can be induced by local changes of the lattice by window passing molecules. These changes lead to collective changes in the MOF lattice creating quasi one-dimensional channels of enhanced directed molecule motion (single-file diffusion) compared to the three-dimensional pore system. The planar phenylene groups of the linkers act as a "lamellar curtain". Concerted switching of orientation by the linker rotation modulates the effective window size in the MOF between fully open and partially closed (Figure 86), which has not been considered so far.
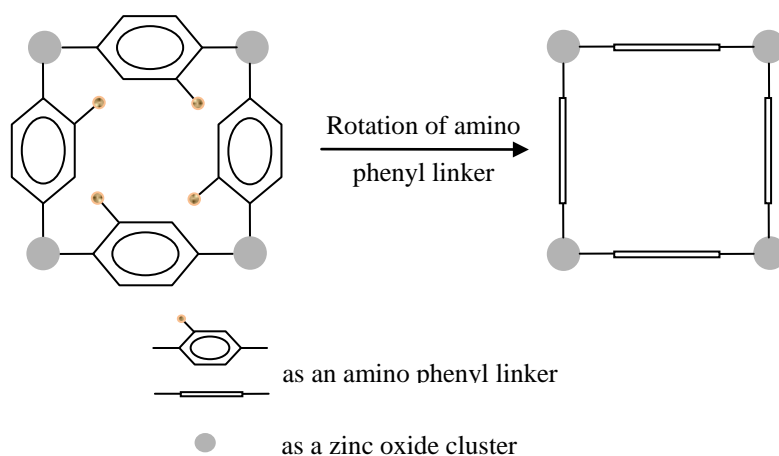
Figure 86. Modulation of the window size by rotation of amino phenylene linker in IRMOF-3.

The proposed occurrence of **single-file diffusion** is supported by the conversion behavior of *n*-alk-1-ene mixture over Rh@MOF-5, where the conversions of different sized *n*-alk-1-enes are equalized and different from those of the single component behaviors. The enhanced conversion is observed with larger *n*-alk-1-ene molecules in the reactions of mixtures of *n*-hex-1-ene/*n*-oct-1-ene/cyclohexene (Figure 51) and *n*-hex-1-ene/*n*-dodec-1-ene/TMP.

Furthermore, NMR spectroscopic diffusivity studies show high liquid-like mobility of *n*-hexane and other molecules in MOF-5 for 50-60% of the adsorbed molecules. The remaining 40-50% of molecules shows a distinctly, *ca.* 10 times, lower mobility, indicating partial pore blocking.[148] Specific linker orientations can be the reason of such differences. The high diffusivity observed with MOF can be explained by the occurrence of single-file diffusion, which is enhanced compared to restricted diffusion in three-dimensional systems, because the molecules cannot pass each other.[112,149]

Finally, it is concluded that the linker in MOFs are not likely randomly oriented. In the case that the molecule fits the size of the channel, the diffusivity is enhanced by the single-file diffusion mode caused by special orientations of the linkers opening the pores.

The following **Structure-Catalytic Property-Relationships** in the hydroformylation of different sized *n*-alk-1-enes and the bulky cyclohexene over Rh supported MOF catalysts can be derived:

- The high catalytic activity of the Rh@MOF catalysts is ascribed to the single site dispersion of the Rh active sites within the porous framework of the inorganic-organic hybrid material. The specific catalytic performance of the catalysts is markedly affected by the structure and textural properties of the MOF supports. In the first stage of reaction (less than 5 h) the starting terminal *n*-alk-1-enes are converted prior to formed internal alkenes.

- The total conversion of *n*-alk-1-enes over the porous metal organic framework catalysts mostly increases with the increasing pore size in the order:

medium pore < large pore < extra-large mesostructured pore

< small/inaccessible pore, i.e.,

MOF-5 < MIL-101< IRMOF-3 < MesoMIL-1 < MesoMIL-2

< MIL-96 < MIL-77.

Highest activity (total conversion) is observed with small pore-sized catalysts, where the reaction takes place at the external catalyst surface or at the walls of large nanopores (MesoMILs). Even though the pore of the IRMOF-3 support is smaller than that of the MOF-5 support, higher conversions for *n*-alk-1-enes are shown with Rh@IRMOF-3due to enhanced access by the hierarchically structured micro–meso–macro pore system.

- A similar effect of the MOF structure on the catalytic property is found with the more bulky cyclohexene molecule, which shows lower conversion compared to *n*-alk-1-enes:

MOF-5 < MIL-101 < MesoMIL-1 < MesoMIL-2 ≈ IRMOF-3

< MIL-96 < MIL-77.

Again improved conversion is observed with IRMOF-3 even its pore size is smaller than of MOF-5 or MIL-101 probably due to the very small crystal size. The mesostructuring of MIL-101 results in an open structure with cut cages improving access to the Rh active. Consequently, high conversion is achieved with Rh@MesoMIL-2.

- The conversion of *n*-alk-1-enes decreases with the increasing chain length except for *n*-oct-1-ene, which shows an unexpected low conversion compared to the longer *n*-dec-1-ene and *n*-dodec-1-ene:

n-hex-1-ene > *n*-dec-1-ene > *n*-dodec-1-ene > *n*-oct-1-ene > *n*-hexadec-1-ene

- The selectivity to aldehydes is similar for the different porous MOF supports (*ca.* 30 to 35%), but higher for MIL-77 or MIL-96 (50 and 45%), where the reaction takes place at the surface:

MIL-77 > MIL-96 > MIL-101≈ MesoMILs ≈ MOF-5 ≈ IRMOF-3.

The similarity found with porous MOFs can be rationalized in terms of the location of Rh at the small cages of the MIL-101 structure (supertetrahedra). They have a similar pore size as MOF-5 or IRMOF-3.

- The *n/i*-aldehyde ratio follows in an opposite manner. It is lowest with MIL-77 and MIL-96 (*ca.* 1.2 and 1.5) compared to porous MOFs (*ca.* 3).

$$\text{MIL-77} < \text{MIL-96} < \text{MIL-101} \approx \text{MesoMILs} \approx \text{MOF-5} \approx \text{IRMOF-3}.$$

The improved selectivity is due to the confinement in the limited space of the pores with porous MOFs and the surface curvature effect with MIL-96 compared to MIL-77.

- The hydroformylation of formed internal alkenes to *i*-aldehydes starts after conversion of starting *n*-alk-1-enes leading to an additional increase of the aldehyde selectivity after prolonged reaction time (21 h):

$$\text{MIL-101} < \text{MIL-96} \approx \text{MOF-5} < \text{IRMOF-3} \approx \text{MIL-77}$$
$$< \text{MeseoMIL-1} < \text{MesoMIL-2}.$$

With enhanced accessibility of the Rh active sites the conversion of alkenes to aldehydes increases to *ca.* 45% (Rh@MOF-5) and *ca.* 75% (Rh@MIL-77) or to *ca.* 90% (MesoMIL-2). The *n/i*-aldehyde ratio decreases correspondingly. Over Rh@MIL-101 and Rh@MIL-96 internal alkenes are nearly not converted showing the strict shape selectivity.

- The anomalous low conversion of *n*-oct-1-ene compared to longer chain *n*-alk-1-enes is explained by the fact that the stiff long *n*-oct-1-ene molecule is difficult to arrange at the active sites in the confined space of the MOF-5 and IRMOF-3 pores or the curvature of the pore wall of MIL-101, which limits the approach to the Rh site at the ST unit.

Besides the MOF structure, the rotation of the phenylene linkers in the windows of MOF pores has an important impact on the catalytic performance.

- An anomaly is observed in the course of conversion of *n*-oct-1-ene over the medium pore-sized MOF catalysts, where the *n*-oct-1-ene molecule just fits the pores. In this case, the *n*-oct-1-ene gets jammed in the cages and partially blocks up the pores resulting in very low conversion at the beginning of the reaction. After the induction period, the pores are opened and speedy conversion starts. This effect is assigned to a concerted change of the orientation of the linkers by window passing molecules, whereby the pores become open in one direction,

leading to the formation of quasi one-dimensional channels. The other two perpendicular directions are closed. The linkers act as a molecular lamellar curtain (MLC-Effect), which can open and close the windows in certain directions.

- In the one-dimensional channel, a single-file diffusion mode is achieved, which is characterized by markedly enhanced diffusivity and molecules cannot pass each other. This conclusion is independently confirmed by the similar behavior of different sized n-alk-1-enes in the hydroformylation of mixtures. Because the different alkenes are aligned in the channels, their conversions are equal. The conversion of longer n-alk-1-ene is increased. It is higher in the single component reaction. The fast conversion in MOFs is facilitated by single-file diffusion.

4. Conclusion

- Different selected MOFs in the increasing pore-sized order namely MIL-77 and MIL-96 (small pore), IRMOF-3 and MOF-5 (medium pore), MIL-101 (large pore), MesoMIL-1 and MesoMIL-2(extra-large pore) have been prepared to investigate Structure-Catalytic Property-Relationships in the hydroformylation of olefins with different structures and chain lengths to aldehydes.

- As-synthesized MOFs and Rh loaded catalysts were characterized by XRD, FTIR, SEM, TEM, AAS, XPS, SAXS, and nitrogen sorption. The results show that high crystalline MOF samples with the different structures and the properties have been successfully prepared.

- High dispersion of rhodium in single site manner throughout the MOF frameworks has been achieved with the Rh@MOF catalysts. Even with a higher Rh loading of up to 1 wt%, i.e., in one Rh@MIL-101 sample, agglomerated rhodium nanoparticles are not detected, confirming that the hybrid MOFs are good supports for the preparation of the single site catalysts.

- All the Rh@MOF catalysts are highly active in the hydroformylation of olefins even though high olefin/catalyst ratios of up to *ca*. 100000 based on Rh are used in catalytic tests. Nearly complete conversion of *n*-alk-1-enes to aldehydes and internal olefins (side reaction) is achieved.

- The catalytic performances of Rh@MOFs are highly affected by the structure and textural properties of the MOF supports. With porous Rh@MOFs the total conversion increases with the increasing pore size. Also higher catalytic activity is found with small-pore catalysts, Rh@MIL-77 and Rh@MIl-96, where the reaction takes place at the catalyst surface with free access of Rh sites.

- Although MOF-5 and IRMOF-3 are isostructural, the catalytic performances of their Rh supported catalysts are different. Higher catalytic activity is shown with Rh@IRMOF-3 due to its textural properties, i.e., a hierarchical micro-meso-nano pore system and the very small crystal size (10–15 nm) improving mass transfer.

- A selectivity to linear aldehyde, i.e., the *n/i*-aldehyde ratio, of up to 3 is achieved in the hydroformylation of *n*-alk-1-enes over Rh@MOFs. After a long time of reaction, the *n/i*-aldehyde ratio is decreased due to the conversion of formed internal alkenes; therefore, the yield of aldehydes is further increased.

- MIL-101 has high selectivity to terminal alkenes. The internal alkenes are nearly not converted. The proposed special location of the Rh active sites in the ST units hinders access of formed internal alkenes to the active sites leading to the low aldehyde selectivity. A similar effect is found with small pore Rh@MIL-96 but it is due to the "surface curvature" effect.

- The orientation of the phenylene linker seems to have an important impact on the catalytic properties. It modulates the effective pore size by rotation of the linker influencing the diffusivity and, hence, the catalytic activity. It is proposed that concerted switching of the linker orientation can block up or open the pores leading to the creation of preferred "diffusion" channels. Thereby the nature of the three-dimensional pore system is changed to a "quasi" one-dimensional one. This leads to a significant enhancement of the diffusivity of adsorbed molecules by single-file diffusion. The latter has been proven by hydroformylation experiments with n-alk-1-ene mixtures. The linker may act as a molecular lamellar curtain (MLC).

- The catalytic results show that porous metal-organic frameworks are interesting and potential materials for the preparation of metal supported heterogeneous catalysts. They are characterized by a high porosity and specific surface area. The hybrid nature with strictly alternating arrangement of organic and inorganic compartments in the crystal lattice allows site isolation and high dispersion of obtained single sites in the catalysts. The Rh@MOF catalysts are highly active and show selectivity in hydroformylation. Due to the limited thermal and hydrolytic stability, it can be useful for non-aqueous liquid phase reactions, like the hydroformylation of olefins at a low temperature.

5. Experimental

5.1. Preparation of MOFs

Different MOFs are solvothermally synthesized by using different metal salts and dicarboxylic acids with appropriate solvents. The Schlenk-line technique is used in the synthesis and workup of MOF-5 and IRMOF-3. The DMF/DEF solvents for synthesis and CH_2Cl_2 for washing are redistilled and dried over CaH_2 prior to use. MIL-101 is prepared using TMAOH to dissolve H_2BDC. For the better removal of the excess acid crystals H_2BDC from the reaction product containing MIL-101, along with the use of water, the centrifugation at different speeds and times is utilized. This seems to be critical for achieving the high yield of pure MIL-101.

5.1.1. MOF-5

MOF-5 was solvothermally synthesized by the optimized procedure based on literature.[62,101,103,150,151] As starting materials $Zn(NO_3)_2$, H_2BDC, and the solvent DMF were used. The sample of MOF-5 was synthesized as follows.

3.32 g of H_2BDC and 15.69 g of $Zn(NO_3)_2 \cdot 4H_2O$ were dissolved into 500 mL of DMF. The solution was given into a glass reactor, which was equipped with a drying tube on overhead. The mixture was heated to 105 ^{o}C under stirring. Then the mixture was allowed to crystallize by standing at 105 ^{o}C for 24 h under static condition. Thereafter, the reaction mixture was allowed to cool down to room temperature.

The crystallized product was filtered off and washed with 3 x 10 mL of CH_2Cl_2. The recovered solid was suspended in 50 mL of DMF, heated under stirring to 130 ^{o}C, and held at this temperature for 1 h. Then the solid was filtered off and washed 3 times with 10 mL of CH_2Cl_2. Next, it was given into 50 mL of CH_2Cl_2 and stirred for 12 h at room temperature. Thereafter, the solid was again filtered off and washed with 3 x 10 mL of CH_2Cl_2. The repeated work up was conducted in order to remove residual H_2BDC and low volatile DMF solvent in the synthesized product. Finally, the fine powdered as-synthesized MOF-5 was obtained by drying the solid under vacuum at 105 ^{o}C for 12 h.

5.1.2. IRMOF-3

Similar to MOF-5, IRMOF-3 was solvothermally synthesized by an optimized procedure based on literature [60,101]. The starting materials included $H_2NC_6H_3$-1,4-$(COOH)_2$ and $Zn(NO_3)_2$. DEF was used as solvent.

In details, 2.537 g of $H_2NC_6H_3$-1,4-$(COOH)_2$ and 11.003 g of $Zn(NO_3)_2 \cdot 4H_2O$ were dissolved in 350 mL of DEF in a glass reactor, which was equipped with a drying tube on the top filled with calcium hydride. The reaction mixture was heated to 105 ^{o}C under stirring. Then it was allowed to crystallize at 105 ^{o}C for 24 h under static condition. The following work up was carried out under argon atmosphere and use of dried solvents to obtain pure IRMOF-3.

The crystallized product was filtered off and washed three times with 10 mL of CH_2Cl_2. The resulting solid was suspended in 50 mL of DEF and heated under reflux at 130 ^{o}C for 1 h. The solid was filtered off and washed again with 3 x 10 mL of CH_2Cl_2. Next, it was given into 50 mL of CH_2Cl_2, slightly shaken, and allowed to stay overnight at room temperature. The solid was again filtered off and the above mentioned procedure was repeated twice in order to remove non-reacted amino terephthalic acid and the low volatile DEF solvent from the synthesis product. Finally, the product was dried at 105 ^{o}C under vacuum to obtain as-synthesized IRMOF-3.

5.1.3. MIL-101

MIL-101 was hydrothermally synthesized in the presence of TMAOH based on literature[134] using an improved work up procedure. As starting materials, $Cr(NO_3)_3 \cdot 9H_2O$, H_2BDC, and 0.05 M TMAOH were used. Typically, 0.62 g of H_2BDC was added to 18.75 mL of aqueous 0.05 M TMAOH and vigorously stirred for 30 min at room temperature. Then 1.5 g of $Cr(NO_3)_3 \cdot 9H_2O$ was added to the mixture and stirred for further 1 h. Next, this reaction mixture was transferred into a 120 mL Teflon-lined autoclave. It was heated at the rate of 2 ^{o}C/min up to 180 ^{o}C and maintained at this temperature for 24 h under static condition.

After reaction, the autoclave was allowed to cool down to room temperature. The green reaction product was recovered by centrifugation at 4000 rpm for 25 min.

Thereafter, the precipitate was suspended in water. The white large elongated unreacted H$_2$BDC crystals were separated from the reaction product by centrifugation at 1600 rpm for 5 min. The above standing opaque green mixture was decanted and further centrifuged at 4000 rpm for 25 min to recover the MIL-101. The obtained product was worked up four times with the same procedure. Finally, the obtained green as-synthesized MIL-101 sample was dried at 90 °C.

5.1.4.   MesoMILs

Two mesoporous MOF samples based on MIL-101 namely MesoMIL-1 and MesoMIL-2 were prepared by the partner in Vietnam. Similar to MIL-101, the starting materials for the preparation of these mesoporous MOFs include Cr(NO$_3$)$_3$·9H$_2$O, H$_2$BDC, HF, and water. Additionally, CTAB was added as a structure-directing agent in order to induce the meso or nanoporosity. The content of CTAB was increased for pore size expansion. The synthesis mixture of MesoMIL-1 had the following composition: Cr(NO$_3$)$_3$·9H$_2$O/CTAB/H$_2$BDC/H$_2$O = 1/0.25/1/280. For the synthesis mixture of MesoMIL-2, CTAB was increased by 2 times.

5.1.5.   MIL-77 and MIL-96

The small pore-sized metal-organic frameworks namely MIL-77 and MIL-96 were synthesized by Janiak's group (the University of Düsseldorf) according to procedures given in literature.[96,97]

5.2.   Preparation of rhodium supported MOF catalysts

All porous metal-organic framework samples were loaded with the rhodium species in a similar way and equally low concentration. Typically, the rhodium loading procedure for MOF-5 sample was carried out as follows. 10 mg of Rh(acac)(cod) containing *ca.* 32–33 wt% of rhodium were put into a glass beaker containing 28 mL of acetonitrile (Baker) and 20 mL of toluene under stirring. A clear pale yellow solution was formed. Subsequently, 4 g of as-synthesized MOF-5 were added under slight stirring. The suspension was slowly heated to *ca.* 70 °C to evaporate the solvents gradually and to adsorb the rhodium precursor on the MOF-5 support. The material was dry after *ca.* 2.5 h. The obtained product was washed three times with 5

mL of toluum and dried at 70 ^{o}C under vacuum. The resulting Rh@MOF-5 catalyst was stored under argon atmosphere and used for catalytic testing.

The other catalyst samples namely Rh@IRMOF-3, Rh@MIL-101, Rh@MIL-77, Rh@MIL-96, Rh@MesoMIL-1,and Rh@MesoMIL-2 were prepared in the same way.

5.3.   Material characterization

The as-synthesized MOF samples and their rhodium loaded forms, Rh@MOFs, were characterized by XRD, FTIR for structural information, AAS for chemical analysis, and SEM, TEM, and nitrogen sorption measurements for textural studies. Besides, XPS and SAXS measurements were used to investigate the state of rhodium in the Rh@MOFs.

The XRD investigation was carried out on a STADI-P X-ray diffractometer (STOE) using monochromatic Cu$K\alpha$ radiation ($\lambda = 1.5418$ Å). IR spectroscopic measurements were recorded on a Nicollet 380 FTIR spectrometer in attenuated total reflection mode using a smart orbit ATR (Attenuated Total Reflection) device. The resolution was *ca.* 4 cm^{-1}. The powders were measured as obtained. SEM images were received by a DSM 960A electron microscope operating at 10 kV (Carl Zeiss, Oberkochen) with a resolution of 4 nm. The sample was suspended in ethanol/water and put into an ultrasonic bath in order to disperse the solid as much as possible. Then a small drop of the sample suspension was deposited on a sample plate. After drying, the plate containing very small particles of sample was coated with a very thin layer of gold by using plasma distribution method. Next, the sample plate was put into the sample box for SEM investigation. Before scanning, the sample inside the box was under high vacuum (*ca.* 2×10^{-5} hPa). SEM images with the high magnification of 30000 were recorded with a speed of 200 μm/pixel in accordance with the scanning time of *ca.* 3 min. TEM measurements were performed with a LIBRA 120 transmission electron spectrometer (Carl Zeiss, Oberkochen) at 120 kV with a resolution of 0.3 nm. Prior to TEM investigations, similar to SEM, the sample was well dispersed in ethanol/water and then deposited on copper grids. Images were recorded with a digital camera with 2000×2000 pixels. Nitrogen adsorption and desorption measurements were performed on an ASAP 2010 sorption system. Before measurement, the solvent in the

sample was removed by heating and pumping under reduced pressure at *ca.* 150 °C. Nitrogen adsorption measurements were carried out at 77 K (−196 °C).

The rhodium contents of the Rh@MOF supported catalysts were determined by atomic absorption spectrometry with an AAS-Analyst 300 device (Perkin Elmer). A nitrous oxide/acetylene or air/acetylene mixture was used for the burner system. XPS measurements were done at an ESCALAB220iXL spectrometer (Thermo Fisher) with monochromatic AlK_α radiation ($E = 1486.6$ eV). The samples were fixed on a stainless steel sample holder with double adhesive carbon tape. The binding energies were referred to C_{1s} at 284.8 eV. For determination of the binding energy and peak area the peak were fitted with Gaussian-Lorentzian curves. The base pressure of the UHV (ultra-high vacuum) chamber was below 1×10^{-7} Pa. SAXS measurements were carried out with a Kratky-type instrument (SAXSess, Anton Paar, Austria) operated at 40 kV and 50 mA in slit collimation using a two-dimensional CCD detector ($T = -40$ °C). The 2D scattering pattern was converted into a one-dimensional scattering curve as a function of the magnitude of the scattering vector $q = (4\pi/\lambda)\sin(\theta/2)$ with SAXSQuant Software (Anton Paar). A Göbel mirror was used to convert the divergent polychromatic X-ray beam into a collimated line-shaped beam of CuK_α radiation ($\lambda = 0.154$ nm). Slit collimation of the primary beam was applied in order to increase the flux and to improve the signal quality.

5.4. Catalytic testing

The Rh@MOF catalysts described above were tested in the hydroformylation of olefins with different structures in the similar reaction conditions. Rh@MOF-5, Rh@IRMOF-3, and Rh@MIL-101 were investigated in detail. Therefore, a couple of olefins with different structures as linear *n*-alk-1-enes with varied chain length, branched alk-1-enes, bulky and less reactive cycloolefins, as well as hexa-1,5-diene were involved in the catalytic experiments. The linear *n*-alk-1-enes included *n*-hex-1-ene, *n*-oct-1-ene, *n*-dec-1-ene, and *n*-dodec-1-ene, and even the very long chain molecule as *n*-hexadec-1-ene. The branched olefins and the bulky or less reactive olefins as 3,3-dimethylbut-1-ene (DMB), 4,4-dimethylpent-1-ene (DMP), 2,4,4-trimethylpent-1-ene (TMP), cyclohexene, and cyclooctene were investigated in the

hydroformylation. Also some mixtures of olefins were tested to study the catalytic behavior of each olefin in the reaction of a mixture.

To investigate the influence of the structure and pore sizes of MOFs on the catalytic performance, along with the highly porous catalysts such as Rh@MOF-5, Rh@IRMOF-3, and Rh@MIL-101 stated above, also the mesostructured metal-organic frameworks Rh@MesoMIL-1 and Rh@MesoMIL-2 and the small pore-sized MOF catalysts as Rh@MIL-77 and Rh@MIL-96 have been included in the study.
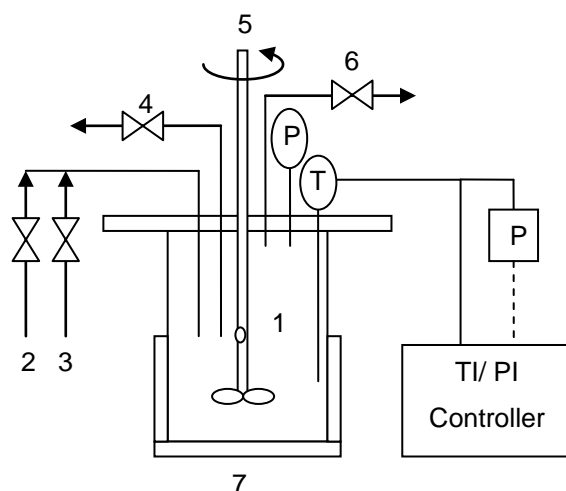
Figure 87. High pressure reaction set up used for hydroformylation of olefins.

(1) PARR high pressure reactor; (2) Argon/Nitrogen; (3) Synthesis gas; (4) Sampling system; (5) Gas introduction stirrer; (6) Venting; (7) Heater plate; (P) Pressure gauge; (TI/ PI Controller) Temperature & Pressure indicators in control panel.

All hydroformylation experiments were carried out in a 100 mL PARR reactor (Figure 87) at $T = 100$ ^{o}C, $p = 50$ bar (CO/H$_2$ = 1), and the substrate to catalyst molar ratio based on rhodium of *ca.* 100000 under stirring at 1000 rpm. The toluene was used as an appropriate solvent.[126]

Typically, in the hydroformylation of *n*-hex-1-ene over Rh@MOF-5, 95 mg of Rh@MOF-5, 12.5 mL of *n*-hex-1-ene, and 30 mL of toluene were loaded into the reactor. The *n*-hex-1-ene to catalyst molar ratio based on rhodium was *ca.* 100000. After loading, the reactor was evacuated and purged with argon. The procedure was repeated in order to remove air and residual moisture. Thereafter, the reactor was immediately loaded with synthesis gas up to a pressure of 50 bar at room temperature. Finally, the reaction mixture was heated under stirring at *ca.* 1000 rpm and

maintained at a temperature of 100 ^{o}C during the course of reaction. The reactor was equipped with a gas introduction stirrer. The reactions of the other olefins over different MOF supported catalysts were carried out in the same way with the similar molar olefin/rhodium ratio.

The reaction products were analyzed by gas chromatography (Agilent HP-6890 equipped with a HP-5 column, 30 m x 0.25 mm x 0.25 μm, and a flame ionization detector, FID). GC/MS analyses were carried out on an Agilent HP-6890 equipped with a capillary column HP-5MS and a mass detector (Agilent MSD 5973). Aliquots of the reaction mixture were taken after 0.5, 1, 2, 3, 4, 5 h and 21 h of reaction and diluted with toluene prior to GC analyses.

6.   References

[1]   F. X. Llabrés i Xamena, J. Gascon, *Metal Organic Frameworks as Heterogeneous Catalysts*, 1 ed., RSC, Cambrigde, UK, **2013**.

[2]   H. Furukawa, N. Ko, Y. B. Go, N. Aratani, S. B. Choi, E. Choi, A. O. Yazaydin, R. Q. Snurr, M. O'Keeffe, J. Kim, O. M. Yaghi, *Science* **2010**, *329*, 424-428.

[3]   T. V. Vu, H. Kosslick, A. Schulz, J. Harloff, E. Paetzold, M. Schneider, J. Radnik, N. Steinfeldt, G. Fulda, U. Kragl, *Appl. Catal., A* **2013**, *468*, 410-417.

[4]   G. Férey, C. Mellot-Draznieks, C. Serre, F. Millange, J. Dutour, S. Surblé, I. Margiolaki, *Science* **2005**, *309*, 2040-2042.

[5]   H. Deng, S. Grunder, K. E. Cordova, C. Valente, H. Furukawa, M. Hmadeh, F. Gándara, A. C. Whalley, Z. Liu, S. Asahina, H. Kazumori, M. O'Keeffe, O. Terasaki, J. F. Stoddart, O. M. Yaghi, *Science* **2012**, *336*, 1018-1023.

[6]   O. M. Yaghi, M. O'Keeffe, N. W. Ockwig, H. K. Chae, M. Eddaoudi, J. Kim, *Nature* **2003**, *423*, 705-714.

[7]   M. Dogru, A. Sonnauer, A. Gavryushin, P. Knochel, T. Bein, *Chem. Commun.* **2011**, *47*, 1707-1709.

[8]   M.-H. Cha, M. C. Nguyen, Y.-L. Lee, J. Im, J. Ihm, *J. Phys. Chem. C* **2010**, *114*, 14276-14280.

[9]   S. M. Cohen, *Chem. Rev.* **2011**, *112*, 970-1000.

[10]   P. Falcaro, A. J. Hill, K. M. Nairn, J. Jasieniak, J. I. Mardel, T. J. Bastow, S. C. Mayo, M. Gimona, D. Gomez, H. J. Whitfield, R. Riccò, A. Patelli, B. Marmiroli, H. Amenitsch, T. Colson, L. Villanova, D. Buso, *Nat. Commun.* **2011**, *2*, 237.

[11]   O. Shekhah, H. K. Arslan, K. Chen, M. Schmittel, R. Maul, W. Wenzel, C. Woll, *Chem. Commun.* **2011**, *47*, 11210-11212.

[12]   R. J. Kuppler, D. J. Timmons, Q.-R. Fang, J.-R. Li, T. A. Makal, M. D. Young, D. Yuan, D. Zhao, W. Zhuang, H.-C. Zhou, *Coord. Chem. Rev.* **2009**, *253*, 3042-3066.

[13]   M. C. Bernini, F. Gándara, M. Iglesias, N. Snejko, E. Gutiérrez-Puebla, E. V. Brusau, G. E. Narda, M. Á. Monge, *Chem. Eur. J.* **2009**, *15*, 4896-4905.

[14]   S. Hermes, M. K. Schroter, R. Schmid, L. Khodeir, M. Muhler, A. Tissler, R. W. Fischer, R. A. Fischer, *Angew. Chem. Int. Edit.* **2005**, *44*, 6237-6241.

[15]   F. T.-S. L. Alaerts, E. Séguinb, J. F. M. Denayer, P. A. Jacobs, D. E. De Vos, in: Z. G. Ruren Xu, Jiesheng Chen, Wenfu Yan (Ed.) *Studies in Surface Science and Catalysis*, Elsevier publications, the Netherlands, **2007**, pp. 1996-2003.

[16]   F. X. Llabrés i Xamena, F. G. Cirujano, A. Corma, *Micropor. Mesopor. Mater.* **2012**, *157*, 112-117.

[17]   M. Ranocchiari, J. A. v. Bokhoven, *Phys. Chem. Chem. Phys.* **2011**, *13*, 6388-6396.

[18]   K. Schlichte, T. Kratzke, S. Kaskel, *Micropor. Mesopor. Mater.* **2004**, *73*, 81-88.

[19]   F. X. Llabrés i Xamena, A. Abad, A. Corma, H. Garcia, *J. Catal.* **2007**, *250*, 294-298.

[20]   H. Zhao, H. Song, L. Chou, *Inorg. Chem. Commun.* **2012**, *15*, 261-265.

[21]   R. Q. Zou, H. Sakurai, S. Han, R. Q. Zhong, Q. Xu, *J. Am. Chem. Soc.* **2007**, *129*, 8402-8403.

[22]   N. B. Pathan, A. M. Rahatgaonkar, M. S. Chorghade, *Catal. Commun.* **2011**, *12*, 1170-1174.

[23]   S. Opelt, S. Türk, E. Dietzsch, A. Henschel, S. Kaskel, E. Klemm, *Catal. Commun.* **2008**, *9*, 1286-1290.

[24]   A. Henschel, K. Gedrich, R. Kraehnert, S. Kaskel, *Chem. Commun.* **2008**, 4192-4194.

[25]   I. Luz, F. X. Llabrés i Xamena, A. Corma, *J. Catal.* **2010**, *276*, 134-140.

[26]   M. Dixit, T. A. Maark, S. Pal, *Int. J. Hydrogen Energ.* **2011**, *36*, 10816-10827.

[27]   M. Eddaoudi, J. Kim, N. Rosi, D. Vodak, J. Wachter, M. O'Keeffe, O. M. Yaghi, *Science* **2002**, *295*, 469-472.

[28]   J. Juan-Juan, J. P. Marco-Lozar, F. Suárez-García, D. Cazorla-Amorós, A. Linares-Solano, *Carbon* **2010**, *48*, 2906-2909.

[29]   J. Li, S. Cheng, Q. Zhao, P. Long, J. Dong, *Int. J. Hydrogen Energ.* **2009**, *34*, 1377-1382.

[30]   J. P. Marco-Lozar, J. Juan-Juan, F. Suárez-García, D. Cazorla-Amorós, A. Linares-Solano, *Int. J. Hydrogen Energ.* **2012**, *37*, 2370-2381.

[31]   D. Saha, S. Deng, *Int. J. Hydrogen Energ.* **2009**, *34*, 2670-2678.

[32] C. Sanchez, K. J. Shea, S. Kitagawa, *Chem. Soc. Rev.* **2011**, *40*, 471-472.

[33] B. Cornils, W. A. Herrmann, M. Rasch, *Angew. Chem. Int. Ed. Engl.* **1994**, *33*, 2144-2163.

[34] S. K. Sharma, P. A. Parikh, R. V. Jasra, *J. Mol. Catal. A: Chem.* **2010**, *316*, 153-162.

[35] C. D. Frohning, C. W. Kohlpaintner, in: B. Cornils, W. A. Herrmann (Eds.) *Applied Homogeneous Catalysis with Organometallic Compounds*, Wiley-VCH Verlag GmbH, Weinheim, **1996**, pp. 29-104.

[36] H.-W. Bohnen, B. Cornils, *Hydroformylation of alkenes: An industrial view of the status and importance*, Advances in Catalysis, Academic Press, **2002**, pp. 1-64.

[37] P. C. J. Kamer, J. N. H. Reek, P. W. N. M. van Leeuwen, in: B. Heaton (Ed.) *Mechanisms in Homogeneous Catalysis, A spectroscopic Approach*, Wiley-VCH, Weinheim, **2005**, pp. 231.

[38] U. Ferenc, *Coord. Chem. Rev.* **2007**, *251*, 2087-2102.

[39] M. Marchetti, S. Paganelli, E. Viel, *J. Mol. Catal. A: Chem.* **2004**, *222*, 143-151.

[40] M. S. Shaharun, B. K. Dutta, H. Mukhtar, S. Maitra, *Chem. Eng. Sci.* **2010**, *65*, 273-281.

[41] D. E. Bryant, M. Kilner, *J. Mol. Catal. A: Chem.* **2003**, *193*, 83-88.

[42] K.-C. Song, J. Y. Baek, J. A. Bae, J.-H. Yim, Y. S. Ko, D. H. Kim, Y.-K. Park, J.-K. Jeon, *Catal. Today* **2011**, *164*, 561-565.

[43] D. Cauzzi, M. Lanfranchi, G. Marzolini, G. Predieri, A. Tiripicchio, M. Costa, R. Zanoni, *J. Organomet. Chem.* **1995**, *488*, 115-125.

[44] J. A. Bae, K.-C. Song, J.-K. Jeon, Y. S. Ko, Y.-K. Park, J.-H. Yim, *Micropor. Mesopor. Mater.* **2009**, *123*, 289-297.

[45] J. Balué, J. C. Bayón, *J. Mol. Catal. A: Chem.* **1999**, *137*, 193-203.

[46] H. Zhu, Y. Ding, H. Yin, L. Yan, J. Xiong, Y. Lu, H. Luo, L. Lin, *Appl. Catal., A* **2003**, *245*, 111-117.

[47] Y. Zhang, H.-B. Zhang, G.-D. Lin, P. Chen, Y.-Z. Yuan, K. R. Tsai, *Appl. Catal., A* **1999**, *187*, 213-224.

[48] T. A. Zeelie, A. Root, A. O. I. Krause, *Appl. Catal., A* **2005**, *285*, 96-109.

[49] T.-J. Yoon, J. I. Kim, J.-K. Lee, *Inorg. Chim. Acta* **2003**, *345*, 228-234.

[50] L. Yan, Y. J. Ding, L. W. Lin, H. J. Zhu, H. M. Yin, X. M. Li, Y. Lu, *J. Mol. Catal. A: Chem.* **2009**, *300*, 116-120.

[51] J. Wrzyszcz, M. Zawadzki, A. M. Trzeciak, J. J. Ziółkowski, *J. Mol. Catal. A: Chem.* **2002**, *189*, 203-210.

[52] A. Riisager, P. Wasserscheid, R. van Hal, R. Fehrmann, *J. Catal.* **2003**, *219*, 452-455.

[53] K. Mukhopadhyay, R. V. Chaudhari, *J. Catal.* **2003**, *213*, 73-77.

[54] V. Isaeva, L. Kustov, *Petrol. Chem.* **2010**, *50*, 167-180.

[55] A. Corma, H. Garcia, F. X. Llabrés i Xamena, *Chem. Rev.* **2010**, *110*, 4606-4655.

[56] M. Fujita, Y. J. Kwon, S. Washizu, K. Ogura, *J. Am. Chem. Soc.* **1994**, *116*, 1151-1152.

[57] D.-Y. Hong, Y. K. Hwang, C. Serre, G. Férey, J.-S. Chang, *Adv. Funct. Mater.* **2009**, *19*, 1537-1552.

[58] P. Horcajada, S. Surble, C. Serre, D. Y. Hong, Y. K. Seo, J. S. Chang, J. M. Greneche, I. Margiolaki, G. Férey, *Chem. Commun.* **2007**, 2820-2822.

[59] D. Addis, S. Zhou, S. Das, K. Junge, H. Kosslick, J. Harloff, H. Lund, A. Schulz, M. Beller, *Chem. Asian J.* **2010**, *5*, 2341-2345.

[60] J. Gascon, U. Aktay, M. D. Hernandez-Alonso, G. P. M. van Klink, F. Kapteijn, *J. Catal.* **2009**, *261*, 75-87.

[61] M. G. Goesten, J. Juan-Alcañiz, E. V. Ramos-Fernandez, K. B. Sai Sankar Gupta, E. Stavitski, H. van Bekkum, J. Gascon, F. Kapteijn, *J. Catal.* **2011**, *281*, 177-187.

[62] H. Li, M. Eddaoudi, M. O'Keeffe, O. M. Yaghi, *Nature* **1999**, *402*, 276-279.

[63] M. Sabo, A. Henschel, H. Frode, E. Klemm, S. Kaskel, *J. Mater. Chem.* **2007**, *17*, 3827-3832.

[64] V. I. Isaeva, O. P. Tkachenko, E. V. Afonina, L. M. Kozlova, G. I. Kapustin, W. Grünert, S. E. Solov'eva, I. S. Antipin, L. M. Kustov, *Micropor. Mesopor. Mater.* **2013**, *166*, 167-175.

[65] Y. Pan, B. Yuan, Y. Li, D. He, *Chem. Commun.* **2010**, *46*, 2280-2282.

[66] J. Hermannsdörfer, R. Kempe, *Chem. Eur. J.* **2011**, *17*, 8071-8077.

[67] X. Zhang, F. X. Llabrés i Xamena, A. Corma, *J. Catal.* **2009**, *265*, 155-160.

[68]   F. Schröder, D. Esken, M. Cokoja, M. W. E. van den Berg, O. I. Lebedev, G. Van Tendeloo, B. Walaszek, G. Buntkowsky, H.-H. Limbach, B. Chaudret, R. A. Fischer, *J. Am. Chem. Soc.* **2008**, *130*, 6119-6130.

[69]   E. V. Ramos-Fernandez, C. Pieters, B. van der Linden, J. Juan-Alcañiz, P. Serra-Crespo, M. W. G. M. Verhoeven, H. Niemantsverdriet, J. Gascon, F. Kapteijn, *J. Catal.* **2012**, *289*, 42-52.

[70]   S. Bhattacharjee, D.-A. Yang, W.-S. Ahn, *Chem. Commun.* **2011**, *47*, 3637-3639.

[71]   S. Subramanian, M. J. Zaworotko, *Angew. Chem. Int. Ed. Engl.* **1995**, *34*, 2127-2129.

[72]   M. Fujita, in: L. R. MacGillivray (Ed.) *Metal-Organic Frameworks, Design and Application*, John Wiley & Sons, New Jersey, USA, **2010**.

[73]   S. Kaskel, *Nachr. Chem.* **2005**, *53*, 394-399.

[74]   S. Kitagawa, R. Kitaura, S.-i. Noro, *Angew. Chem. Int. Ed.* **2004**, *43*, 2334-2375.

[75]   J. R. Long, O. M. Yaghi, *Chem. Soc. Rev.* **2009**, *38*, 1213-1214.

[76]   D. Britt, D. Tranchemontagne, O. M. Yaghi, *Proc. Natl. Acad. Sci.* **2008**, *105*, 11623-11627.

[77]   S. S.-Y. Chui, S. M.-F. Lo, J. P. H. Charmant, A. G. Orpen, I. D. Williams, *Science* **1999**, *283*, 1148-1150.

[78]   L.-G. Qiu, T. Xu, Z.-Q. Li, W. Wang, Y. Wu, X. Jiang, X.-Y. Tian, L.-D. Zhang, *Angew. Chem. Int. Ed.* **2008**, *47*, 9487-9491.

[79]   L. Peng, J. Zhang, J. Li, B. Han, Z. Xue, G. Yang, *Chem. Commun.* **2012**, *48*, 8688-8690.

[80]   W. Xuan, C. Zhu, Y. Liu, Y. Cui, *Chem. Soc. Rev.* **2012**, *41*, 1677-1695.

[81]   X.-D. Do, V.-T. Hoang, S. Kaliaguine, *Micropor. Mesopor. Mater.* **2011**, *141*, 135-139.

[82]   A. R. Millward, O. M. Yaghi, *J. Am. Chem. Soc.* **2005**, *127*, 17998-17999.

[83]   T. Loiseau, C. Serre, C. Huguenard, G. Fink, F. Taulelle, M. Henry, T. Bataille, G. Férey, *Chem. Eur. J.* **2004**, *10*, 1373-1382.

[84]   I. Bezverkhyy, G. Ortiz, G. Chaplais, C. Marichal, G. Weber, J.-P. Bellat, *Micropor. Mesopor. Mater.* **2014**, *183*, 156-161.

[85]   G. Férey, C. Serre, C. Mellot-Draznieks, F. Millange, S. Surblé, J. Dutour, I. Margiolaki, *Angew. Chem. Int. Ed.* **2004**, *43*, 6296-6301.

[86] G. Férey, in: Z. G. R. Xu, J. Chen, and W. Yan (Ed.) *From Zeolites to Porous MOF Materials - the 40th Anniversary of International Zeolite Conference*, Elsevier B.V, the Netherland, **2007**, pp. 66-84.

[87] X. Wu, Z. Bao, B. Yuan, J. Wang, Y. Sun, H. Luo, S. Deng, *Micropor. Mesopor. Mater.* **2013**, *180*, 114-122.

[88] P. Amo-Ochoa, G. Givaja, P. J. S. Miguel, O. Castillo, F. Zamora, *Inorg. Chem. Commun.* **2007**, *10*, 921-924.

[89] Y.-K. Seo, G. Hundal, I. T. Jang, Y. K. Hwang, C.-H. Jun, J.-S. Chang, *Micropor. Mesopor. Mater.* **2009**, *119*, 331-337.

[90] W. Liu, L. Ye, X. Liu, L. Yuan, X. Lu, J. Jiang, *Inorg. Chem. Commun.* **2008**, *11*, 1250-1252.

[91] E. Haque, N. A. Khan, C. M. Kim, S. H. Jhung, *Cryst. Growth Des.* **2011**, *11*, 4413-4421.

[92] E. Haque, S. H. Jhung, *Chem. Eng. J.* **2011**, *173*, 866-872.

[93] S. H. Jhung, J.-H. Lee, P. M. Forster, G. Férey, A. K. Cheetham, J.-S. Chang, *Chem. Eur. J.* **2006**, *12*, 7899-7905.

[94] Z. Lin, D. S. Wragg, R. E. Morris, *Chem. Commun.* **2006**, 2021-2023.

[95] N. Guillou, C. Livage, M. Drillon, G. Férey, *Angew. Chem. Int. Ed.* **2003**, *42*, 5314-5317.

[96] N. Guillou, C. Livage, J. Chaigneau, G. Férey, *Powder Diffr.* **2005**, *20*, 288-293.

[97] T. Loiseau, L. Lecroq, C. Volkringer, J. Marrot, G. Férey, M. Haouas, F. Taulelle, S. Bourrelly, P. L. Llewellyn, M. Latroche, *J. Am. Chem. Soc.* **2006**, *128*, 10223-10230.

[98] J. S. Lee, S. H. Jhung, *Micropor. Mesopor. Mater.* **2010**, *129*, 274-277.

[99] J. G. Nguyen, S. M. Cohen, *J. Am. Chem. Soc.* **2010**, *132*, 4560-4561.

[100] L. Bellarosa, J. M. Castillo, T. Vlugt, S. Calero, N. López, *Chem. Eur. J.* **2012**, *18*, 12260-12266.

[101] S. S. Kaye, A. Dailly, O. M. Yaghi, J. R. Long, *J. Am. Chem. Soc.* **2007**, *129*, 14176-14177.

[102] J. Yang, A. Grzech, F. M. Mulder, T. J. Dingemans, *Chem. Commun.* **2011**, *47*, 5244-5246.

[103] U. Mueller, M. Schubert, F. Teich, H. Puetter, K. Schierle-Arndt, J. Pastre, *J. Mater. Chem.* **2006**, *16*, 626-636.

[104] Sigma-Aldrich, *Mater. Matters* **2008**, *3*, 17-18.

[105] J. Moellmer, A. Moeller, F. Dreisbach, R. Glaeser, R. Staudt, *Micropor. Mesopor. Mater.* **2011**, *138*, 140-148.

[106] R. P. Nielsen, in: J. I. Kroschwitz (Ed.) Kirk-Othmer encyclopedia of chemical technology, John Wiley & Son, **1993**.

[107] J. Hagen, *Industrial Catalysis: A Practical Approach*, 2 ed., Wiley-VCH Verlag GmbH, Weinheim, Germany, **2006**.

[108] Organic Chemistry Resources Worldwide, *Heterogeneous Catalysts*. http://www.organicworldwide.net/content/heterogeneous-catalysts.

[109] I. Ogino, B. C. Gates, *J. Phys. Chem. C*. **2010**, *114*, 2685-2693.

[110] I. Ogino, C. Y. Chen, B. C. Gates, *Dalton T.* **2010**, *39*, 8423-8431.

[111] E. G. Derouane, J.-M. Andre, A. A. Lucas, *J. Catal.* **1988**, *110*, 58-73.

[112] G. Sastre, A. Corma, *J. Mol. Catal. A: Chem.* **2009**, *305*, 3-7.

[113] A. K. Aboul-Gheit, S. M. Abdel-Hamid, E. A. Emam, *Appl. Catal., A* **1999**, *179*, 107-115.

[114] A. K. Aboul-Gheit, A. A. Aboul-Enein, A. E. Awadallah, S. A. Ghoneim, E. A. Emam, *Chinese J. Catal.* **2010**, *31*, 1209-1216.

[115] V. R. R. Pendyala, G. Jacobs, W. D. Shafer, R. A. Keogh, J. Kang, D. E. Sparks, B. H. Davis, *Appl. Catal., A* **2013**, *453*, 195-203.

[116] R. G. Bell, *What are Zeolites?* Bristish Zeolite Association, UK, May 2001. http://www.bza.org/zeolites.html

[117] J. S. Beck, J. C. Vartuli, W. J. Roth, M. E. Leonowicz, C. T. Kresge, K. D. Schmitt, C. T. W. Chu, D. H. Olson, E. W. Sheppard, S. B. Mccullen, J. B. Higgins, J. L. Schlenker, *J. Am. Chem. Soc.* **1992**, *114*, 10834-10843.

[118] D. Y. Zhao, J. L. Feng, Q. S. Huo, N. Melosh, G. H. Fredrickson, B. F. Chmelka, G. D. Stucky, *Science* **1998**, *279*, 548-552.

[119] P. d. Jongh, in: M. Beller, A. Renken, R. A. v. Santen (Eds.) *Catalysis from Principles to Applications*, Wiley-VCH, Weinheim, Germany, **2012**.

[120] S. Bektesevic, A. M. Kleman, A. E. Marteel-Parrish, M. A. Abraham, *J. Supercrit. Fluid.* **2006**, *38*, 232-241.

[121] G. C. Bond, G. Webb, in: G. C. Bond, G. Webb (Eds.) *Catalysis: Volume 6*, the Royal Society of Chemistry, **1983**, pp. 169-195.

[122] A. M. Trzeciak, J. J. Ziolkowski, *Coord. Chem. Rev.* **1999**, *192*, 883-900.

[123] K.-D. Wiese, D. Obst, in: M. Beller (Ed.) *Catalytic Carbonylation Reactions*, Springer Berlin Heidelberg, **2006**, pp. 1-33.

[124] Louisiana State University, *Hydroformylation (Oxo) Catalysis*, United States, 2013. http://chem-faculty.lsu.edu/stanley/webpub/4571-chapt16-hydroformylation.pdf

[125] R. Lazzaroni, R. Settambolo, A. Caiazzo, in: P. N. M. Leeuwen, C. Claver (Eds.) *Rhodium Catalyzed Hydroformylation*, Springer Netherlands, **2002**, pp. 15-33.

[126] A. van Rooy, E. N. Orij, P. C. J. Kamer, P. W. N. M. van Leeuwen, *Organometallics* **1995**, *14*, 34-43.

[127] R. V. Gholap, O. M. Kut, J. R. Bourne, *Ind. Eng. Chem. Res.* **1992**, *31*, 1597-1601.

[128] D. Saha, S. Deng, *J. Colloid Interface Sci.* **2010**, *348*, 615-620.

[129] S. Gao, N. Zhao, M. Shu, S. Che, *Appl. Catal., A* **2010**, *388*, 196-201.

[130] R. S. Mikhail, E. Robens, *Microstructure and thermal analysis of solid surfaces*, John Wiley & Sons Limited, Chichester, **1983**.

[131] G. Tonetto, J. Atias, H. de Lasa, *Appl. Catal., A* **2004**, *270*, 9-25.

[132] D. D. Do, *Adsorption Analysis: Equilibria and Kinetics*, Imperial College Press, London, **1998**.

[133] P. I. Ravikovitch, A. V. Neimark, *Langmuir* **2002**, *18*, 9830-9837.

[134] J. Yang, Q. Zhao, J. Li, J. Dong, *Micropor. Mesopor. Mater.* **2010**, *130*, 174-179.

[135] T. V. Vu, H. Kosslick, A. Schulz, J. Harloff, E. Paetzold, H. Lund, U. Kragl, M. Schneider, G. Fulda, *Micropor. Mesopor. Mater.* **2012**, *154*, 100-106.

[136] O. Glatter, O. Kratky, *Small angle x-ray scattering*, Academic Press Inc. Ltd., Lodon, **1982**.

[137] A. C. Geiculescu, H. J. Rack, *J Non-Cryst. Solids* **2002**, *306*, 30-41.

[138] J. Schaffer, V. A. Kondratenko, N. Steinfeldt, M. Sebek, E. V. Kondratenko, *J. Catal.* **2013**, *301*, 210-216.

[139] M. J. Ingleson, J. Perez Barrio, J.-B. Guilbaud, Y. Z. Khimyak, M. J. Rosseinsky, *Chem. Commun.* **2008**, 2680-2682.

[140] H. Kosslick, R. Bräunig, R. Eckelt, J. Harloff, S. Mothes, H. Häring, S. Wilhelm, A. Schulz, *J. Chem. Chem. Eng.*, **2011**, *5* 170-176.

[141] W. J. Mortier, *Compilation of Extra-Framework Cation Sites in Zeolites*, Butterworth Scientific Ltd., Great Britain, **1982**.

[142] T. V. Vu, H. Kosslick, A. Schulz, J. Harloff, E. Paetzold, J. Radnik, U. Kragl, G. Fulda, C. Janiak, N. D. Tuyen, *Micropor. Mesopor. Mater.* **2013**, *177*, 135-142.

[143] J. Patel, S. Mujcinovic, W. R. Jackson, A. J. Robinson, A. K. Serelis, C. Such, *Green Chem.* **2006**, *8*, 450-454.

[144] H. Yim, E. Kang, J. Kim, *B. Korean Chem. Soc.* **2010**, *31*, 1041-1042.

[145] Z. Wang, S. M. Cohen, *Angew. Chem.* **2008**, *120*, 4777-4780.

[146] W. Morris, R. E. Taylor, C. Dybowski, O. M. Yaghi, M. A. Garcia-Garibay, *J. Mol. Struct.* **2011**, *1004*, 94-101.

[147] S. L. Gould, D. Tranchemontagne, O. M. Yaghi, M. A. Garcia-Garibay, *J. Am. Chem. Soc.* **2008**, *130*, 3246-3247.

[148] F. Stallmach, S. Gröger, V. Künzel, J. Kärger, O. M. Yaghi, M. Hesse, U. Müller, *Angew. Chem. Int. Ed.* **2006**, *45*, 2123-2126.

[149] P. Bräuer, S. Fritzsche, J. Kärger, G. Schütz, S. Vasenkov, in: R. Haberlandt, D. Michel, A. Pöppl, R. Stannarius (Eds.) *Molecules in Interaction with Surfaces and Interfaces*, Springer Berlin Heidelberg, **2004**, pp. 89-125.

[150] S. Hermes, F. Schroder, S. Amirjalayer, R. Schmid, R. A. Fischer, *J. Mater. Chem.* **2006**, *16*, 2464-2472.

[151] L. M. Huang, H. T. Wang, J. X. Chen, Z. B. Wang, J. Y. Sun, D. Y. Zhao, Y. S. Yan, *Micropor. Mesopor. Mater.* **2003**, *58*, 105-114.

7. Appendices

7.1. List of chemicals used

Substance	Origin	Substance	Origin
2,4,4-Trimethylpent-1-ene	Sigma-Aldrich, 99%	Hexa-1,5-diene	Jenssen, 98%
2-Aminoterephthalic acid	Sigma-Aldrich, 99%	n-Dec-1-ene	Acros, 95%
3,3-Dimethylbut-1-ene	Sigma-Aldrich, 95%	n-Dodec-1-ene	Acros, 93-95%
4,4-Dimethylpent-1-ene	SAFC, 99%	n-Hex-1-ene	Sigma-Aldrich, 97%
Acetonitrile	Baker, 99.8%	n-Hexadec-1-ene	Acros, 98%
$Cr(NO_3)_3 \cdot 9H_2O$	Merck, 99%	n-Oct-1-ene	Sigma-Aldrich, 98%
CTAB	Sigma-Aldrich, 95%	Rh(acac)(cod)	Sigma-Aldrich, 99%
Cyclohexene	Sigma-Aldrich, 99%	Terephthalic acid	Merck, 98%
Cyclooctene	Acros, 95%	$C_4H_{13}NO \cdot 5H_2O$	Sigma-Aldrich, 97%
DEF	Sigma-Aldrich, 99%	Toluene	Merck, 99.5%
Dichloromethane	Sigma-Aldrich, 99%	$Zn(NO_3)_2 \cdot 4H_2O$	Merck, 98.5%
DMF	Merck, 99.8%		

7.2. List of publications

1. T.V. Vu, H. Kosslick, A. Schulz, J. Harloff, E. Paetzold, M. Schneider, J. Radnik, N. Steinfeldt, G. Fulda, U. Kragl, *Selective hydroformylation of olefins over the rhodium supported large porous metal–organic framework MIL-101,* Applied Catalysis A: General 468 (2013)410-417.

2. T.V. Vu, H. Kosslick, A. Schulz, J. Harloff, E. Paetzold, J. Radnik, U. Kragl, G. Fulda, C. Janiak, N.D. Tuyen, *Hydroformylation of olefins over rhodium supported metal-organic framework catalysts of different structure,* Microporous and Mesoporous Materials 177 (2013)135-142.

3. T. V.Vu, H. Kosslick, A. Schulz, J. Harloff, E. Paetzold, H. Lund, U. Kragl, M. Schneider, G. Fulda, *Influence of the textural properties of Rh/MOF-5 on the catalytic properties in the hydroformylation of olefins,* Microporous and Mesoporous Materials154 (2012) 100-106.

7.3. List of oral and poster presentations

1. T.V. Vu, H. Kosslick, and A. Schulz, *Influence of the structure of metal-organic frameworks on the catalytic hydroformylation of olefins over Rh@MOFs,* Poster presentation at the 26[th]GermanZeoliteConference (Die 26 DeutschenZeolith-Tagung), Paderborn, Germany, 26–28/2/2014.

2. H. Kosslick, T.V. Vu, and A. Schulz, *Different nano-sized metal-organic framework supported catalysts in hydroformylation of olefins,* Oral presentation at the 2nd Saudi International Nanotechnology Conference, Riyadh, Saudi Arabia, 11–13/11/2012.

3. H. Kosslick, T.V. Vu, and A. Schulz, *Hydroformylation of olefins over metal-organic framework supported Rh catalysts of different structure*, Poster presentation at the ZMPC 2012: International Symposium on Zeolites and Microporous Crystals, Hiroshima, Japan, 28/7/2012–01/8/2012.

4. H. Kosslick, V.T. Vu, J. Harloff, H. Lund, A. Schulz, E. Paetzold, U. Kragl, and M. Beller, *Effect of textural properties of Rh@MOF-5 on the catalytic properties in the hydroformylation*, Poster presentation at the 9th International Symposium on the Characterization of Porous Solids – COPS 9, Dresden, Germany, 05–08/6/2011.